Multi-Scale Numerical Modelling of Phase Transition Phenomena in Metallic Alloys

Ali Chirazi

A thesis submitted in partial fulfilment of the requirements of the University of Greenwich for the Degree of Doctor of Philosophy

November 2000

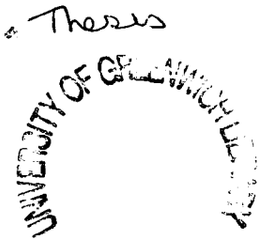

List of Figures

Contents

Acknowledgement

I would like to thank my supervisor at the University of Greenwich, Dr. H. Rafii-Tabar, for his valuable guidance, advice and assistance and also Dr. C. Bailey for useful discussions and interest shown in my work.

My thanks also extended to Dr. P. D. Lee, Mr. R. C. Atwood and others in the Materials Department at the Imperial College of Science, Technology and Medicine, who contributed to this work in one way or another. I am also extremely grateful to my parents and my wife for their patience and encouragement.

Finally, i would like to thank the University of Greenwich for partially supporting this work.

Abstract

A multiscale numerical model of the solidification process involving the metallic alloys is proposed. The purpose of this model is to increase our basic knowledge of the physics of the solidification by incorporating atomic aspects of the phase change and, therefore, to predict the microstructural features of the phase transformation based on the alloy parameters, such as the solute concentration and the process parameters, such as the cooling rate and surface roughness. The proposed multiscale strategy, is based on the parametric study of the solidification process at atomistic (nano), microscopic (meso) and macroscopic levels. Once the major parameters, influencing the process at each scale, are identified, the three different levels are linked via the creation of relevant databases and the passage of information from one scale to another is implemented by using these databases.

The multiscale model utilises the Molecular Dynamics (MD) methods at the atomic level, the Cellular Automaton (CA) method at the microscale and the Finite Volume (FV) models at the macroscale. The combination of these methods allowed us to study the phase transition beginning from the atomic clusterisation, progressing to the microstructure formation and culminating in the bulk formation at the macro level.

General Introduction

Solidification is a multiscale and multiphysics process involving various time, length and energy scales. The quality of cast and as-cast alloys used in everyday industrial applications, such as automotive and airspace industries, depends on the quality of casting process. The solidification process influences the thermo-mechanical properties of the alloys such as fatigue strength, total elongation and hardness [1, 2, 3, 4]. The complexity of the process makes a full and detailed study a difficult task, involving a full parametric study of the phenomenon at different time and length scales.

The subject of this Thesis is to propose a multiscale model of solidification, linking the atomistic, the microscopic and the macrocopic approaches to the solidification. This multiscale methodology is validated by applying it to several elemental and alloy systems. Aluminum and tin based alloys were chosen due to their wide scale application in automotive airspace and electronic packaging industries respectively.

This Thesis is comprised of three Chapters. The first Chapter introduces the atomistic approach to the phase transition. It introduces the fundamental and pertinent principles of the statistical mechanics and the notion of interatomic potentials as well as the corresponding computational methods used in atomistic modelling. The aim of the first Chapter is to prove the capability of atomistic models to deal in an accurate, reliable and comprehensive way, with the solid-to-liquid and liquid-to-solid phase transitions and therefore, their capacity to be used as a serious alternative, or complement, to the time consuming and expensive experimental measurements of material properties needed in the micro-scale and macro-scale simulations. On the other hand, the use of properties based on atomistic models provides the micro and macro scale simulations with a firm physical basis and decreases considerably the need for empirical assumptions in these simulations. The second Chapter describes the microscale approach to the solidification and its ability to reproduce microstructural features and their influence on the mechanical properties of the final cast. It also discuss the mechanism by which atomistic models can contribute to the improvement of the micro models and describes in details the links between the atomistic and micro scales. The aim of the second

Chapter is to implement the combined atomistic-micro model, using the Rappaz model for the micro modelling as described in Chapter 2, and to validate this bi-scale model by comparing qualitatively and quantitatively (where possible) the results obtained via the bi-scale model with other experimental and computational results. The model was validated for different alloying systems undergoing different solidification processes.

The last Chapter deals with the macroscopic approach to the phase transition. It discusses the macro model used for the simulation of the heat and mass transfer during the solidification and the way by which the link between the atomistic-micro model, already developed, and the macro model can improve the predictions of the model and also enable the model to predict the local microstructure of solidification at a given temperature. It discusses in details the links between the atomistic and macroscopic, the microscopic and macroscopic models and how their present limitations could be overcome by using outputs from the atomistic and microscopic models. The aim of the third Chapter is to implement the coupled atomistic-micro- macro model of solidification, using the Physica software for the macro modelling as described in Chapter 3, and to validate this multiscale model by applying it to several commonly used and industrially important binary alloys, and to compare qualitatively and quantitatively (where possible) its results with other experimental or computational results.

The full implementation of the model, with all the links between different scales is presented schematically in the Figure 1. The way by which different discretised domains at various levels are linked together is shown in Figure 2. As shown in Figure 1, material properties calculated at atomistic level, such as the nucleation rate, diffusion coefficient, specific heat , latent heat and shear viscosity, are used as input to both the micro and macro levels. The micro level results, such as the variation of the solid fraction for a given cooling rate and mould's quality, are used also as input to the macro level and the output of macro level, such as the temperature field, is feed back to the micro level for the prediction of local microstructures. The influence of process parameters, such as the cooling rate, were taken into account at the atomistic level as well as the alloy parameters, such as the solute concentration.

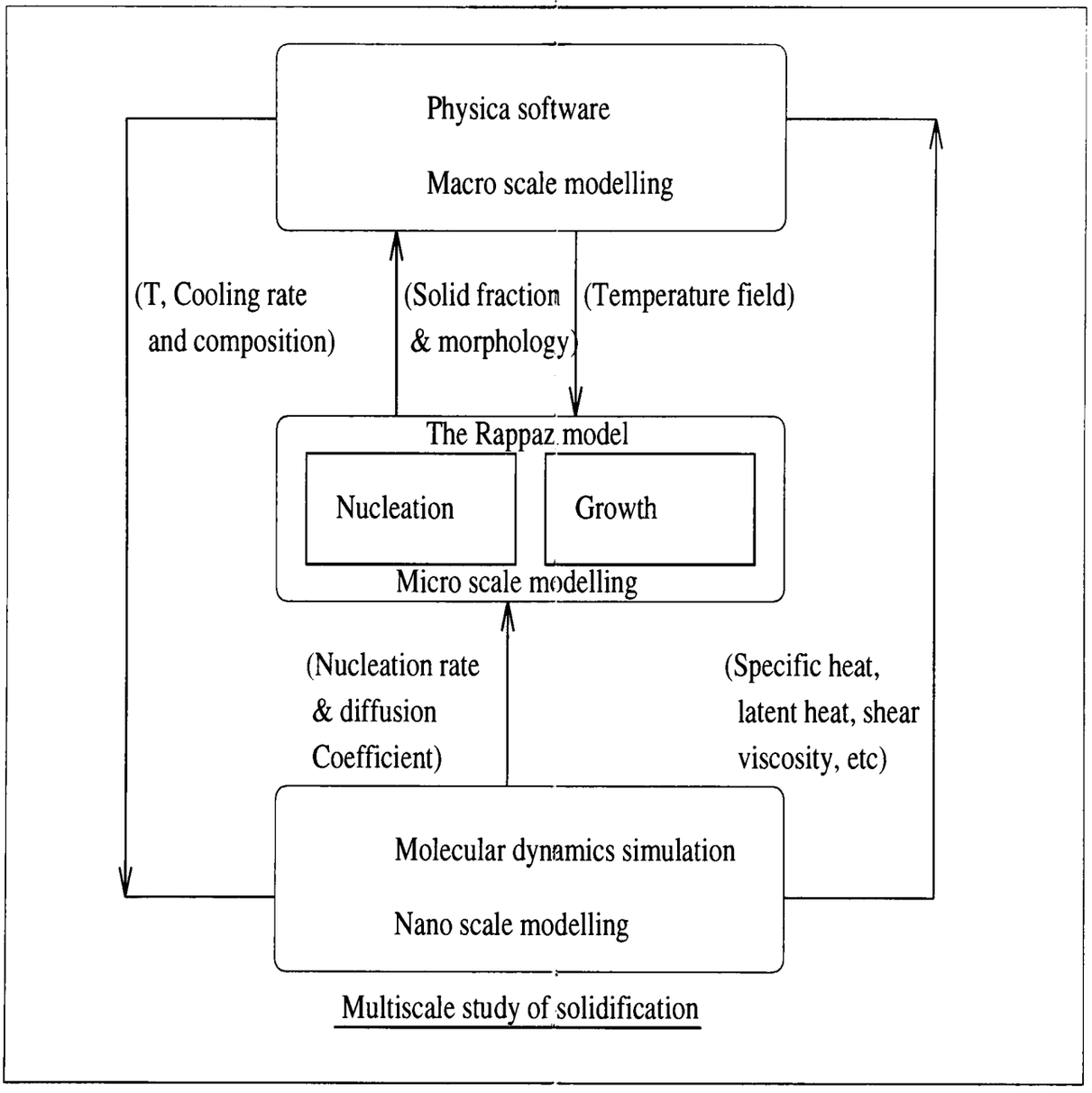

Figure 1: Flow-chart linking nano-micro-macro scales using a parametric study

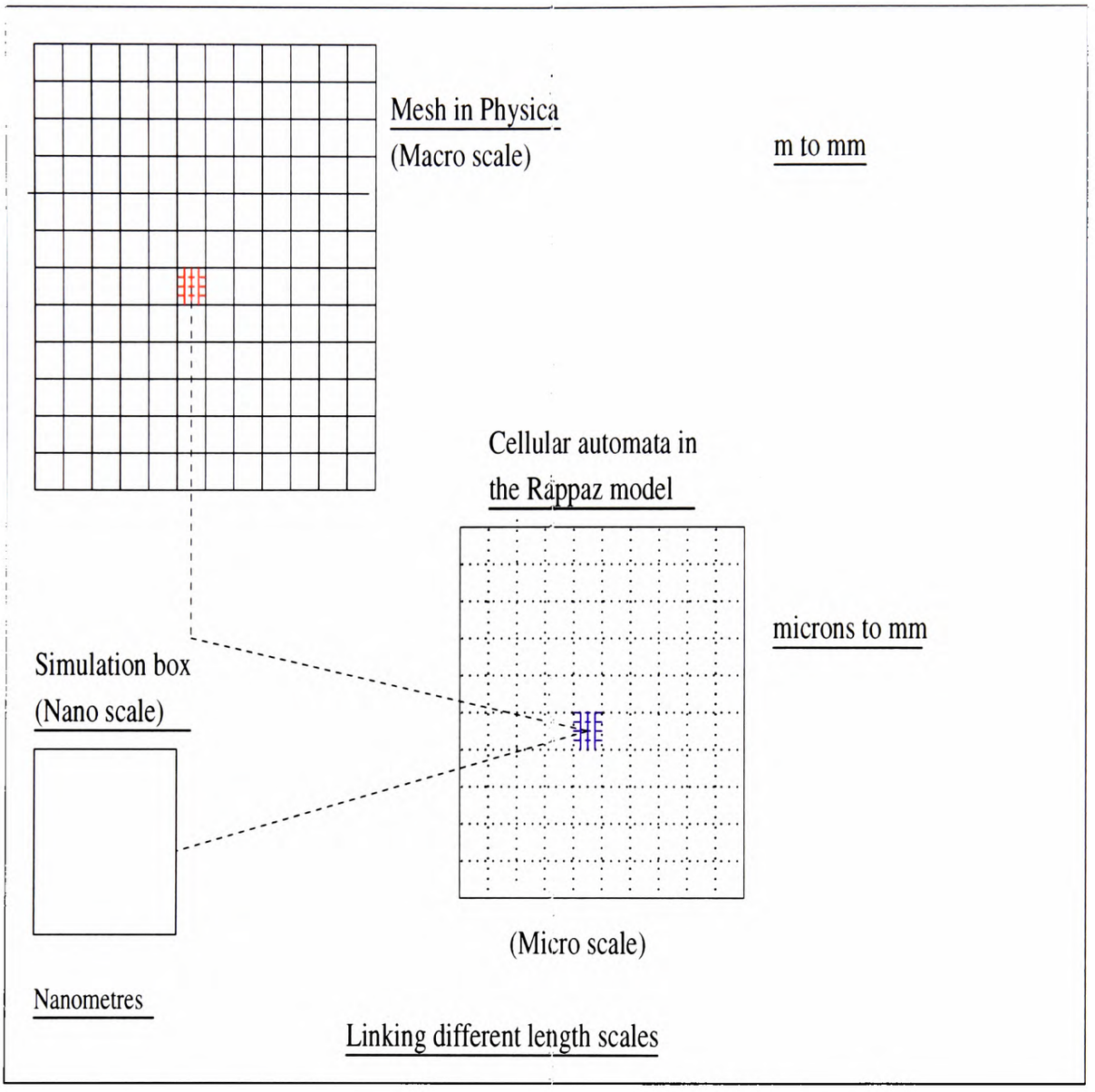

Figure 2: Zooming on the scales from the macro scale mesh to the MD simulation cell

Chapter 1

Nano-Scale approach to phase transition

1.1 Why do we need an atomistic modelling?

Phase transitions, like many other natural phenomena, originate at an atomistic level. The need to describe and to understand fully the nature of the physical processes involved in order to control, and therefore adapt, them to industrial applications is an ongoing challenge. Phase transitions are *multiscale* and *multiphysics* processes, involving different time, length and energy scales. To study these processes we need to know why, when and how they are initiated. Since a phase transition begins with atoms and molecules rearranging themselves within the system, we need to include an *atomistic* aspect to the modelling of the overall process. The knowledge of the atomistic structure and the manner in which it changes due to a phase transition will allow us to shed light on underlying parameters which influence and control the physics of the system. Without an atomistic approach to a phase transition, the real nature of the processes involved could not be completely understood.

In this Chapter, the nature of phase transitions in metallic systems and the method of the Molecular Dynamics (MD) simulation, based on the use of prescribed interatomic potentials, to model the initial stages in the emergence of these transitions will be discussed. We concentrate

on the liquid-to-solid transitions in elemental and binary alloys since these transitions influence the final microstructures in casts and also determine their thermo-mechanical properties. Solidification, unlike melting, occurs once a potential barrier has been overcome [5]. A liquid system shedding its heat content will reduce the speed of its atoms, or molecules. At a sufficiently low temperature, atomic clusters in the liquid, which have been unstable until now and could disassemble quite easily due to thermal agitation, are transformed into solid nuclei [5, 6, 7] in which the interatomic attractions are greater than the thermal agitations. This critical undercooling of the liquid system, which is necessary for the creation of solid nuclei, corresponds to a critical Gibbs free energy [5, 6, 7], which is a manifestation of the potential barrier to solidification. With each nucleus size there is associated a critical undercooling and a critical radius [5]. The higher is the undercooling, the smaller will be, the critical radius. This is due to the fact that the number of atoms necessary to interact, in order to overcome the thermal agitation, decreases with an increasing undercooling [5, 8]. For elemental metals, the critical undercooling can even reach 20% of the value of the melting point [8]. For alloys, as we shall see in this Chapter, the critical undercooling is much less (around 5%) [8].

The task of pin-pointing the transition from the liquid state to the solid state is quite important and is based on the calculation of the level of order, within the system [9]. Further on in this Chapter, the main methods used to calculate the orderlyness of an atomic system will be discussed.

1.2 Study of Phase Formation

1.2.1 Various orders of phase transition

Generally speaking, there are two kinds of phase transformations [10]. These are referred to as the *first* order and the *second* order transitions. If we consider a given property, A, whose phase transition is under investigation, and which is a function of x_i state variables $(i = 1, \cdots, N)$, we can define an n^{th} order phase transition if and only if $\left(\frac{\partial^n A_1}{\partial x_i^n}\right) \neq \left(\frac{\partial^n A_2}{\partial x_i^n}\right)$ and all other lower order derivatives are continuous throughout the transition zone, where A_1 is

associated with the phase one and A_2 with the phase two [10].

In the case of thermodynamic phase transitions, the system's property that is of interest is the Gibbs free energy, and the state variables considered are the temperature and pressure [10, 11]. Consequently, a first order phase transition is obtained when [10]

$$\begin{aligned} \left(\frac{\partial G_1}{\partial T}\right)_P &\neq \left(\frac{\partial G_2}{\partial T}\right)_P , \\ \left(\frac{\partial G_1}{\partial P}\right)_T &\neq \left(\frac{\partial G_2}{\partial P}\right)_T . \end{aligned} \tag{1.1}$$

An example of a first order phase transition is the solid-to-liquid transition [10, 11].

A second order phase transition is obtained when

$$\begin{aligned} \left(\frac{\partial^2 G_1}{\partial T^2}\right)_P &\neq \left(\frac{\partial^2 G_2}{\partial T^2}\right)_P , \\ \left(\frac{\partial^2 G_1}{\partial P^2}\right)_T &\neq \left(\frac{\partial^2 G_2}{\partial P^2}\right)_T , \end{aligned} \tag{1.2}$$

where the first order derivatives are continuous throughout the transition zone.

1.2.2 Why does a phase transition occur?

All systems have the tendency to go towards a state of maximum entropy and minimum enthalpy and therefore their equilibrium state at a given temperature and pressure must satisfy these criteria [8, 12]. As mentioned previously, the fundamental quantity to consider is the Gibbs free energy which is defined as

$$G = H - TS = H + \mu , \tag{1.3}$$

where H is the enthalpy, given by

$$H = E + PV , \tag{1.4}$$

and S is the entropy, μ the chemical potential, E is the total internal energy, P is the pressure and V is the volume of the system. At equilibrium, $dG = 0$. Therefore, for two given phases we must have $G_2 - G_1 = \Delta G < 0$ to obtain a phase transition from 1 to 2. At the transition temperature (T_m), the two phases have the same G values and coexist together. For

temperatures above (T_m) the liquid phase has a lower Gibbs free energy and is therefore the more stable phase.

1.2.3 Liquid-to-solid phase transition

In contrast to a melting process which occurs when the system reaches its transition temperature (T_m) [5], the solidification does not occur until a certain critical temperature, (T_c), *below* the (T_m), is reached. [5, 8, 12]. The difference, $\Delta T = T_m - T_c$, is called the *undercooling*, or the *supercooling*, of the system. The origin of this phenomenon can be seen from Figure 1.1 below [8], where the potential barrier has to be overcome before the system can change its

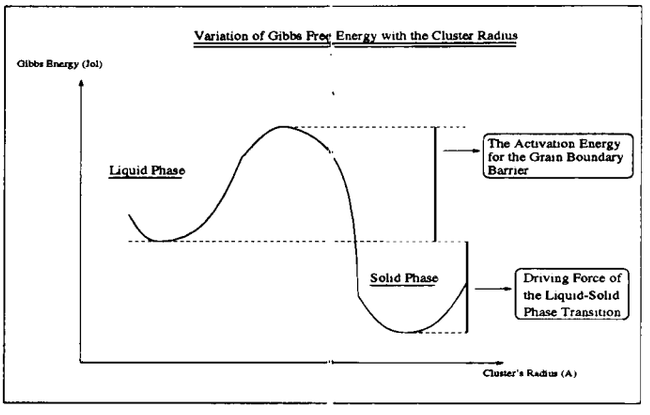

Figure 1.1: Potential barrier to solidification

phase.

According to the Volmer's theory [5], a phase transition begins with local deviations from the normal state leading to fluctuations in density and concentration. In a *homogeneous* system, such as a liquid or a vapour, there are always small fluctuations of the density compatible with the global state of aggregation. These are called *homophase* fluctuations. On the other hand, there might be the *hetrophase* fluctuations which lead to the emergence of a *new* state of aggregation. These density fluctuations are stochastic in nature. If these density fluctuations are sufficiently intense, they lead to an increase in the number of possible collisions among the atoms, resulting in the emergence of clusters of atoms in the system. These clusters are of

random shapes but they can be approximated by *spherical* shapes and therefore a radius can be associated with them. If the mother phase, for example the liquid phase, is more stable, i.e. its chemical potential is smaller than that of the new phase, then the clusters will not grow and will decay back into the mother phase. On the other hand, if the chemical potential of the new phase is smaller than that of the mother phase, then the clusters will grow without limit after reaching a certain *critical* radius. Such clusters are referred to as *critical nuclei.* The variation in Gibbs free energy resulting in the generation of critical nuclei is given by [5]

$$\Delta G_c = \frac{4\eta_s^3\gamma^3}{27\Delta\mu^2}, \tag{1.5}$$

and

$$n_c = \left(\frac{2\eta_s\gamma}{3\Delta\mu}\right)^3, \tag{1.6}$$

is the number of atoms in the critical nucleus, and where η_s is the cluster's shape factor, γ is the surface tension and μ is the chemical potential.

1.3 Elements of Statistical Mechanics

1.3.1 Pertinet concepts from statistical mechanics

Statistical mechanics acts as the link coupling the microscopic, i.e. the atomistic, description of a system to its gross, thermodynamic, or macroscopic state. We now introduce some of its essential concepts that underlie the MD modelling studies reported in this Thesis.

A mole of any material consists of 6.02×10^{23} atoms. The *macrostate* of such an assembly of particles, characterized by a set of macrostate variables, such the energy E, the volume V, and the temperature T, at any time t can be realised in one of an extremely large number of *microstates*, characterized by the positions and momenta of the constituent particles. For an N-particle system, it is more convenient to represent the microstate of the system as a point in an abstract $6N$-dimensional space, called the *phase space.* As time evolves the system switches from one microstate to another, resulting in the motion of the representative point

in the phase space to trace a trajectory. Since over a reasonable time duration all we observe is the time-averaged behaviour of the system, it is more practical to consider a collection of systems, all mental copies of the original system but in different microstates, all of which are compatible with the same macrostate, at a *single* instant of time, and then compute the average behaviour over this collection, rather than of the original system over the time duration. Such a collection is called a Gibbs *ensemble*, and the average computed over the ensemble is referred to as the *ensemble average*.

Since over a sufficiently long period of time, a system will be able to visit all the different accessible microstates in the phase space, therefore any trajectory defined over the phase space will be reversible. This is called the *ergodicity* principal [13, 14] and any ensemble satisfying it will be considered as an ergodic ensemble. *A statistical ensemble at equilibrium is an ergodic ensemble in which the time average and the ensemble average of any property calculated over a long period of time are equal* [13, 14]. The assumption of this equality between these two averages lies at the very foundations of the MD simulation technique.

1.3.2 Statistical-mechanical ensembles

Depending on the prescribed set of macroscopic conditions, one can define four major ensembles enumerated below (see Figures 1.2) [11, 15]:

- An isolated system in equilibrium is represented by a *microcanonical ensemble* in which the set (N,V,E) is kept constant, where N is the number of particles, V is the volume and E is the total energy.

- A closed system in thermal equilibrium with a heat bath is represented by a *canonical ensemble* in which the set (N,V,T) is kept constant, where T is the temperature.

- An open system in thermal equilibrium with a particle chamber is represented by *grand-canonical ensemble* in which the set (μ, V, T) is kept constant, where μ is the chemical potential (see Section 1.3).

- A closed system in thermal equilibrium with a pressure bath is represented by an *isobaric-isothermal ensemble* in which the set (N, P, T) is kept constant, where P is the pressure.

We can define the probability distribution function of an ensemble as a *weight function*, $W_{ens}(\Gamma)$ [13, 14]

$$\begin{aligned} \rho_{ens}(\Gamma) &= Q_{ens}^{-1} W_{ens}(\Gamma)\,, \\ Q_{ens} &= \textstyle\sum_{\Gamma} W_{ens}(\Gamma)\,, \end{aligned} \tag{1.7}$$

where Q_{ens} is called the *partition* function of the ensemble.
The ensemble-average value of any property is given by

$$< A >_{ens} = \frac{\sum_{\Gamma} W_{ens}(\Gamma) A(\Gamma)}{Q_{ens}}\,, \tag{1.8}$$

where A is the property under study and Γ denotes a particular point in 6N-dimensional phase space.

1.4 Molecular Dynamics (MD) Simulation Method

1.4.1 Equations of motion

Classical molecular dynamics simulation is concerned with the computation of space-time trajectories of a system of N interacting particles confined to a finite volume [13, 16]. The coupled differential equations of motion of the particles are solved using a variety of finite difference methods. The forces experienced by the particles appear in the equations of motion, and these are computed as the negative gradient of scalar potentials. The prescribed potential functions are represented by interatomic potentials which can be obtained either from *first principal* calculations that take into account the electronic degrees of freedom, or by semi-empirical methods that employ a variety of *fitting procedures.*
In a classical MD simulation the deterministic force experienced by the particle i in an N-particle assembly is given by

$$m_i \ddot{\mathbf{r}}_i = \mathbf{f_i} \tag{1.9}$$

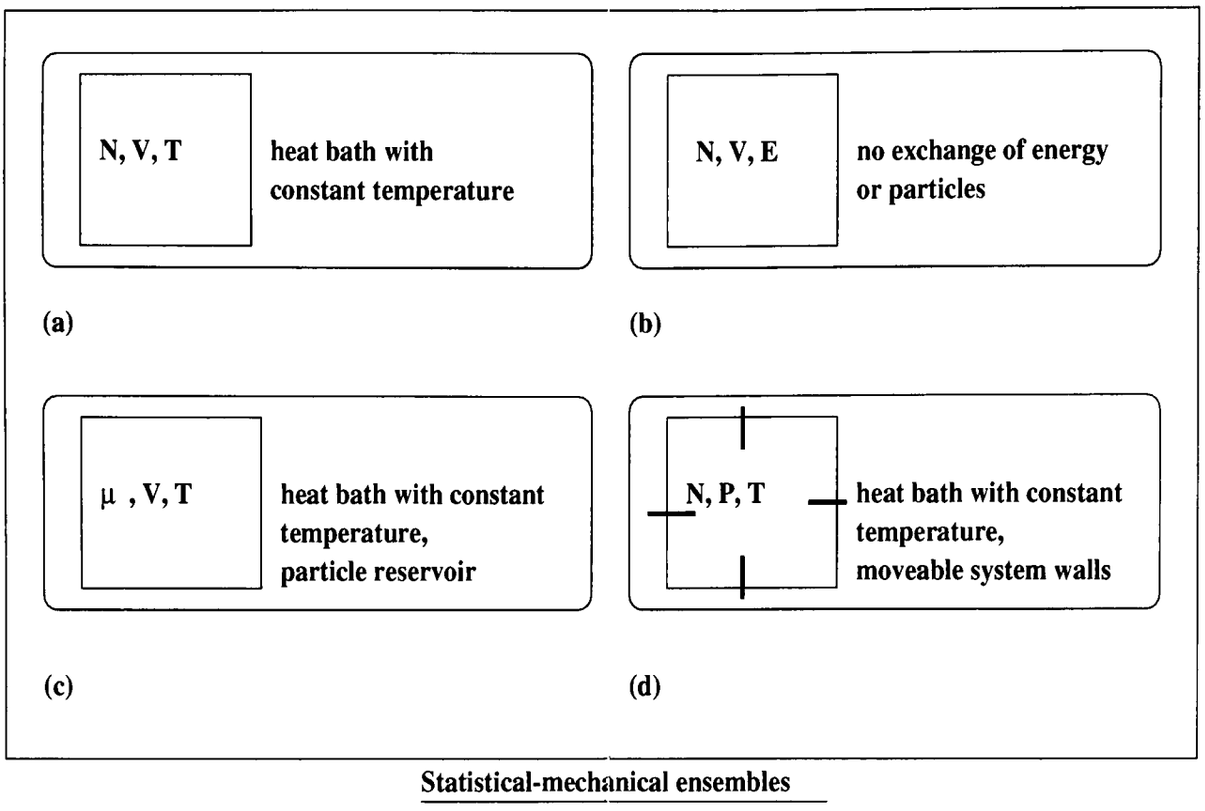

Figure 1.2: Typical ensembles used in MD simulations: (a) canonical ensemble with Helmholz Free energy as the thermodynamic potential; (b) microcanonical ensemble with the entropy as the thermodynamic potential; (c) grandcanonical enesemble with Massiue function as the thermodynamic potential; (d) isobaric-isothermal ensemble with Gibbs Free energy as the thermodynamic potential.

where m_i is the mass of the particle. In terms of the total interaction potential energy, U, the force can be written as

$$\mathbf{f_i} = -\nabla_{\mathbf{r_i}} U \tag{1.10}$$

In an MD simulation, we can make the assumption that the total potential energy can be expanded in terms of two-body, three-body, etc terms

$$U = \sum_i V_1(\mathbf{r_i}) + \sum_i \sum_{j>i} V_2(\mathbf{r_i}, \mathbf{r_j}) + \sum_i \sum_{j>i} \sum_{k>j>i} V_3(\mathbf{r_i}, \mathbf{r_j}, \mathbf{r_k}) + \cdots \tag{1.11}$$

where the first term represents the potential due to *external* sources to the system, and the remaining terms are due to the *internal* interactions among the particles. The total kinetic energy is given by [13]

$$E_k = \sum_{i=1}^{N} \frac{p_i^2}{2m_i}. \tag{1.12}$$

1.4.2 Finite-difference methods of solution of equations of motion

In an MD simulation, we have to solve a system of N coupled equations of motion ,eqn. (1.9). A variety of finite-difference methods have been devised for this purpose [13]. Below, we briefly summarize those techniques that have been employed in this Thesis.

1.4.2.1 The Verlet algorithm

The Verlet algorithm, is a step-by-step finite difference method and is based on the Taylor expansion of the dependent variable under investigation at time t [13]. To calculate the equations of motion, eqn. (1.9), the algorithm stores the positions, $\mathbf{r}(t)$ and $\mathbf{r}(t-\delta t)$ at times t and $(t-\delta t)$ and the acceleration, $\mathbf{a}(t)$, at time t. If we consider two Taylor expansions

$$\begin{aligned} \mathbf{r}(t+\delta t) &= \mathbf{r}(t) + \delta t \mathbf{v}(t) + \tfrac{1}{2}\delta t^2 \mathbf{a}(t)\,, \\ \mathbf{r}(t-\delta t) &= \mathbf{r}(t) - \delta t \mathbf{v}(t) + \tfrac{1}{2}\delta t^2 \mathbf{a}(t)\,, \end{aligned} \tag{1.13}$$

then by adding these two series together we obtain the Verlet algorithm for positions as

$$\mathbf{r}(t+\delta t) = 2\mathbf{r}(t) - \mathbf{r}(t-\delta t) + \delta t^2 \mathbf{a}(t). \tag{1.14}$$

where δt is the time step. As can be seen, the velocities have been eliminated and are therefore not necessary for the calculation of the trajectories, but they are needed for the calculation of the kinetic energy and therefore the total energy. Hence, subtracting the two series gives

$$\mathbf{v}(t) = \frac{\mathbf{r}(t+\delta t) - \mathbf{r}(t-\delta t)}{2\delta t}\,. \tag{1.15}$$

It can be seen from these equations that the Verlet algorithm, due to the symmetrical aspect of $\mathbf{r}(t-\delta t)$ and $\mathbf{r}(t+\delta t)$, is time reversible and the evolution of the trajectories is handled in one step in contrast to some other methods.

1.4.2.2 Velocity-Verlet algorithm

The original Verlet method has been extended where the positions, velocities and accelerations are all stored at the *same* time step [13]. The advantage of the method is that it minimizes the round-off error. This is a two-step method in which the first step consists of

$$\begin{aligned} \mathbf{r}(t+\delta t) &= \mathbf{r}(t) + \delta t \mathbf{v}(t) + \tfrac{1}{2}\delta t^2 \mathbf{a}(t)\,, \\ \mathbf{v}(t+\tfrac{1}{2}\delta t) &= \mathbf{v}(t) + \tfrac{1}{2}\delta t \mathbf{a}(t)\,, \end{aligned} \tag{1.16}$$

where the positions are advanced from t to $t+\delta t$ but velocities from t to $t+\frac{1}{2}\delta t$. To obtain the velocities at t, forces are computed at $t+\delta t$, and using these, we have

$$\mathbf{v}(t+\delta t) = \mathbf{v}(t+\frac{1}{2}\delta t) + \frac{1}{2}\delta t \mathbf{a}(t+\delta t)\,. \tag{1.17}$$

1.4.3 Periodic Boundary Conditions (PBC)

In an MD simulation, we consider a finite nano-sized model system to represent an element of the macroscopic system. The finite size of the system introduces undesirable *surface effects* since the percentage of atoms on the surface of the model is relatively high. Therefore, the bulk properties cannot be properly represented [13].

To overcome this problem, use is made of *periodic boundary conditions* as shown in Figure 1.3 [13]. In this method the central simulation box is replicated in three dimensions throughout the space, and this mimics an infinite lattice representing the bulk phase[13]. When a particle within the central box moves, all its periodic images within the periodic boxes move in exactly the same way. Therefore, if a particle leaves the central box from the right hand side, one of its periodic images enters the box from the left hand side. This procedure eliminates the

surface effects associated with small systems. There are some limitations concerning the use of the boundary conditions to represent the bulk phase at equilibrium. Due to the symmetry of the simulation box, some anisotropy can be artificially imposed on the system which may be isotropic at the beginning. On the other hand, if we have long range interatomic forces, any particle can interact with its own images within the adjacent boxes and will introduce errors into the calculation of the force and potential. Another problem is the suppression of all the density wavelengths bigger than the length of box. These phenomena occur mostly near the phase transition zones. Therefore, we can conclude that the best use of the PBC is when the system is at equilibrium, far from the phase transition regime and having a short range interatomic potential.

It is possible to use noncubic or spherical boxes to reduce the anisotropy effect but in

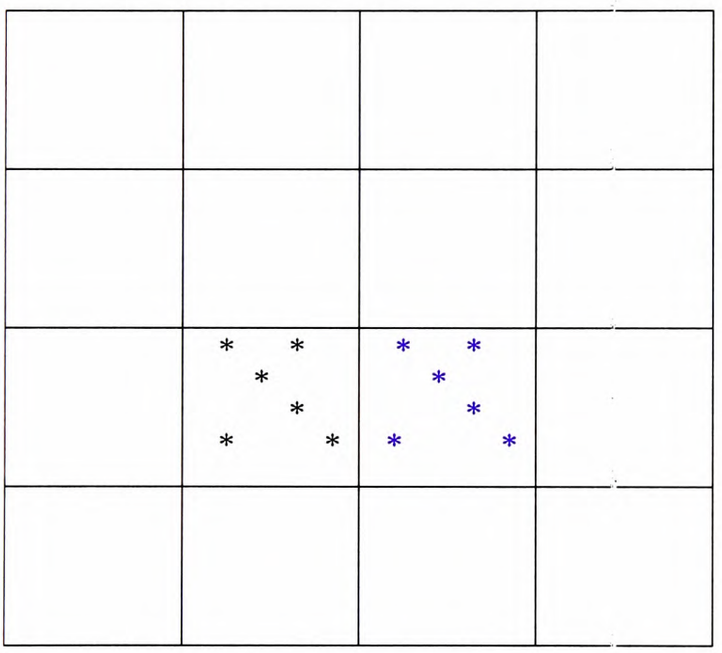

Periodic boundary conditions used in the Molecular Dynamics

Constant volume ensemble with fixed number of particles and periodic boundary conditions compensating for the surface effect.

Figure 1.3: Periodic boundary conditions

this case the computer code will be much more complicated.

1.4.4 Minimum Image Convention

The force subroutine is the main subroutine determining the run time of an MD simulation. This is the force experienced by each atom within the central simulation cell due to all the other (N-1) atoms. Furthermore, there are also the interactions between the atoms in the simulation box and the periodic images of the (N-1) particles in all the other periodic cells. Clearly this is an infinite number of interactions. To overcome this problem, an approximation called *the minimum image convention* [13] has been devised in which a given particle in the central box interacts with the *closest periodic images* of all the other particles in the adjacent cells. An N-particle system interacting in a pair-wise fashion under the minimum image convention requires $\frac{1}{2}N(N-1)$ interactions. This would still be a very large number if N is big. A further approximation to reduce the number of interactions is to apply a *cut-off* radius to the potential which will limit the interactions to those pairs which lie within the cut-off range. In the case of metals, a suitable cut-off radius would be equivalent to 2 or 3 lattice parameters, which is long enough to consider all the quantitatively important pair-wise interactions. By combining the cut-off method and the minimum image convention, we can substantially reduce the run time of a simulation.

1.4.5 Neighbour List

We can use the cut-off radius to produce a neighbour list for each particle in the system [13, 16]. The Verlet neighbour method can be used to create the neighbour list. At the beginning of the run, all the pairs with an interatomic distance smaller than the imposed cut-off will be stored in an array. A second array, storing the addresses for the beginning and the end of each particle's neighbour list is also created. Several methods of creating such a list exist [13]. The list is updated at each time step. However, for a slow moving system, the list can be updated after many time steps.

1.4.6 General Implementation of an MD Simulation

In an MD simulation, we must first select a statistical-mechanical ensemble which is appropriate for the problem under investigation. The model-system must then be *equilibrated* so that the simulation starts with a system that has *no memory*. The periodic boundary conditions and the cut-off are applied. The initial positions of the atoms and their velocities must be supplied. These initial velocities are generated in accordance with Maxwell-Boltzmann distribution with random orientations, and the initial positions reflect the geometry of the phase under consideration.

1.4.6.1 Interatomic potentials

Interatomic potentials lie at the basis of any MD simulation. They encapsulate the physics of the problem at hand. A great deal of effort has been spent over many years in developing appropriate potentials to model the physics of various classes of materials.

In this Section, we consider the pertinent interatomic potentials used for the metallic systems studied in this Thesis. Metallic bonding operates over the range of 0.2 to 0.5 nm [17]. For large interatomic distances, the predominant force arises due to van der Waals interactions, which is responsible for long range cohesion[17]. Metallic bonding, like covalent bonding, is due to the sharing of the electrons in the system, and hence a proper description of this bonding requires the consideration of the many-body effects.

Potentials employed in this Thesis are both of two-body and many-body types. These consist of the two-body Lennard-Jones potential and the many-body Finnis-Sinclair type potentials [18] due to Sutton and Chen [19] and Rafii-Tabar and Sutton [20], and Murrell-Mottram [21, 22] two-plus-three body potentials for elemental materials and their binary alloys.

1.4.6.2 Lennard-Jones potential

This potential is one of the simplest and oldest potentials which has been developed. It models the van der Waals force which originates from the dipole-dipole interactions [13], and leads to an attractive force between the atoms which is on average non-zero [17].

The Lennard-Jones potential has the general form

$$U^{LJ} = 4\epsilon \sum_{i,j} \left[\left(\frac{\sigma}{r_{ij}} \right)^{12} - \left(\frac{\sigma}{r_{ij}} \right)^{6} \right], \tag{1.18}$$

where r_{ij} is the separation of atom i from atom j, σ is the hard sphere distance between i and j, and ϵ is the depth of the potential at equilibrium [17, 13].

The problem with this kind of potential is that it can only properly model the rare gas elements, such as Argon [13, 17]. Other atomic elements, especially the metals, cannot be adequately described by pair-wise potentials for the following reasons [23, 24]

- For most cubic metals, the ratio of C_{12} to C_{44} elastic constants is far from unity, but a pair-wise potential leads to the Cauchy relation, $C_{12} = C_{44}$, between these constants, which is not valid for metals.

- The prediction of the un-relaxed vacancy formation energy gives values around the cohesive energy which is completely wrong for metals. The relaxation energy for metals is quite small and the experimental data suggest that the vacancy formation energy for metals is about one third of the cohesive energy [24].

- The interatomic distance between the first and second atomic layers within an unreconstructed surface structure (bulk cross section) is predicted to be expanded by pair-wise potentials. This is opposite to the experimental data which suggest a contraction of the open surface's lattice spacing.

- Pair-wise potentials overestimate the melting point by up to 20% of the experimental value.

- Potentials with a functional form having only one optimum at the diatomic equilibrium distance cannot be fitted properly to phonon frequencies.

Two approachs have been proposed to improve these potentials by introducing a new term which accounts for the many-body effects. The first approach is to introduce three-body and

four-body terms with appropriate functional forms and symmetries, and the second approach is to introduce a term which is a functional of the *local density* of a given atom. This latter approach has led to several potentials, such as the Emebded-Atom Model [25, 26, 27], the Finnis-Sinclair [18] and the Sutton-Chen [19] potentials. The first approach is used in the Murrell-Mottram potentials [23] .

1.4.6.3 The Sutton-Chen potentials for FCC elemental metals

Sutton-Chen potentials [19] were proposed for the description of interatomic interactions of the ten FCC elemental metals. These potentials are based on the Finnis-Sinclair [18] methodology and have therefore the functional form

$$U_{tot} = \epsilon \left[\frac{1}{2} \sum_{i \neq j} \sum_{j} V(r_{ij}) - c \sum_{i} \sqrt{\rho(r_{ij})} \right] , \tag{1.19}$$

where the functions $\rho(r)$ and $V(r)$ are defined as *power laws*

$$V(r) = (\frac{a}{r})^n , \tag{1.20}$$

and

$$\rho_i = \sum_{j \neq i} (\frac{a}{r_{ij}})^m , \tag{1.21}$$

therefore the potential is given by:

$$U_{tot} = \epsilon \left[\frac{1}{2} \sum_{i \neq j} \sum_{j} (\frac{a}{r_{ij}})^n - c \sum_{i} \sqrt{\sum_{j \neq i} (\frac{a}{r_{ij}})^m} \right] , \tag{1.22}$$

where r_{ij} is the distance between atom i and atom j, c is a positive dimensionless parameter, ϵ is a parameter with the dimension of energy, a is a parameter with the dimension of length, generally fitted to the lattice parameter, and (n, m) are positive constants. The choice of a power law for the ρ function is based on the fact that for large interatomic distances, ρ will behave as a pair additive potential mimicking the van der Waals behaviour and at short interatomic distances it behaves like a many-body potential and the passage between these

two limits is quite smooth (continuous function) [19].

In order to investigate the behaviour of these potentials, let us consider a free surface and a single atom belonging to this surface. Its contribution to the cohesive energy of the surface is given by [19]:

$$u^s = -\epsilon c\sqrt{\rho^s}\,, \tag{1.23}$$

where ρ^s is the value of ρ given by (1.21). Now, if we consider an additional atom above the surface at a distance R from the surface, the new value of u^s will be given by [19]

$$u^s = -\epsilon c\left[\rho^s + (\frac{a}{R})^m\right]^{1/2}. \tag{1.24}$$

If R is very large (long interatomic distances), the square root can be approximated by its first term of the Taylor series which is

$$\sqrt{\rho^s} + \frac{(\frac{a}{R})^m}{2\sqrt{\rho^s}}. \tag{1.25}$$

Therefore, we see that by choosing m around 6, for large distances, the attractive term behaves as a van der Waals potential and at short distances as the approximation becomes more and more irrelevent, the many body aspect takes over [19]. The parameters used in this potential have been fitted using the cohesive energy, lattice parameter and elastic coefficients of different FCC elemental metals, and therefore a table is available for the potential usage within a program.

The last point to consider is that the elastic stability of a metallic crystal , which implies that $C_{44} > 0, C_{11} > 0$ and $C_{11} > C_{12}$. For Sutton-Chen potentials this condition is satisfied with $n > m$ [20].

1.4.6.4 The Murrell-Mottram potentials for the Sn, Pb and Al

The Murrell-Mottram potentials consist of pair-wise and three-body interactions. They are written in the form:

$$U_{tot} = \sum_i \sum_{j>i} U_{ij}^{(2)} + \sum_i \sum_{j>i} \sum_{k>j} U_{ijk}^{(3)}. \tag{1.26}$$

The pair interaction term satisfies the conditions of a diatomic potential of stable diatomic molecules and therefore it has few parameters [21, 23] . The *Rydberg function* was used for the functional form of the two-body interaction term [21, 22, 23]. In the units of reduced energy and distance [13]

$$\frac{U_{ij}^{(2)}}{D} = -(1 + a_2\rho_{ij})e^{-a_2\rho_{ij}}\,, \tag{1.27}$$

where

$$\rho_{ij} = \frac{r_{ij} - r_e}{r_e}. \tag{1.28}$$

D is the depth of the potential well which corresponds to the diatomic dissociation energy at $\rho_{ij} = 0$, which in turn corresponds to $r_{ij} = r_e$, with r_e the diatomic equilibrium distance. These are fitted to bulk cohesive energy and lattice parameter respectively. The only parameter involved in optimisation of the potential is the parameter a_2, which is related to the curvature and therefore the force constant of the potential at its minimum [21, 22, 23] . The three-body term must be symmetric to permutation of the three indices i, j and k. The most convenient way to achieve this is to create functional forms which are combinations of interatomic coordinates Q_1, Q_2 and Q_3. This choice is justified based on the fact that these coordinates are the irreducible representations of the S_3 permutation group [28] . If we consider a given triangle with atoms a_i, a_j and a_k, the coordinates Q_i, (i=1,3) are given by

$$\begin{bmatrix} Q_1 \\ Q_2 \\ Q_3 \end{bmatrix} = \begin{vmatrix} \sqrt{1/3} & \sqrt{1/3} & \sqrt{1/3} \\ 0 & \sqrt{1/2} & -\sqrt{1/2} \\ \sqrt{2/3} & -\sqrt{1/6} & -\sqrt{1/6} \end{vmatrix} \begin{bmatrix} \rho_{ij} \\ \rho_{jk} \\ \rho_{ki} \end{bmatrix}, \tag{1.29}$$

with $\rho_{ij} = \frac{r_{ij}-r_e}{r_e}$ and r_{ij} representing one of the three triangle edges. These interatomic coordinates have specific geometrical meanings, Q_1 represents the perimeter of the triangle in reduced units, Q_2 and Q_3 represent the distortion factors from an equilateral geometry [23]. Any polynomial form which is totally symmetric in ρ_{ij} can be expressed as sums of products of the integrity basis [23], defined as three expressions as follows

$$Q_1\ , Q_2^2 + Q_3^2\ , Q_3^3 - 3Q_3Q_2^2\,. \tag{1.30}$$

A last condition that must be imposed on the three-body term is that it must go to zero if one of the atoms goes to infinity. It means that large triangle perimeters correspond to large Q_1 values. Therefore, the following form was chosen for the three-body part

$$\frac{U_{ijk}^{(3)}}{D} = P(Q_1, Q_2, Q_3)F(a_3, Q_1)\,, \tag{1.31}$$

where $P(Q_1, Q_2, Q_3)$ is a polynomial in the Q coordinates and F is a damping function which decays exponentially at long range. The damping function is considered as an exponential having a parameter a_3 and therefore it will determine the range of the three-body potential. Three different kinds of damping function can be used:

$$\begin{aligned} F(a_3, Q_1) &= \quad exp(-a_3Q_1)\,, \quad && exponential\,, \\ F(a_3, Q_1) &= \tfrac{1}{2}\left(1 - tanh(\tfrac{a_3Q_1}{2})\right)\,, && tanh\,, \\ F(a_3, Q_1) &= \quad sech(a_3Q_1)\,, && sech\,. \end{aligned} \tag{1.32}$$

Using the exponential damping function leads in some cases to lattice instabilities for the following reason. The Rydberg function used as the functional form of the two-body potential does not go to infinity if the interatomic distance goes towards zero. It will be a very big value but not infinity [23]. Having this fact in mind, let us consider a very small triangle for which $r_{ij} + r_{jk} + r_{ki} << 3r_e$, in this situation the damping factor would be quite big and if the polynomial P is negative for this small triangle, the overall three-body potential can overcome the two-body part and therefore create a lattice instability and the collapse of the system. To

avoid such a situation, it is necessary to add a *hard wall* function to the two-body repulsive part to make it go to infinity when the interatomic distance tends to zero [23].
The polynomial is given by

$$\begin{aligned} P(Q_1,Q_2,Q_3) = \; & c_0 + c_1 Q_1 + c_2 Q_1^2 + c_3(Q_2^2+Q_3^2) + c_4 Q_1^3 \\ & + c_5 Q_1 (Q_2^2+Q_3^2) + c_6 (Q_3^3 - 3Q_3 Q_2^2) \end{aligned} \quad . \tag{1.33}$$

There are seven parameters to be fitted using the experimental data on phonon frequencies and elastic coefficients. For metallic systems having two different solid phases, four more terms corresponding to quartic terms in the polynomial can be added as

$$c_7 Q_1^4 + c_8 Q_1^2 (Q_2^2+Q_3^2) + c_9 (Q_2^2+Q_3^2)^2 + c_{10} Q_1 (Q_3^3 - 3Q_3 Q_2^2) \tag{1.34}$$

So far, all the potentials that have been constructed, have been applied to simple *elemental materials.* Further on in this Chapter we shall study different mixing rules which we have devised in order to apply the same functional forms to the construction of *binary alloy* potentials.

1.4.7 Binary alloy potentials

In order to construct interatomic potentials to model the energetics and dynamics of binary alloys, based on the use of elemental metal potentials, we need to make use of several *mixing rules* which allow for the computation of an alloy potential parameters from those of the elemental materials. These rules are based on different averaging methods, such as the arithmetic or geometric averages. For the Sutton-Chen elemental potentials, these rules have already been obtained by Rafii-Tabar and Sutton in constructing long-range binary alloy potentials for FCC metals [20]. The rules applied to the Murrell-Mottram elemental potentials are specifically constructed in this Thesis.

1.4.7.1 Rafii-Tabar and Sutton fcc binary alloy potentials

The potential is given by

$$\begin{aligned} H = \; & \tfrac{1}{2}\left[\textstyle\sum_{i\neq j}\sum_j \wp_i\wp_j V^{AA}(r_{ij}) + (1-\wp_i)(1-\wp_j)V^{BB}(r_{ij})\right. \\ & + \left[\wp_i(1-\wp_j)+\wp_j(1-\wp_i)\right]V^{AB}(r_{ij}) \\ & -d^{AA}\textstyle\sum_i \wp_i\left[\sum_{j\neq i}\wp_j\Phi^{AA}(r_{ij}) + (1-\wp_j)\Phi^{AB}(r_{ij})\right]^{1/2} \\ & \left.-d^{BB}\textstyle\sum_i(1-\wp_i)\left[\sum_{j\neq i}(1-\wp_j)\Phi^{BB}(r_{ij}) + \wp_j\Phi^{AB}(r_{ij})\right]^{1/2}\right. \end{aligned} \quad . \tag{1.35}$$

The operator $\wp_i$ is a site occupancy operator and is defined as

$$\wp_i = \begin{cases} 1, & \text{if the site } i \text{ is occupied by an atom A} \\ 0, & \text{if the site } i \text{ is occupied by an atom B} \end{cases} \quad . \tag{1.36}$$

The functions $V^{\alpha\beta}$ and $\Phi^{\alpha\beta}$ are defined as

$$\begin{aligned} & V^{\alpha\beta}(r) = \epsilon^{\alpha\beta}\left[\tfrac{a^{\alpha\beta}}{r}\right]^{n^{\alpha\beta}}, \\ & \Phi^{\alpha\beta}(r) = \epsilon^{\alpha\beta}\left[\tfrac{a^{\alpha\beta}}{r}\right]^{m^{\alpha\beta}}, \\ & \text{where } \alpha \text{ and } \beta \text{ are both A or B}. \end{aligned} \tag{1.37}$$

In this model, values of ϵ^{AA} , c^{AA} , a^{AA} , m^{AA} and n^{AA} are set to those of element A and ϵ^{BB} , c^{BB} , a^{BB} , m^{BB} and n^{BB} are set to those of element B.

$$d^{AA} = \epsilon^{AA}c^{AA}, \tag{1.38}$$

$$d^{BB} = \epsilon^{BB}c^{BB}. \tag{1.39}$$

The mixing rules defined for this potential are based on the assumption that the functions V^{AB} and Φ^{AB} may be expressed as:

$$V^{AB} = (V^{AA}V^{BB})^{1/2}, \tag{1.40}$$

$$\Phi^{AB} = (\Phi^{AA}\Phi^{BB}). \tag{1.41}$$

Therefore, we can express the alloy parameters as

$$\begin{aligned} m^{AB} &= \tfrac{1}{2}(m^{AA} + m^{BB}) , \\ n^{AB} &= \tfrac{1}{2}(n^{AA} + n^{BB}) , \\ a^{AB} &= (a^{AA} a^{BB})^{1/2} , \\ \epsilon^{AB} &= (\epsilon^{AA} \epsilon^{BB})^{1/2} . \end{aligned} \tag{1.42}$$

The assumption of using a geometrical average for V and Φ are purely empirical. These potentials have the advantage that all the parameters for the alloys can be obtained from the parameters for the elemental metals *without* the introduction of any new parameters.

1.4.7.2 Murrell-Mottram potential for Sn-Pb, Al-Sn and Al-Ni binary alloys

The Murrell-Mottram potential applied to binary alloys has three terms for the two-body interactions and eight terms for the three-body interactions. To obtain a realistic mixing rule, several rules were tried by fitting to the experimental value of enthalpy of formation.

1.4.7.2.1 Derivation of the mixing rule A rule involving 14 different parameters (the total number of the coefficients used in the two-body and three-body parts of the Murrell-Mottram potential) was searched for. As these parameters had positive or negative values, two different approaches were used. The first approach was based on allocating separately the sign and the absolute value, since there was a sign ambiguity when computing a geometrical average. The second approach was to allocate sign and absolute values at the same time by using averages which would not lead to a sign ambiguity. A list of these rules is (the averaging rules are common practice in MD as used by Rafii-Tabar et al. [20] for fcc binary alloys)

- **Rule 1:** Geometric average for D, c_0 to c_6 and arithmetic average for r_e , a_2 and a_3 and arithmetic average for r_e , a_2 and a_3 . As c_7 to c_{10} are only used for elements capable of allotropic transformation, these values are set to those related to the corresponding element with allotropic transformation. The sign assignment was the sign of the parameter with the highest absolute value.

- **Rule 2:** Geometric average for D, c_0 to c_{10} and arithmetic average for r_e, a_2 and a_3 . The sign assignment was as in rule one.

- **Rule 3:** The same averaging rules as in rule two but the sign assignment was as follows: for the two-body part of the potential, the same as in rule one but for the three-body part of the potential, the sign allocated would be the one corresponding to the atom which has the majority of atoms over a set of three.

- **Rule 4:** Arithmetic average was used for all parameters.

- **Rule 5:** Arithmetic average for c_0 to c_{10} and for a_3 and geometric average for D , r_e and a_2

- **Rule 6:** The same as rule 5 except that an arithmetic average has been used for a_2 .

All the above rules were tested and the best fit was obtained using rule 5, which was adopted for this study.

1.5 MD simulation of a canonical ensemble

The simulation of a system with a constant number of particles, N, confined to a fixed volume, V, and maintained at a constant preset temperature, T, is implemented within the framework of a constant (N, V, T), or canonical, ensemble. The temperature acts as a control parameter. Such a constant- temperature ensemble can be realised in a variety of ways [29]

- Direct velocity scaling([13])

- Berendsen's method of temperature control([31])

- The Andersen method([32])

- Nosé-Hoover dynamics([33])

The Nosé-Hoover (N-H) dynamics [30, 33] was adopted as the temperature- control procedure in our simulations. The reason behind this choice is the fact that Nosé-Hoover dynamics can

generate true canonical ensembles in real space as well as the phase space. The partition function of the microcanonical ensemble of the virtual system is equivalent to the partition function of the canonical ensemble of the real system [14].

1.5.1 Nosé-Hoover dynamics

This method of temperature control is based on coupling a *thermostat* to the simulated system. The method is implemented by introducing an additional, or *phantom*, degree of freedom which is coupled to the real physical system, and the system is then referred to as an *extended* system. The fictitious degree of freedom acts as a heat bath for the real particles [14, 34], and a mass, $\mathcal{Q}$, is associated with it. The Hamiltonian function of the extended system is given by [14, 30, 34, 35]

$$H^* = \sum_{i=1}^{N} \frac{p_i^2}{2m_i s^2} + U(\mathbf{q}) + \frac{p_s^2}{2\mathcal{Q}} + gk_BT \ln s\,, \tag{1.43}$$

where p_i is the momentum for the virtual system, $\mathbf{q}$ is the coordinate for the virtual system, s is the fictitious coordinate associated with the extra degree of freedom, p_s is its conjugate momentum, g is the number of degrees of freedom and k_B is the Boltzmann constant. From this Hamiltonian the equations of motion of the particles in the system are obtained [14, 34, 35]

$$\begin{aligned} \frac{d\mathbf{q_i}}{dt} &= \frac{\mathbf{p_i}}{m_i} \\ \frac{d\mathbf{p_i}}{dt} &= -\frac{dU}{d\mathbf{q_i}} - \zeta p_i \\ \frac{d\zeta}{dt} &= \frac{\sum_i \frac{p_i^2}{m_i} - gk_BT}{\mathcal{Q}} \end{aligned}\,, \tag{1.44}$$

where ζ is the friction coefficient of the heat bath and T is the thermostat temperature. The friction coefficient is not a constant and can take on both positive and negative values. The last equation controls the functioning of the heat bath. From this equation we see that if the total kinetic energy of the N- particle system is greater than $gk_BT/2$ then $\frac{d\zeta}{dt}$, and hence ζ, is positive. This creates a friction inside the bath and hence the motion of the particles are decelerated to lower their kinetic energy to that of the bath. On the other hand, if the kinetic energy is lower than $gk_BT/2$, then ζ will be negative. This results in the bath being heated

up and accelerate the motion of the particles. The above set of equations are referred to as the *Nosé-Hoover thermostat.*

1.5.2 Velocity-Verlet implementation of the N-H thermostat

To implement the N-H thermostat within an MD simulation, we need to substantially modify the velocity verlet algorithm, eqns. (1.16) and (1.17). The modified velocity-Verlet equations are given by [34]

$$\begin{aligned}
&\mathbf{r}_i(t+\delta t) = \mathbf{r}_i(t) + \delta t \mathbf{v}_i(t) + \tfrac{\delta t^2}{2}\left(\tfrac{\mathbf{F}_i(t)}{m} - \zeta(t)\mathbf{v}_i(t)\right) . \\
&\text{The velocities } \mathbf{v} \text{ and the value of } \zeta \text{ at time } t+\delta t \text{ are obtained as follows} \\
&\mathbf{v}_i(t+\tfrac{\delta t}{2}) = \mathbf{v}_i(t) + \tfrac{\delta t}{2}\left(\tfrac{\mathbf{F}_i(t)}{m} - \zeta(t)\mathbf{v}_i(t)\right) , \\
&\zeta(t+\tfrac{\delta t}{2}) = \zeta(t) + \tfrac{\zeta}{2\mathcal{Q}}\left(\textstyle\sum_{i=1}^{N} m_i \mathbf{v}_i^2(t) - g k_B \tau\right) . \\
&\text{These equations allow the evaluation of } \zeta(t+\delta t) \text{ , which is given by} \\
&\zeta(t+\delta t) = \zeta(t+\tfrac{\delta t}{2}) + \tfrac{\delta t}{2\mathcal{Q}}\left(\textstyle\sum_{i=1}^{N} m_i \mathbf{v}_i^2(t+\tfrac{\delta t}{2}) - g k_B \tau\right) .
\end{aligned} \tag{1.45}$$

The velocities at time $t+\delta t$ satisfy:

$$\mathbf{v}_i(t+\delta t) = \mathbf{v}_i(t+\frac{\delta t}{2}) + \frac{\delta t}{2}\left(\frac{\mathbf{F}_i(t+\delta t)}{m} - \zeta(t+\delta t)\mathbf{v}(t+\delta t)\right) , \tag{1.46}$$

from which we obtain

$$\mathbf{v}_i(t+\delta t) = \frac{2}{2+\delta t \zeta(t+\delta t)}\left(\mathbf{v}_i(t+\frac{\delta t}{2}) + \delta t \frac{\mathbf{F}_i(t+\delta t)}{2m}\right) . \tag{1.47}$$

In above expressions, $\mathbf{F}_i$ is the force experienced by a given particle. A particular parameterisation of $\mathcal{Q}$ is given by

$$Q = g k_B T \tau^2 , \tag{1.48}$$

where τ is the relaxation time of the heat bath. It controls the speed with which the bath damps down the fluctuations in the temperature. The number of degrees of freedom is given by $g = 3(N-1)$.

1.6 Detection of phase transitions

All phase transitions can be defined by the change that normally occurs in the order of the system while the transition takes place [9]. Thus, studying and detecting a phase transition imply a measurement of the order or disorder of the molecular system [9, 16]. There are several ways of measuring or evaluating the orderliness of a system either via experiments or theoretical calculations. Our approach to this problem is based on the evaluation of three important parameters, characterising the order of a crystalline structure (as indicated in [16])

- *Distribution functions*,
- *Translational order parameters*, and
- *Running mean square displacement.*

These quantities can provide the necessary information on local molecular or atomic arrangements and therefore the degree of internal order of the system [9].

1.6.1 Distribution functions

Distribution functions can be obtained in different ways. We can create models to compute them or conduct experiment on real materials, or even obtain them from theoretical first principle calculations [13, 16]. One must always distinguish between Green functions and distribution functions as the former represents the propagation of the property under investigation from a given source and the latter is related to how neighbouring particles are structured locally [9] .

Consider N fixed identical particles confined in a volume V. The position vectors of the centres of these particles are denoted by $\mathbf{R}_i$. The number density is

$$n_0 = \frac{N}{V}\,. \tag{1.49}$$

If there is no interpenetration or coincidences between different particles, then each point in space can only be occupied by one particle [13, 16]. By using the Dirac δ-functions we can

define the *single-particle density functions*

$$\nu^{(1)}(\mathbf{r}) = \sum_{i=1}^{N} \delta(\mathbf{r} - \mathbf{R}_i)\,. \tag{1.50}$$

Therefore, $\int \nu^{(1)}(\mathbf{r})d\mathbf{r} = N$. These Dirac δ-functions represent the occupancy functions for site $\mathbf{R}_i$ [13, 16]. We can also define the *two-particle density functions* [13, 16]

$$\nu^{(2)}(\mathbf{r_1}, \mathbf{r_2}) = \sum_{i=1}^{N} \sum_{j \neq i} (N-1)\delta(\mathbf{r_1} - \mathbf{R}_i)\delta(\mathbf{r_2} - \mathbf{R}_j). \tag{1.51}$$

This function is equal to zero unless we have simultaneously the particle 1 at $\mathbf{R}_i$ and particle 2 at $\mathbf{R}_j$. By integrating over $\mathbf{r_2}$ each time that we have $\mathbf{r_2} = \mathbf{R}_j \neq \mathbf{r}_i$ there will be a non-zero contribution of Dirac δ- function related to $\mathbf{r_2}$. Therefore, the integral will be equal to [13, 16]

$$\int \nu^{(2)} d\mathbf{r_2} = (N-1) \sum_{i=1}^{N} \delta(\mathbf{r_1} - \mathbf{R}_i) = (N-1)\nu^{(1)}(\mathbf{r_1}). \tag{1.52}$$

In the case of real physical systems, particles are atoms and molecules and therefore due to thermal agitations they cannot be considered as fixed in space. This means that in all the above formulae, we have to replace all the values by their respective ensemble averages [13, 16]. Thus denoting $\left\langle \nu^{(1)}(\mathbf{r}) \right\rangle$ by $n^{(1)}(\mathbf{r})$, the expression $n^{(1)}(\mathbf{r})d\mathbf{r}$ will be the average number of atoms and molecules which are centred in $d\mathbf{r}$. But, since the particles cannot coincide, therefore $n^{(1)}(\mathbf{r})d\mathbf{r}$ will be the probability to find a particle within $d\mathbf{r}$. This means that $\int_V n^{(1)}(\mathbf{r})d\mathbf{r} = N$. We therefore call $n^{(1)}(\mathbf{r})d\mathbf{r}$ the *number density function* or the *one-particle distribution function.*

By averaging in the same way over $\mathbf{r_2}$ for the two-particle density function, we can find the *two-particle distribution function*

$$d\mathbf{r_1} \int_V n^{(2)}(\mathbf{r_1}, \mathbf{r_2})d\mathbf{r_2} = (N-1)n^{(1)}(\mathbf{r_1})d\mathbf{r_1}. \tag{1.53}$$

Due to the fact that the probability of occupation for particle 2 is not independent of the probability of occupation for particle 1, because of the interatomic interactions which exist

between different particles, we have[13, 16]

$$n^{(2)}(\mathbf{r_1}, \mathbf{r_2}) \neq n^{(1)}(\mathbf{r_1}) n^{(1)}(\mathbf{r_2}). \tag{1.54}$$

We can therefore define a *pair-distribution function* as a proportionality factor

$$n^{(2)}(\mathbf{r_1}, \mathbf{r_2}) = n^{(1)}(\mathbf{r_1}) n^{(1)}(\mathbf{r_2}) g^{(2)}(\mathbf{r_1}, \mathbf{r_2}). \tag{1.55}$$

In the case of a homogeneous system, the number density function value is independent of the particle position and is equal to the number density

$$n^{(1)}(\mathbf{r_1}) = n^{(2)}(\mathbf{r_2}) = n_0. \tag{1.56}$$

Therefore the two-particle distribution function can be written as

$$n^{(2)}(\mathbf{r_1}, \mathbf{r_2}) = n_0^2 g^{(2)}(\mathbf{r_1}, \mathbf{r_2}). \tag{1.57}$$

The integration of the pair-distribution function over the position vector, considering $\mathbf{r} = \mathbf{r_2} - \mathbf{r_1}$ and $\mathbf{r_1}$ at the origin, yields

$$n_0 \int g(2)(\mathbf{r}) d\mathbf{r} = N - 1. \tag{1.58}$$

The interpretation of this equation is that the value $n_0(2)g(2)(\mathbf{r})d\mathbf{r}$ gives the probability of finding a particle at a point $d\mathbf{r}$ which is at a distance $\mathbf{r}$ from another particle centred at the origin. For isotropic systems, we have $g^{(2)}(\mathbf{r}) = g^2(\mid \mathbf{r} \mid) = g(r)$. It is always possible to define higher order distribution functions and to obtain more details about the structure of the system, *but experimentally only the pair-distribution function can be obtained* [13, 16]. If we consider a spherical shell with thickness $d\mathbf{r}$ and centred on a particle at the origin, we can write

$$\int_{shell} n_0 g(r) dr = 4\pi r^2 n_0 g(r) dr = n_0 \rho(r) dr\,, \tag{1.59}$$

where $\rho(r) = 4\pi r^2 g(r)$ is called the *Radial Distribution Function* . We can determine the *coordination number*, or the number of nearest neighbours, by integrating the radial distribution function over the distance r_n which is the nearest distance between any given pair in the system [13, 16]. Therefore the coordination number is

$$n_1 = n_0 \int_0^{r_n} \rho(r) dr \,. \tag{1.60}$$

1.6.2 MD-based computation of radial distribution functions

For an N-particle in a volume V, with the number density n_0 and the radial distribution function $\rho(r)$, we have

$$n_0 \rho(r) = \frac{1}{N} \left\langle \sum_{i=1}^{N} \sum_{j \neq i}^{N} \delta(\mathbf{r} - \mathbf{r_{ij}}) \right\rangle \,. \tag{1.61}$$

Here the average defined is a time average, and $\mathbf{r_{ij}}$ is the distance between atoms i and j [13, 16]. As was mentioned previously, for homogeneous and isotropic systems the structural arrangement of particles is only a function of the distance r between two particles and the orientation of the separation vector does not have to be taken into consideration. Therefore

$$n_0 \rho(r) = \frac{1}{N} \left\langle \sum_{i=1}^{N} \sum_{j \neq i}^{N} \delta[r - r_{ij}] \right\rangle \,, \tag{1.62}$$

and since $r_{ij} = r_{ji}$, the sum can be written as

$$n_0 \rho(r) = \frac{2}{N} \left\langle \sum_{i=1}^{N} \sum_{j > i}^{N} \delta(r - r_{ij}) \right\rangle . \tag{1.63}$$

Normalisation of the radial distribution function leads to [13, 16]

$$n_0 \int \rho(r) d\mathbf{r} = \frac{2}{N} \left\langle \sum_{i=1}^{N} \sum_{j > i}^{N} \int \delta(r - r_{ij}) d\mathbf{r} \right\rangle = (N - 1) \approx N. \tag{1.64}$$

This formula expresses the fact that if we sit on one atom and count the atoms in the system, we will find $(N - 1)$ atoms [13, 16]. Therefore if we consider an atom over which we create an

spherical shell of radius r and thickness Δr, the probability to find an atomic centre within this shell is given by

$$\frac{n_0}{N-1}\rho(r)V(r,\Delta r). \tag{1.65}$$

In this formula, $V(r,\Delta r)$ is the volume of the spherical shell. Therefore, the radial distribution function can be considered as a time-averaged influence of one atom over its neighbouring atomic positions [13, 16]. Two important consequences are that, first of all as we cannot find any two particles having a distance less than an atomic diameter, for distances less than one atomic distance the value of $\rho(r)$ is equal to zero, and the second consequence is that for large separations in fluids, no atom has any influence over other atoms' positions and therefore the value of $\rho(r)$ will be equal to one.

Let us now consider how a radial distribution function is computed in an MD simulation. Using a finite shell thickness, Δr, we can rewrite the eqn. (1.69) as [16]

$$n_0 \sum_{\Delta r} g(r)V(r,\Delta r) = \frac{2}{N}\sum_{\Delta r}\left\langle \sum_{i=1}^{N}\sum_{j>i}^{N}\delta(r-r_{ij})\Delta\mathbf{r}\right\rangle. \tag{1.66}$$

We can transform the double sum to a counter operator [9] and therefore write

$$\sum_{i=1}^{N}\sum_{j>i}^{N}\delta[r-r_{ij}]\Delta\mathbf{r} = N(r,\Delta r). \tag{1.67}$$

Here the term $N(r,\Delta r)$ represents the number of atomic centres found in a spherical shell of radius r and thickness Δr with the centre on another atom [16]. As the equation must be satisfied term by term and for any thickness, therefore we can deduce

$$\rho(r) = \frac{< N(r,\Delta r) >}{\frac{1}{2}Nn_0V(r,\Delta r)}. \tag{1.68}$$

Now if we write the time average explicitly as the number of time steps for which we have run the simulation, the result will be [16]

$$\rho(r) = \frac{\sum_{k=1}^{M} N_k(r,\Delta r)}{M(\frac{1}{2}N)n_0V(r,\Delta r)}. \tag{1.69}$$

In this expression, $N_k(r, \Delta r)$ is the result of counting operation at time step t_k in the run. This expression can be interpreted as a ratio between a local density $n(r)$ and the system density which is n_0.

What is very important for a reliable and precise evaluation of the radial distribution function is the choice of the value of the thickness [16]. This must be small enough in order to capture the detailed internal structure of the system and at the same time large enough in order to sample a large population for a reliable statistical data. A value such as $\Delta r = 0.025\sigma$ (σ is the lattice parameter) is a good compromise for the radius thickness. The radial distribution function for a crystalline structure at $0K$ is a set of Dirac δ-functions representing the internal structure of the crystal [16]. At non-zero K temperatures, these functions will be transformed into sharp Gaussians due to thermal agitations [16]. These Dirac δ- or Gaussian, functions are a clear manifestation of the fact that within crystalline structures the local density is not constant and, based on the crystallographic structure, we get different spectrum of these localised density profiles with various heights. For a liquid, in contrast to a solid, we may observe a continuous spectrum, confirming the fact that the local density is uniform throughout the system.

The radial distribution function is a powerful tool to distinguish between the liquid and solid states and also between different crystalline structures [16].

1.6.3 MD-based computation of translational order parameter

In order to study the positional order and disorder in a solid system we can define a translational order parameter which will represent the occupancy of different lattice sites [16]. Here we consider the order parameter of an FCC lattice structure. Other expressions can be found for other lattice structures. The translational order parameter is defined by

$$\lambda = \frac{1}{3}\left[\lambda_x + \lambda_y + \lambda_z\right] , \tag{1.70}$$

where λ_α is defined as

$$\lambda_\alpha = \frac{1}{N}\sum_{i=1}^{N} \cos\left(\frac{4\pi\alpha_i}{a}\right), \tag{1.71}$$

with $\alpha = (x, y, z)$ and a is the lattice parameter of the FCC system [16]. For a solid, $\lambda = 1$ because the positional components, α_i, are all integer multiples of $\frac{1}{2}a$. For a liquid, the parameter will fluctuate around zero as the atoms are distributed randomly about the original lattice sites [16] . As the magnitude of the oscillation is $\frac{\sqrt{N}}{N}$, the bigger the system, the smaller is the fluctuation. This order parameter is appropriate for liquid-to-solid phase transition but not the solid-to-liquid transition as the system does not release the heat as it adsorbes it [16].

1.6.4 Running mean square displacement (RMSD)

The RMSD is a measure of displacement of any given particle within the system during the phase transition [16]. For a solid, by definition, there must be no significant displacement of atoms or molecules within the system and, therefore, RMSD must be zero for a solid phase [16]. In contrast to a solid, the atoms and molecules within a liquid have certain amount of freedom to move around their original positions and, therefore, in going from the solid state to the iquid state the value of RMSD is increased. If the time origin is changed and the RMSD is averaged over it, a linear variation of RMSD for a liquid phase is obtained during the time [16]. RMSD is defined by

$$RMSD = \frac{1}{N}\sum_{i=1}^{N} \mid r_i^2(t) - r_i^2(0) \mid . \tag{1.72}$$

1.6.5 MD-based calculation of material properties during phase transition

Molecular dynamics provides us with a valuable tool for obtaining information about the thermal, mechanical, entropic, electromagnetic and chemical properties of different phases. These properties can be obtained by averaging specific run-time parameters over a long period of time [13, 16]. As these properties are macroscopic properties, we need to use a sufficeintly

large-scale system in order to obtain reliable results. Therefore, there is a need for large-scale molecular dynamics simulations[13, 16]. We focus on the thermo-mechanical properties of atomic systems.

An important parameter to study during any phase transition is the rate of creation of nuclei of the new phase per unit volume of the system. This value is called the *nucleation rate* [5, 8, 12]. Evaluation of the nucleation rate during a phase transition requires the computation of the surface tension and the chemical potential. To calcualte the chemicel potential, the *test particle method* [16] has been used.

1.6.6 The test-particle method

To evaluate the chemical potential, one needs to calculate the change in the Gibbs free energy of the system when the total number of particles present in the system varies ($\mu = \left(\frac{\partial G}{\partial N}\right)$) [14, 16] . The test-particle method is based on the calculation of the entropy variation of the system *when a new particle is added to the system.* The chemical potential is defined as

$$\mu = -T\left(\frac{\partial S}{\partial N}\right)_{EV}. \tag{1.73}$$

It is a reversible work which is related to the addition or substraction of a particle to or from, the system [16]. For a microcanonical ensemble we can write this as [16]

$$\begin{aligned} &\mu = -k_B T\left(\tfrac{\partial \Omega}{\partial N}\right)_{EV} \\ &\mu \approx -k_B T\left(\tfrac{\ln \Omega_{N+1} - \ln \Omega_N}{N+1-N}\right)_{EV} \approx -k_B T\left(\ln \tfrac{\Omega_{N+1}}{\Omega_N}\right)_{EV} \end{aligned}, \tag{1.74}$$

where Ω is the statistical potential (number of microstates in the ensemble). We need to transform the $\frac{\Omega_{N+1}}{\Omega_N}$ into a time average expression calculable by molecular dynamics. Using the test-particle potential, U_t, the instantaneous temperature, T_{ins}, the time average temperature, T, and the thermal de Broglie wavelength, Λ, we can write [16] :

$$\mu = -k_B T \ln\left[\frac{1}{\rho\Lambda^3 \left\langle k_B T_{ins}\right\rangle^{3/2}}\left\langle (k_B T)^{3/2} \exp\left[-\frac{U_t}{k_B T_{ins}}\right]\right\rangle\right], \tag{1.75}$$

where

$$\Lambda = \left(\frac{h^2}{2\pi m k_B T}\right)^{1/2}, \tag{1.76}$$

with h the Planck's constant and m the mass of the particle. What we are intrested in is the variation of the chemical potential at a given temperature and density. Therefore, as under these conditions the contribution of the ideal gas part remains constant [16], we remove it from the chemical potential and only consider the excess part, also called the residual chemical potential [16]

$$\mu_{res} = -k_B T \ln \left[\frac{1}{\langle k_B T_{ins}\rangle^{3/2}} \left\langle (k_b T)^{3/2} \exp\left[-\frac{U_t}{k_B T_{ins}}\right]\right\rangle\right]. \tag{1.77}$$

We have to keep in mind that the test particle method adds only a fictitious particle to the system and the dynamics of the system is unchanged by this insertion. Also the phase-space trajectory of the system remains intact [16]. Therefore, we can define the test-particle potential as the variation of the potential energy of the system before and after the introduction of the test particle which is equal to the sum of interactions between the test particle and the N real particles [16]. In reality, this is the amount of work that should have been provided if one wants to add a new particle to the system.

The position of the test particle influences the final result. Therefore, to obtain statistically reliable results for the time-average we need to introduce at each time step a randomly chosen set of test particles and to calculate for each one of them the test particle potential. Therefore, considering reduced variables (see [13]), the time average becomes [16]

$$\left\langle (T^*_{ins})^{3/2} \exp\left[-\frac{U^*_t}{T^*_{ins}}\right]\right\rangle = \frac{1}{M N_t} \sum_j^{N_t} \sum_k^{M} (T^*_{ins})^{3/2}\, exp\left[-\frac{1}{T^*_{ins}} \sum_i^{N} U^*_{ij}(k_B \Delta t)\right], \tag{1.78}$$

where N_t is the number of inserted particles at each time step and M is the total number of time steps. The reduced variables are shown using an $*$ as superscript. These insertions are done for randomly selected positions at each time step using a random number generator [13].

In a canonical ensemble, the expression for the residual chemical potential, i.e. the excess part, is much simpler than in the microcanonical ensemble due to the constancy of the

temperature. In this case we have [13]

$$\mu_{res} = -k_B T \ln \left\langle \exp\left(-\frac{U_t}{k_B T}\right) \right\rangle . \tag{1.79}$$

To implement the test-particle method in a canonical ensemble, at each time step we use a random number generator to create new positions for a set of particles to be inserted into the system. The test-particle potential is calculated for each one of these particles ($U_{tj} = \sum_{i=1, i\neq j}^{N} U_{ij}(t)$) and at each time step we add up the expression $\mu_k = \sum_{j=1}^{N_t} \exp\left(-\frac{U_{tj}}{T}\right)$ and at the end we calculate the time average and obtain

$$\mu_{res} = -T \ln \left(\frac{1}{M} \sum_{k=1}^{M} \mu_k \right) . \tag{1.80}$$

The higher the number of test particles used for the insertion, the better will be the statistics of the result [16].

1.6.7 Evaluation of homogeneous nucleation rate

In order for a grain to be nucleated, an unstable liquid cluster must be transformed into a solid nucleus [5, 8, 12], and this transformation requires a minimum release of internal energy in order to decrease the thermal agitations in a way that interatomic forces may stabilize the liquid cluster and lead to the formation of a solid nucleus. Therefore, it would be reasonable to expect that the nucleation rate is dependent on the variation of the residual chemical potential during the phase transition. The nucleation rate is given by [5]

$$I_v = 10^{33} \exp\left[\frac{-4\eta_s^3 \gamma^3}{27 k_B T \Delta\mu^2}\right] , \tag{1.81}$$

where η_s is the *shape factor* and γ is the surface tension. This formula provides the number of grains formed per second and per cubic centimetre for a given temperature and a specific differential residual chemical potential, eqn. (1.79). The value of the differential residual chemical potential is calculated via the test-particle method, described in section (1.6.6).

1.6.8 Isometric and isobaric specific heats

Based on the generalised Einstein and Green-Kubo formula [16], for a given property $A(t)$, the autocorrelation function can be defined as

$$\lim_{t\to\infty} \left\langle [A(t) - A(0)]^2 \right\rangle / 2t = \int_0^\infty d\tau \left\langle \ddot{A}(\tau)\ddot{A}(0) \right\rangle . \tag{1.82}$$

The autocorrelation, or covariance fluctuation functions [13, 16], can be used to obtain several thermodynamical properties, such as the isometric and isobaric specific heats. If we consider the total enthalpy H and the temperature T, we can define the isometric specific heat as

$$< \delta H^2 >_{NVT} = k_B T^2 C_v \, , \tag{1.83}$$

where

$$< \delta H^2 > = < H^2 > - < H >^2 \, . \tag{1.84}$$

H represents the Hamiltonian, i.e. the total energy. All the running mean square deviations are calculated, in our case, in the canonical ensemble. The isobaric specific heat is given by

$$C_p = \left[K_t T \gamma_v^2 \right] V + C_v \, , \tag{1.85}$$

where K_t is the isothermal compressibility, γ_v is the thermal pressure coefficient and V is the volume of the system. Both of these values represent the variation in the total energy of the system due to a variation in the temperature of the same system.

1.6.9 Isothermal and isoentropic compressibility

The isothermal compressibility measures how the system's volume responds to an isothermal pressure variation. It is defined as [13, 16]

$$K_t^{-1} = \left[\frac{-1}{V} \left(\frac{\partial V}{\partial P} \right)_T \right]^{-1} , \tag{1.86}$$

where V is the volume and P the pressure of the system. In the canonical ensemble, the isothermal compressibility can be obtained using [16, 36]

$$K_t = \left[\frac{2P + \rho k_B T}{3} + < \Theta > - \frac{N < \delta P^2 >}{\rho k_B T}\right]^{-1}, \tag{1.87}$$

where ρ is the density of the system and Θ is related to the *force constant* and is given by

$$\Theta = \frac{1}{9V} \sum_{i=1}^{N-1} \sum_{j>i}^{N} r_{ij}^2 \frac{\partial^2 U_k(r_{ij})}{\partial r_{ij}^2}, \tag{1.88}$$

in which r_{ij} is the atomic distance between atoms i and j and U_k is the interatomic potential calculated at time step index k. The value of isoentropic compressibility can be obtained using the isometric and isobaric specific heats [16]

$$K_s = \frac{K_t C_v}{C_P}. \tag{1.89}$$

In the case of isoentropic compressibility, the volume change of the system is in response to a reversible and adiabatic change of pressure in contrast to an isothermal change of pressure [16]. The isoentropic compressibility can be used to evaluate the velocity of sound within the material, ω, via

$$\omega = \sqrt{\frac{1}{\rho K_s m}}, \tag{1.90}$$

1.6.10 Thermal pressure coefficient

The thermal pressure coefficient measures the variation in pressure due to an isometric change of temperature. It can be obtained in canonical ensemble using the expression [16]

$$\gamma_v = (1/V)\left[\frac{< \delta U \delta W >}{K_b T^2} + N k_B\right], \tag{1.91}$$

where δU represents the variation of interatomic potential and δW represents the variation of the virial pressure of the system.

1.6.11 Shear viscosity, shear and bulk moduli

Shear viscosity is due to the velocity gradient which exists between parallel flux within a system [16, 37]. In the case of a molecular system, the way by which one particle's momentum is transported by the other particles in different directions is measured by the value of the system's shear viscosity [16, 38] . Shear and bulk moduli are, on the other hand, two parameters which represent the elastic behaviour of a system with regard to a sudden applied force [16]. Quantitatively, the bulk modulus is equivalent to the inverse of isothermal compressibility [16, 37] and shear modulus, also called the coefficient of rigidity, is equal to the static value of the shear viscosity.

The evaluation of the shear viscosity is based on the determination of the *stress tensor* whose elements are given by [16]

$$S_{\alpha\beta} = m\sum_{i=1}^{N} v_{i\alpha}v_{i\beta} + \frac{1}{2}\sum_{i\neq j}^{N} r_{ij\beta}F_{ij\alpha} \tag{1.92}$$

where α and β are (x,y,z). In this expression $v_{i\alpha}$ is the α component of the velocity of atom i and $r_{ij\alpha}$ is the α component of the interatomic distance r_{ij}. The β component of the force applied on atom i by atom j is represented by $F_{ij\beta}$. If the system is homogeneous and isotropic, then the tensor will be symmetric [16]. Based on the virial theorem [13], the time-average of the sum of the diagonal elements (the trace) will provide us with the total pressure (kinetic and virial parts) of the system [16]. The shear viscosity is given by the *stress autocorrelation function* formed from the off-diagonal elements of the stress tensor. By choosing A as $m\sum_{i=1}^{N} v_{i\alpha}(t)r_{i\alpha}(t)$ in (1.82) we have [16]

$$\eta = \frac{1}{Vk_BT}\sum_{\alpha}\sum_{t_0}\frac{1}{2}\left[m\sum_{i=1}^{N} v_{i\alpha}(t)r_{i\alpha}(t) - m\sum_{i=1}^{N} v_{i\alpha}(t_0)r_{i\alpha}(t_0)\right]^2 , \tag{1.93}$$

where t_0 is the time origin and we sum over various time origins. The value of shear modulus, as mentioned before, is the static value (at origin) of the shear viscosity, and therefore we have [16]

$$S_m = \lim_{\tau\to 0}\left\langle \ddot{A}(\tau)\ddot{A}(0)\right\rangle \tag{1.94}$$

where

$$\ddot{A}(\tau) = m \sum_{i=1}^{N} \sum_{\alpha} \sum_{\beta} v_{i\alpha}(t) v_{i\beta}(t) + \sum_{i=1}^{N-1} \sum_{j>i}^{N} \sum_{\alpha} \sum_{\beta} r_{ij\beta}(t) F_{ij\alpha}(t) \tag{1.95}$$

The summation is over the cyclic indices xy, yz and zx in order to increase the accuracy of the final result.

1.6.12 Diffusion coefficient

Green-Kubo formula allows us to relate a macroscopic transport coefficient to some molecular quantities [13, 16] which in the case of the diffusion coefficient is the *molecular positions.* The diffusion coefficient which is a measure of molecular diffusion due to stochastically distributed elastic collisions, is given by the expression [13, 16] :

$$D = \lim_{t \to \infty} \frac{\left\langle [r_i(t) - r_i(0)]^2 \right\rangle}{6t} \tag{1.96}$$

This expression must be calculated for every particle in the system and the results must be averaged to increase the accuracy [13, 16].

1.7 Results and discussion

1.7.1 Introduction

It was indicated in Figure 1 that MD simulations are performed as a computational tool to provide the values of the following parameters needed in the micro and macro scales modelling:

- The values of the diffusion coefficient and the nucleation rate are needed for the micro level simulations that are performed in Chapter 2.
- The values of thermo-mechanical properties, such as the specific heat, latent heat and shear viscosity are needed for the macro level simulations that are performed in Chapter 3.

The question that must be asked before using MD-based results, as input to micro- and macro- scale simulations, is how accurate and reliable these results are, and also how effective the phase transition is modelled by MD simulations. The accuracy of results produced by an MD simulation and the effectiveness of the phase transitions modelled, depend strongly on the accuracy of the interatomic potential used [22]. In order to investigate the suitability of interatomic potentials used, several MD simulations were conducted to study the phase transitions of elemental and binary metallic systems. In this Section, a description of the implementations of these simulations and the results related to the detection of phase transitions via the calculation of the radial distribution functions and translational order parameters are given. Also the evaluation of thermo-mechanical properties, over a range of temperatures, such as the isobaric and isometric specific heats and shear and bulk moduli for several elemental and binary materials are provided.

1.7.2 Implementations of MD simulations

Simulations involving Al, Cu, Pb, Ag-Cu, Sn-Pb and Al-Sn nano-sized clusters of atoms were performed. For different systems, the total number of atoms in these clusters varied within the range of 490 to 7040 as follows:

- 490 atoms for Al and Pb clusters for the study of the shear and bulk moduli, isothermal and isoentropic compressibility, latent heat of fusion and thermal pressure coefficient.
- 490 atoms for the Al and Cu clusters for monitoring the emergence of the phase transition.
- 7040 atoms for the Al cluster in order to calculate the c_p and c_v
- 4805 atoms for Ag-5%wtCu and Ag-10%wtCu binary clusters for the evaluation of the diffusion coefficient and nucleation rate.
- 544 atoms for Sn-10%wtPb cluster for the evaluation of the diffusion coefficient and nucleation rate.

- 490 atoms for Al and Al-3%atSn binary clusters for the evaluation of the diffusion coefficient and nucleation rate.

The simulation's time step was set at $\delta t = 2$fs. The time step must be chosen carefully in order to allow the temperature bath to relax the system thermally. Therefore the time step is chosen about an order of magnitude less than the relaxation time used in the Nos'-Hoover dynamics. The initial temperature was set at $10K$ and was raised to 2010K for the Al, Pb and Ag-Cu clusters, to 3010K for the Cu cluster and to 1540K for the Sn-Pb and Al-Sn clusters, well above their respective liquidus temperatures. All the clusters were initially constructed in their respective crystalline states. The liquid states were then obtained, and equilibrated for 10,000 time steps using the Nosé-Hoover thermostat formalism for the temperature control, eqns. (1.45), (1.46) and (1.47). Following equilibration, the system was cooled down at the rate of $1K$ per 100 time steps until it reached the room temperature. During cooling, the system was periodically re-equilibrated at several intermediate temperatures. The PBC was applied and a cut-off, equal to 2 lattice parameters in the case of SC and RTS potentials and equal to the atomic diameter in the case of MM potential was applied.

1.7.3 Mixing rule for Sn-based alloy potentials

The case of Sn-based alloys, for which a new mixing rule for the MM potential was developed, were complicated due to their allotropic transformations at 13.6°C from an α-diamond structure to a β-tetragonal body-centerd structure.

The Murrell-Muttrom potential, as described in Section (1.4.6.4), was used in order to study the properties of Sn-based alloys, in our case the Sn-Pb alloy. *The Sn-Pb binary alloy was chosen due to its extensive use as the soldering material in the electronic packaging industry.* Six different mixing rules based on arithmetic and geometric averages were used as described in Section 1.4.7.2. These rules were applied to Sn-50%wtPb at 773K for the calculation of the enthalpy of formation, ΔH_{Sn-Pb}. The enthalpy of formation was used to find the best fit for the alloy potential.Table 1.1 shows that the result obtained with rule number 5 was in a reasonable agreement with the experimental result [42].

Table 1.1

mixing rule	ΔH^{773K}_{Sn-Pb} (cal/gr)	error to expt.
1	514	171%
2	290	3.34%
3	218	4.0%
4	243	19.0%
5	299	0.33%
Experiment		300

In order to investigate further the validity of the mixing rule, the rule number 5 was applied to several alloys with different Sn and Pb concentrations. The results obtained for varying Sn concentrations are shown in Figure 1.4. It can be seen from this Figures that the simulated

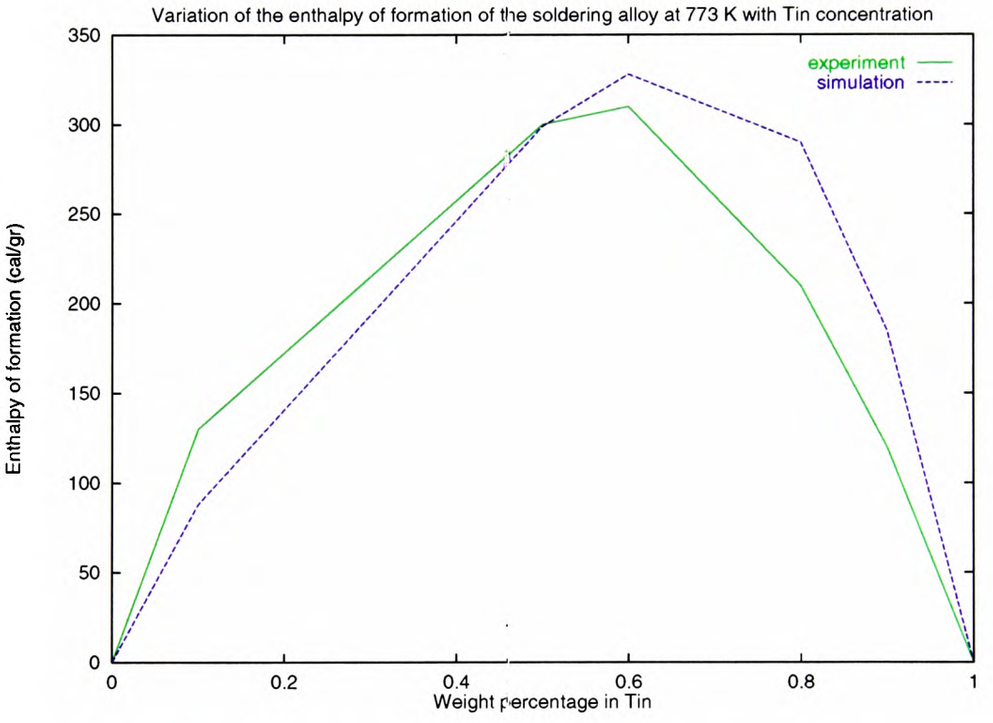

Figure 1.4: Simulated and experimental enthaply of formation of Sn-Pb alloy using the mixing rule number 5

value is under-estimated for Sn concentrations smaller than 50%wt and is over-estimated for Sn concentrations higher than 50%wt. In order to find out how accurate this alloy potential is

for the evaluation of the thermo-mechanical properties, the isometric heat capacity and also the shear viscosity were calculated using eqns. (1.83) and (1.93) respectively for the alloy compositions for which experimental results were available. It can be seen from Table 1.2 that the simulated values of the cohesive energy and the isometric heat capacity are in good agreement with experimental values. This suggests that the fitted alloy potential, obtained using the enthalpy of formation, can reasonably model the interaction of particles within the binary cluster. As the MD simulations are used to calculate the nucleation rate, I_v eqn. (2.2), based on the computation of the residual chemical potential, eqn. (1.79), therefore having a potential which models accurately the particle interactions is very helpful. Hence the MM potential can be used to evaluate the residual chemical potential and therefore the nucleation rate. The value of the isometric heat capacity can also be used as an input for the macro level simulation (see Chapter 3) as the difference between the experimental and simulated values are in a range of 2 to 3 percent.

Table 1.2

Material	Temperature K	Property	Experiment	Simulated
Sn-50%wtPb	298	C_v	210 J/KgK ([43])	205 J/KgK
Sn-50%wtPb	775	C_v		251 J/KgK
Sn pure	298	C_v	226 J/KgK ([43])	230 J/KgK
Sn-50%wtPb	625	η	0.02 Kg/sm ([43])	0.05 Kg/sm
Sn pure	10	cohesive energy	3.12 ev	3.09 ev
Pb pure	10	cohesive energy	2.04 ev	1.92 ev

Despite the fact that the MM potential is not based on the thight binding theory [44], its behaviour regarding the surface reconstruction, resembles interatomic potentials, which are based on the second moment approximation of the thight binding theory [44] in an effective-medium. It has the advantage of reproducing accurately the lattice energy but has the disadvantage of not reproducing the lattice structures accurately, especially lattice surfaces. In order to illustrate this fact a cluster of 1000 Sn atoms within a diamond structure at 0K was constructed. The cluster was equilibriated for 10000 time steps at 0K and then heated up to

273K within 20000 time steps. The cluster was then re-equilibriated for 10000 time steps at 273K. The lattice structure corresponding to this temperature is shown in Figure 1.5. It can be seen that far below the surface, the lattice structure is preserved and the diamond structure is in place but near the surface the lattice is deformed and distorded. Therefore, in order to

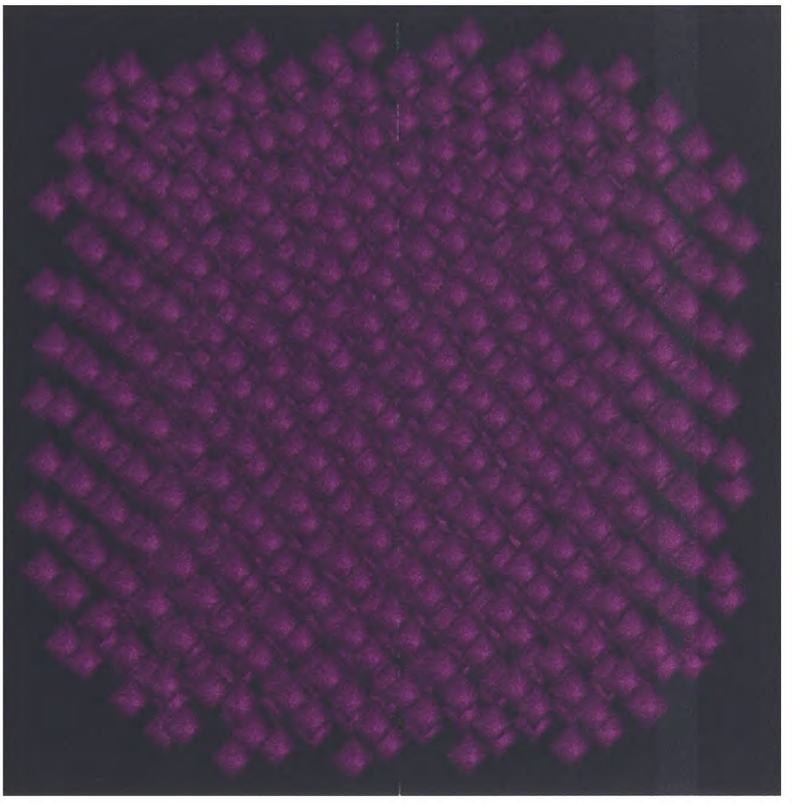

Figure 1.5: The Sn diamond structure at equilibrium, at 273K

obtain precise thermo-mechanical properties we need to increase the number of bulk particles in comparison to the surface particles.

1.7.4 Detecting the phase transition

In this Section the validity of MD simulations for the study of phase transitions has been investigated using the evaluation of the RDF, eqn. (1.69), and translational order parameter, eqn. (1.70), of Al and Cu clusters. As for any crystalline structure, at tempeartures far from the melting point, the local atomic density is anisotropic and has a Dirac δ-function-

like distribution. At higher temperatures, due to thermal agitations, the Dirac δ-function transforms into a Gaussians distribution and by reaching the melting point the local atomic density spectrum becomes continuous [16]. A cluster of 490 Al atoms within an FCC structure was constructed. The RTS potential was used to equilibriate the cluster during 10000 time steps at $0K$. The RDF was calculated for the equilibrium cluster at $0K$ using eqn. (1.69) as shown in Figure 1.6. A set of Dirac δ-functions representing different localised atomic densities can be observed. As the system was not disturbed by the thermal agitations, the value of RDF was discretised due to the relative position of atomic pairs within the crystal structure. The highest frequency was observed for the pairs of atoms representing the nearest neighbours in the FCC structure at a distance of one atomic diameter which is around 0.71 times the lattice parameter. Now, for the same cluster of 490 Al atoms, we began to heat up the system

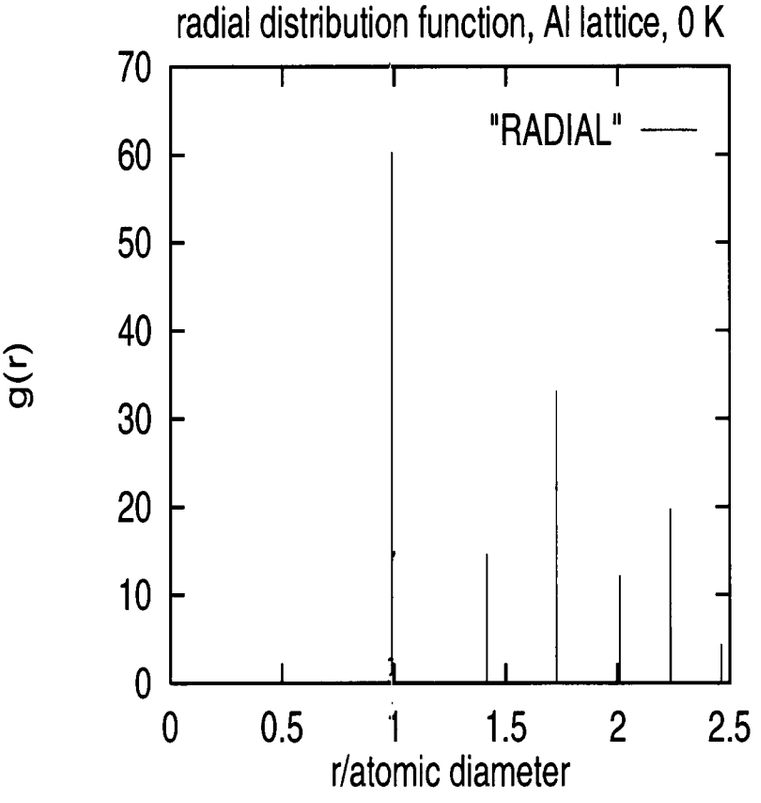

Figure 1.6: Radial Distribution Function at 0 Kelvin for Al

at the rate of 2010 K within 20000 time steps, melting down the crystal structure. Due to the increased thermal agitation at this high temperature, atoms moved from their initial

positions and the relative distances of atomic pairs within the heated system were no longer confined to thier original values as it was the case at $0K$. Therefore, the spectrum of allowed relative positions become more continuous and, the total density of atomic pairs observed at a given position decreased. This means that the original set of Dirac δ-functions were now transforming into a nearly continuous spectrum. This was shown by the value of the running RDF (the term running corresponds to the fact that the RDF was calculated at each time step for varying temperatures) in Figure 1.7(a). After reaching the temperature of $2010K$, the system was re-equilibriated for 20000 time steps and the value of RDF is calculated at this temperature as shown in Figure 1.7(c). By comparing Figures 1.7(c) and 1.6 we can observe the complete transformation of the RDF for a solid phase to the one corresponding to the completely liquid phase. At these temperatures above the melting point, the crystal structure was completely gone and the spectrum was completely continuous and had only one peak left as shown in Figures 1.7(a), representing the greater number of minimum distance atomic pairs due to short range ordering in liquid systems [16] with the peak at one atomic diameter. By re-solidifying again the liquid system and decreasing the temperature from $2010K$ to $10K$ within 20000 time steps, rearrangement of atoms into a crystalline structure, began to bring back the Dirac δ-function-like distribution as shown in Figure 1.7(b) representing the running RDF within the temperature range of 2010 to 10K. Once the system reached the 10K, it was re-equilibriated for 10000 time steps and the RDF calculated at this temperature is shown in Figure 1.7(d). The spectrum was once more nearly discretised with some interferences due to residual thermal agitation at 10K and the lattice reconstruction inperfections due to MD simulations observable also in Figure 1.8. The change in the order of an atomic cluster, was a manifestation of the structural change. For an interatomic potential to simulate the phase transition accurately, the correct reconstruction of the crystalline structure is an advantage. The change in the lattice structure was monitored during the melting and the solidification of the 490 Al atoms cluster and is shown in Figure 1.8. In Figure 1.8(a) the atomic cluster is liquid and no crystallographic plane is observable. Figures 1.8(b) and (c), represent the reconstruction of the crystallographic planes whithin the FCC structure before and after the equilibrium respectively. The most important aspect of the phase change in this Thesis is the

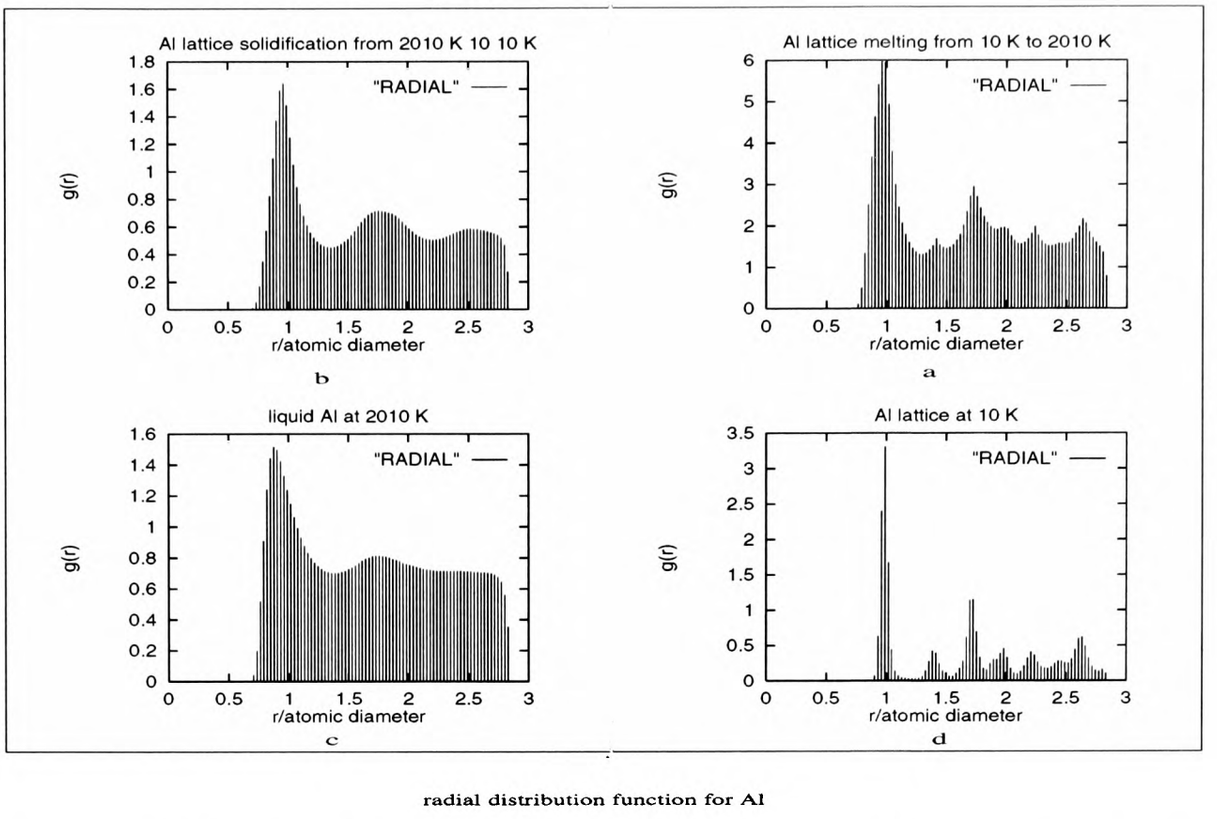

Figure 1.7: Variation of the Radial Distribution Function with temperature for Al

quantification of the change in the internal energy of the system due to the relation between the variation of the Gibbs Free energy or the residual chemical potential and important material properties such as the specific heat, viscosity, nucleation rate or diffusion coefficient. The release of the latent heat or enthalpy of fusion, ΔH, during the solidification, levels down the internal energy of the system and therefore the value of Gibbs free energy is lower in the solid phase in comparison to the liquid phase. This difference between the values of the Gibbs free energy is the driving force behind the liquid-to-solid phase transition as shown in Figure 1.1. For the same Al cluster, the variation of the Gibbs free enrgy during the melting and the solidification was monitored as shown in Figure 1.9. During the melting process, the values of both interatomic potential and Gibbs free energy increased as shown in Figure 1.9(a). To make sure that the system reached equilibrium, the potential and Gibbs free energy were monitored and appeared to be constant in Figure 1.9(c). During the solidification, in opposition to the melting, a discontinuity was observed at the melting point due to the release of the latent heat

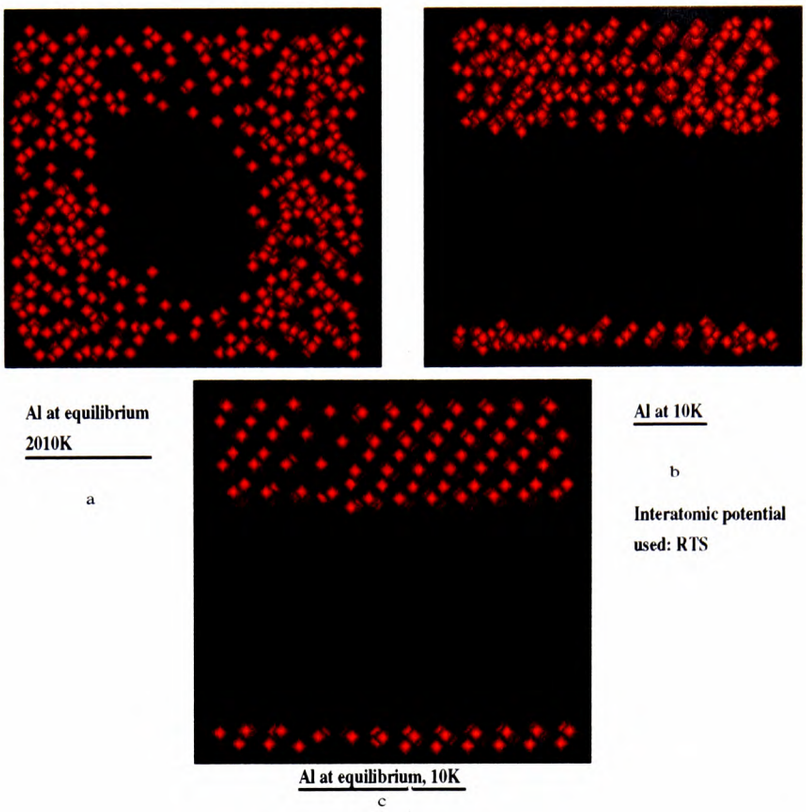

Figure 1.8: The reconstruction of the Al crystallographic structure after solidification

which characterises the driving force for the phase change as shown in Figure 1.9(b). The value of the potential and Gibbs free energy was monitored once more at equilibrium at $10K$ and they also appeared to be constant but much smaller than those at $2010K$. This is shown in Figure 1.9(d).

In order to test further the interatomic potential, the same process was applied to copper. To see if the elevelation of temperature high above the melting point has any influence on the behavior of the potential (it must be kept in mind that interatomic potentials are idealy created for zero Kelvin), a cluster of 490 Cu atoms was considered and equilibriated at 10K during 10000 time steps. The Cu cluster was then heated up from 10K to 3010K during 30000 time steps The system was then equilibriated at 3010K for 10000 time steps. The variation of the RDF during the melting and at the liquid phase was similar to the aluminum and is shown in Figures 1.10(a) and 1.10(b) respectively. By resolidifying the cluster from 3010K to 10K during 30000 time steps and after the re-equilibrium at 10K during 10000 time steps,

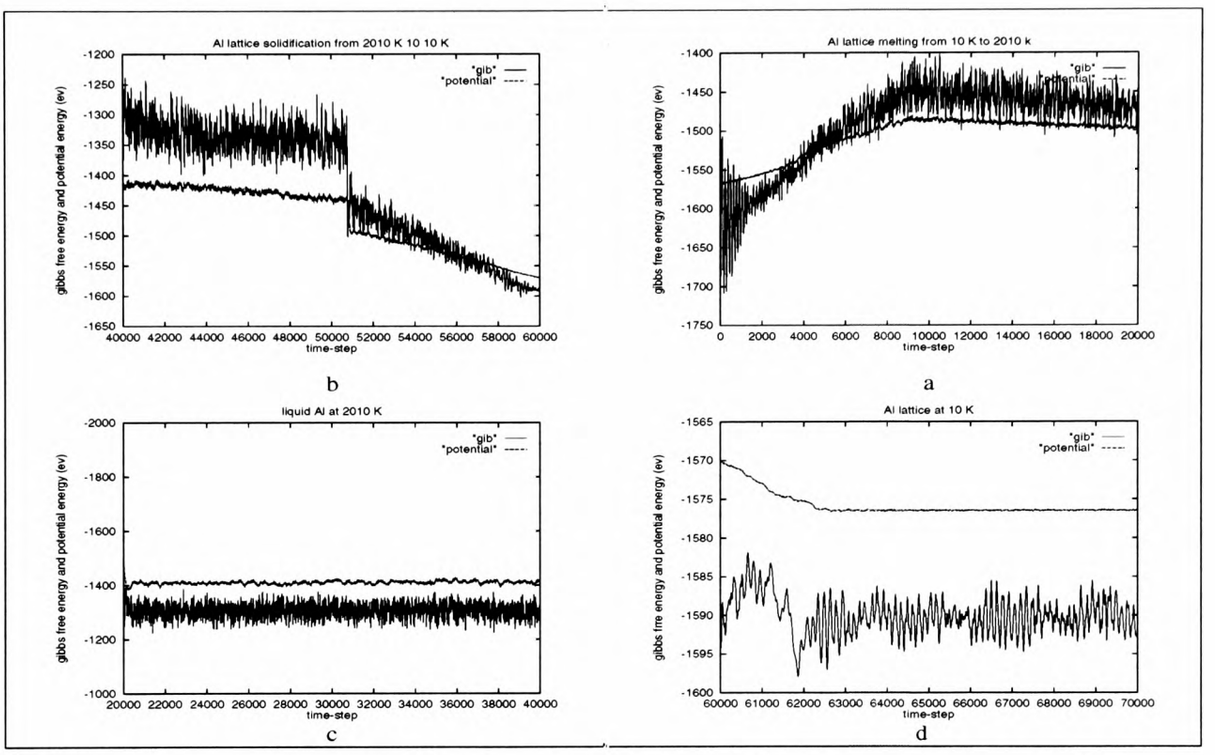

gibbs free energy and interatomic potential for Al

Figure 1.9: Variation of Gibbs free energy with temperature for Al

the reconstruction of the lattice can be observed via RDF as shown in Figures 1.10(c) and 1.10(d). As in the case of the aluminum the reconstruction of the crystallographic planes due to the transition between the liquid and the solid phases can be observed in Figures 1.11(a-c). By comparing Figures 1.8(c) and 1.11(c), it can be seen that the lattice reconstruction was somehow more accurate in the case of the copper than aluminum. This fact show the relative applicability of the same potential to different materials with the same crystalline structure.

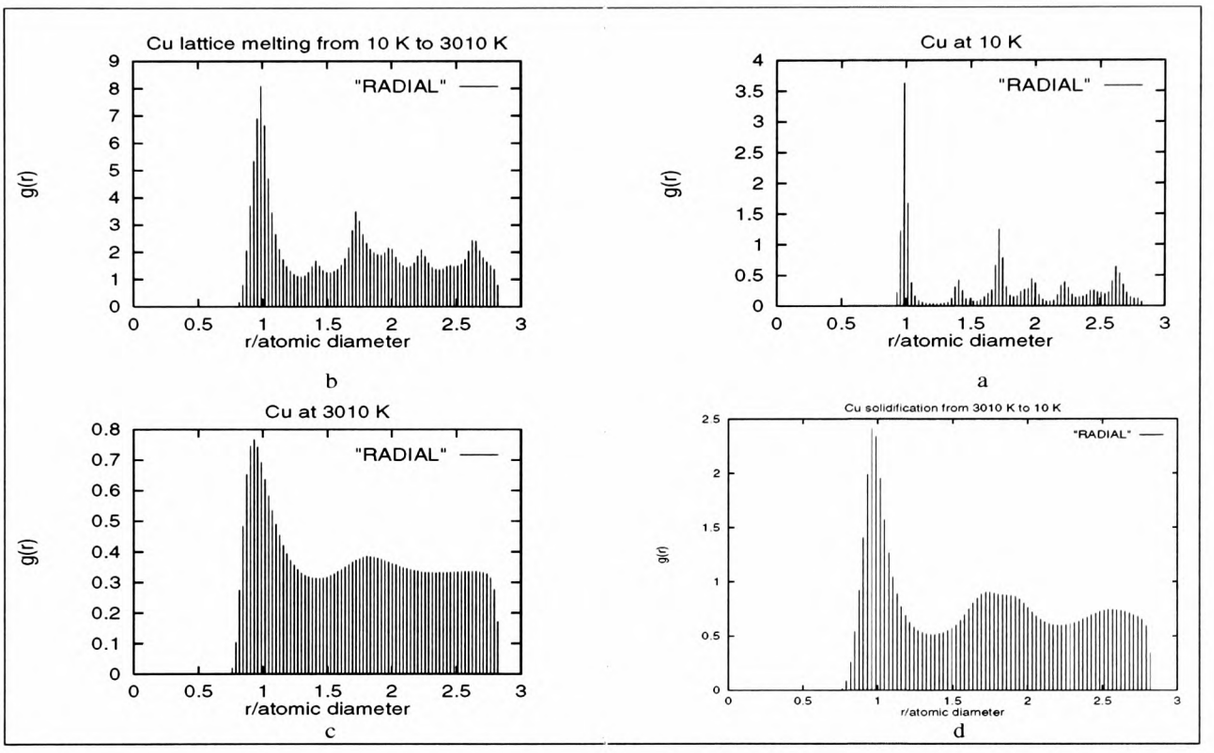

radial distribution function for Cu

Figure 1.10: Variation of the Radial Disdtribution Function with temperature for Cu

The change of the internal energy of the sytem was also monitored to reflect the decrease of the Gibbs free energy due to the liquid-to-solid phase transition. The release of the latent heat of solidification and the change in the value of the Gibbs free energy during is shown in Figure 1.12. As expected, as in the case of aluminum, the level of internal energy of the system was lowered due to the phase change. These two test cases of Al and Cu, show quite accurately, that three main aspects of the liquid-to-solid phase transition are correctly simulated and

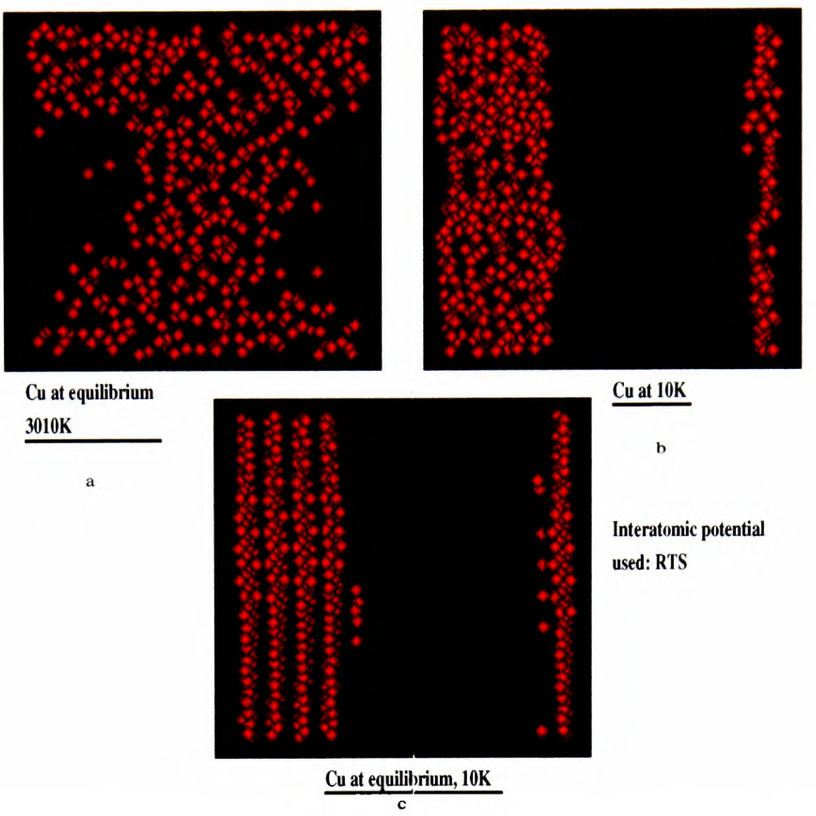

Figure 1.11: The reconstruction of the Cu crystallographic structure after solidification

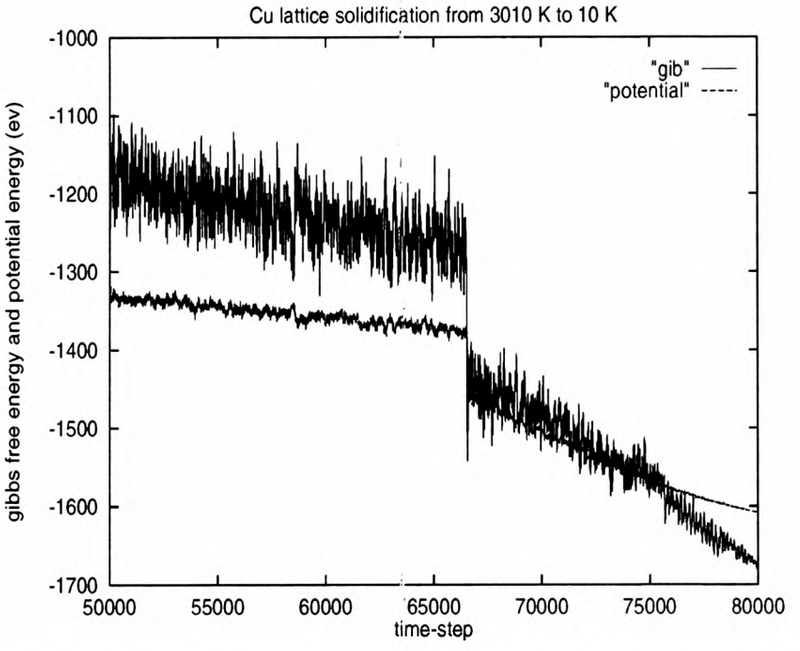

Figure 1.12: Variation of Gibbs free energy with temperature for Cu

modelled by the use of molecular dynamics techniques

- The change in the order of the system was correctly monitored via the calculation of the RDF and the translational order parameter.
- The re-construction of the crystallographic planes could be observed at the end of the solidification and for an equilibrium state.
- The release of the latent heat, or the enthalpy of fusion, could be measured and the transition point detected quite clearly.

Hence, it can be concluded from the above that the use of MD simulations for the detection and monitoring of the phase transition is quite appropriate and, therefore, the evaluation of the material properties during the phase transtion can be done using MD. In the following, MD simulations applied to elemental and binary metallic clusters are reported, and a set of temperature-dependent material properties obtained for future use in the macroscale and microscale models as shown in Figure 1.

1.7.5 Thermo-mechanical properties

In this Section, we report on the results of simulations to compute:

- Shear viscosity (to be used in the macroscale modelling)
- Bulk modulus (evaluation of hardness)
- Isothermal compressibility (material property database)
- Latent heat of fusion (to be used in the macroscale modelling)
- Specific heat (to be used in the macroscale)
- Number density (monitoring the phase change)

These properties were chosen as their knowledge was necessary either to the macroscale simulation of the heat and mass flow (see Chapter 3) during the solidification of, or to the creation

of databases for mechanical properties difficult to measure or evaluate. As their values change with the changing temperature , a temperature-dependent database is necessary. The lack of experimental values for thermo-mechanical properties such as those mentioned above, in the mushy zone (where the liquid and solid phases coexist) and also the difficulty to obtain experimental values in general are the two main reasons for the use of the atomistic modelling in order to produce material property databases necessary to the macroscale simulations of the phase transition as described in Chapter 3. The validation of simulated results is based on the comparison of these values with the values provided by NIST (National Institute of Standars and Technology in USA) or NPL (National Physical Laboratory in UK). Experimental values are mainly produced for the ambient temperature in opposition to the simulated values which vary with temperature. It is assumed that if the simulated values and experimental values are in good agreement for a given temperature for which the experimental measurement is available, since the system behaves deterministically, the other simulated values are also reliable. Al and Pb systems were used to test the accuracy of MD simulations for the evaluation of these properties. In the Table 1.3, the computed values of the residual chemical potentials for different temperatures using eqn. (1.79) are given. These values are necessary for the calculation of the nucleation rate as given in eqn. (2.2) to be used in the microscale simulations as shown in Figure 1. Their values increase with an increasing temperature as shown in the Table 1.3. The enthalpy of fusion, ΔH for the Pb and Al are calculated and compared to experimental values. The agreement between these two values are in the range of 5 to 19 percents error for the Al and Pb respectively. The value of the enthalpy of fusion (latent heat) is necessary to the evaluation of the source term in the enthalpy equation (see Chapter 3). Values of the number density are also given for which a decrease in their value for an increasing temperature is observed. Number density as in the case of RDF, was used to monitor the phase change and is much simpler to calculate. Therefore, it can be used instead of the RDF once the reliability of the potential was established.

Table 1.3

For Pb

T (K)	μ_{res} (ev)	density (1/A3)	$\Delta H^{MD}_{601.5°-600.5°}$	ΔH^{exp}_{sl} (Kcal/Mol)
410	-1.2734	0.6435	1.41	1.14
510	-1.236	0.5985		
598	-1.217	0.5856		
604	-1.214	0.585		
610	-1.214	0.585		
810	-1.20	0.559		

For Al

T (K)	μ_{res} (ev)	density (1/A3)	$\Delta H^{MD}_{930°-937°}$	ΔH^{exp}_{sl} (Kcal/Mol)
310	-1.9714	1.219	2.68	2.55
510	-1.933	1.168		
710	-1.904	1.127		
910	-1.878	1.0904		
930	-1.877	1.087		
940	-1.875	1.085		
1010	-1.867	1.0721		
1510	-1.814	0.9896		

In Table 1.4, the simulated and experimental values of the shear viscosity, bulk and shear moduli and isothermal compressibility for the Al and Pb systems are compared. The simulated shear viscosity, shear modulus, isothermal compressibility and bulk modulus were obtained using eqns. (1.93), (1.94) and (1.87) respectively. Except for the shear modulus in the case of the Al system, simulated values are in good agreement with the experimental values. As shown in Figures 1.13 and 1.14, the value of shear viscosity decreases with the temperature as the force necessary to move one layer of material over another one with a different velocity decreases with an increasing temperature due to the increasing thermal agitation and therefore, interatomic bonding, weakening.

Table 1.4

Material	TK	Property	Experiment	Simulated
Al	973	viscosity	0.0011 Kg/sm	0.00144 Kg/sm
Pb	300	viscosity	0.0015 Kg/sm	0.00153 Kg/sm
Al	300	bulk modulus	70 GPa	50.8 GPa
Pb	300	bulk modulus	45 GPa	42.8 GPa
Al	300	shear modulus	26 GPa	9 GPa
Pb	300	shear modulus	5.6 GPa	7.3 GPa
Al	300	isothermal compressibility	0.0143 1/GPa	0.0197 1/GPa
Pb	300	isothermal compressibility	0.025 1/GPa	0.0233 1/GPa

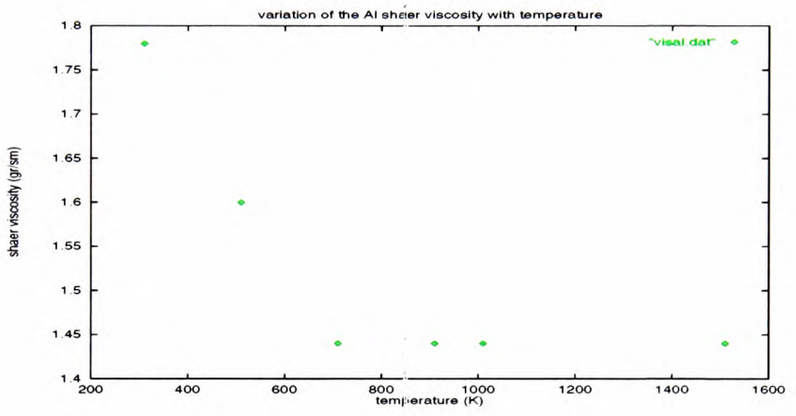

Figure 1.13: Temperature variation of Al shear viscosity

Figure 1.15 gives the variation of simulated and experimental values of the isobaric specific heat. As shown, there is a good agreement between the simulated and experimental values. The simulated values were obtained using eqn. (1.85). The specific heat increases when the temperature increases. These temperature-dependent values of the specific heat or the heat capacity are necessary to the solution of the enthalpy equation described in Chapter 3. Values of isothermal compressibility for Al and Pb systems are given in Figures 1.16 and 1.17 respectively. They were obtained using eqn. (1.87). The isothermal compressibility increases with the temperature as the change in system's volume based on an imposed pressure

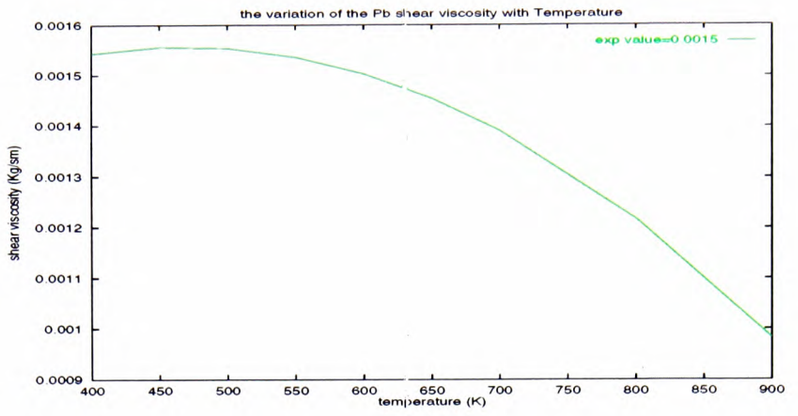

Figure 1.14: Temperature variation of Pb shear viscosity

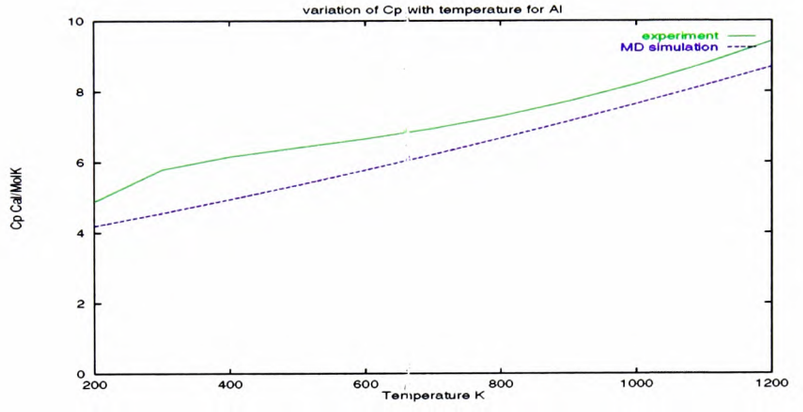

Figure 1.15: Temperature variation of Al specific heat

perturbation increases, when the temperature increases. The temperature-dependent values for the isothermal compressibility are generally not available particularly in the mushy zone.

The values of the bulk and shear moduli are quite important for the determination of mechanical properties, such as the hardness. The shear modulus is also called the rigidity modulus or the rigidity coefficient. The value of the bulk modulus decreases with temperature in opposition to the value of shear modulus which increases with the tempearture as shown in Figures 1.18, 1.19 and 1.20. The former represents the force to be applied to the system and the latter is the deformation of the system, therefore when the temperature goes up the former decreases and the latter increases. Figure 1.21 shows the experimental and simulated

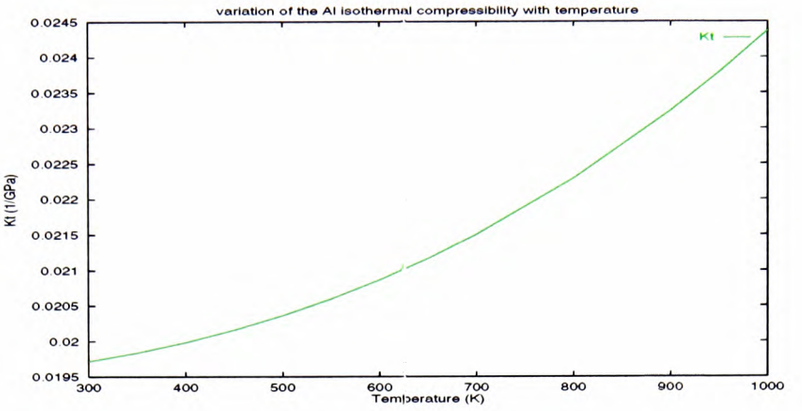

Figure 1.16: Temperature variation of Al isothermal compressibility

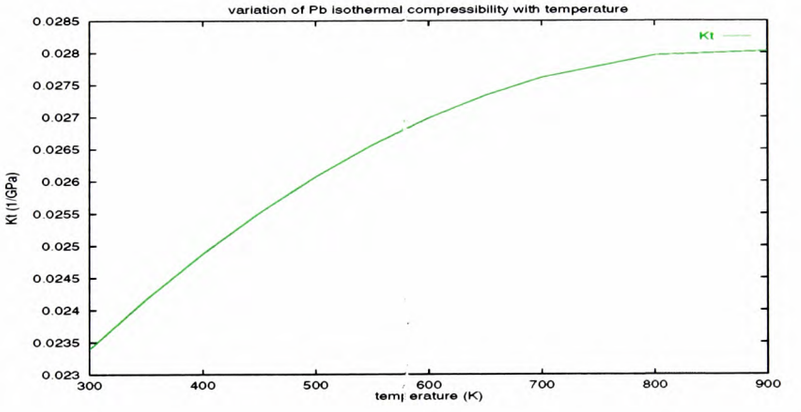

Figure 1.17: Temperature variation of Pb isothermal compressibility

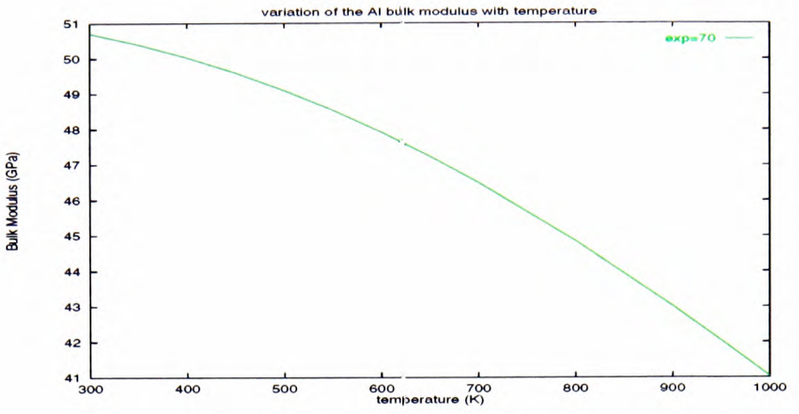

Figure 1.18: Temperature variation of Al Bulk modulus

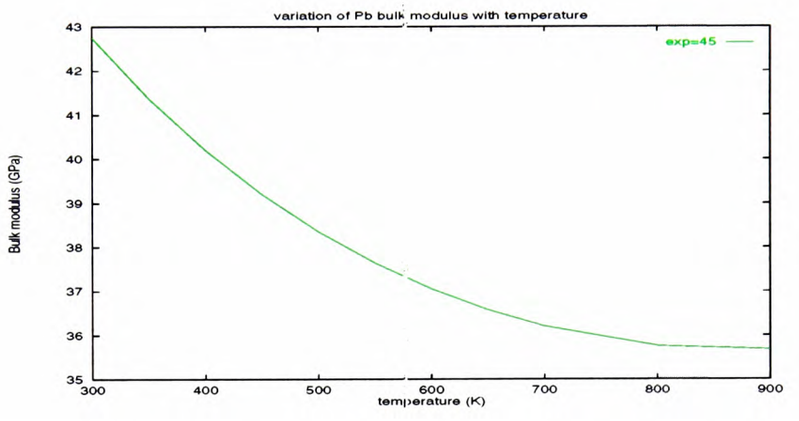

Figure 1.19: Tempearature variation of Pb Bulk modulus

values of the isobaric specific heat for seven different FCC metallic systems (Al, Cu, Pb, Ni, Ag, Au and Pt), all calculated at room temperature. As shown, there is a good agreement between these two sets of values. Also in Figure 1.21, values of the thermal pressure coefficient and isoentropic compressibility obtained respectively by eqn.s. (1.91) and (1.89), are given.

1.8 Concluding Remarks

In this Chapter the fundamentals of Molecular Dynamics simulations based on the use of statistical-mechanical ensembles and prescribed interatomic potentials have been discussed.

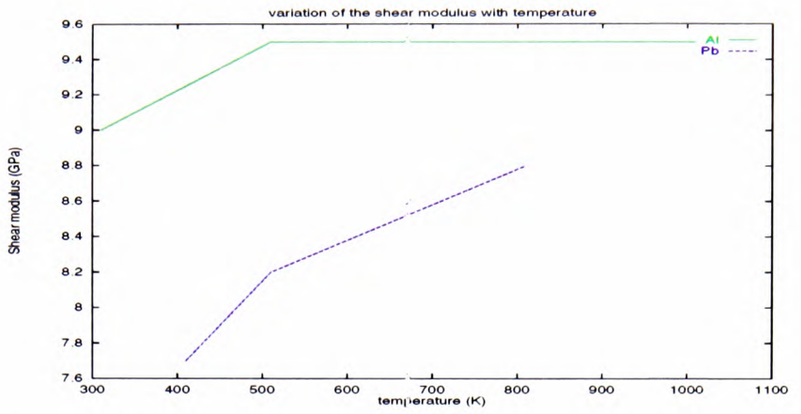

Figure 1.20: Temperature variation of Al and Pb shear modulus

MD simulations were used to compute the input parameters for the micro- and macro- scale simulations, as shown in Figure 1. The main task was to determine the usefulness and the accuracy of MD simulations, in their role as a preprocessor to the upper level simulations, to be described in Chapters 2 and 3. To do so we emphasised two major roles of MD simulations in our multiscale model which are as follows:

- To be able to detect with precision the nanoscopic liquid-to-solid and solid-to-liquid transitions via a continuous control of the degree of the order, Gibbs free energy and crystallographic structure of the system.

- To provide accurate, reliable and reproducable thermo-mechanical properties that vary with the temperature of the system.

As MD simulations are based on the solution of the equations of motion, eqn. (1.9) in which the force is derived from an interatomic potential, eqn. (1.10), the ability of the interatomic potential used to reproduce the physics of the problem is of critical importance. The physics that we model in this Thesis is that of phase transition, therefore three main aspects of the phase change can be monitored in order to evaluate the suitability of the interatomic potentials used in the MD simulations:

- The change in the order of the system,

- The variation in the internal energy of the system, and
- The destruction and reconstruction of the crystallographic structure.

As the system changes its phase from solid to liquid or vice versa, the translational order parameters, eqn. (1.70) and the radial distribution function, eqn. (1.69) change. As shown in Figures 1.7 and 1.10, by increasing the temperature the local atomic density becomes continuous, representing the melt down of the crystallographic structure and by decreasing the temperature, the spectrum becomes discret, representing the reconstruction of crystallographic planes. This reconstruction can be observed in Figures 1.8 and 1.11 for the FCC structures.

The change in the internal energy of the system associated with the phase change is also shown in Figures 1.9 and 1.12. The discontinuity at the melting point of the material is due to the release of the latent heat of fusion. For an alloying material, in addition to the Gibbs free energy one can monitor the enthalpy of formation as shown in Figure 1.4 for Sn-Pb binary alloy, for which the simulated results have less than 10% error.

Based on these simulated results, it can be concluded that the MD simulations, based on the chosen interatomic potentials, do detect accurately the phase change and therefore can reproduce the physical phenomenon of phase transition. As the properties calculated at the nanoscale are mainly related to the positions and velocities of the particles, and therefore, related to their interactions, the values of these properties are directly linked to the quality of the interatomic potential used. We can therefore evaluate some of these properties and monitor their variation during the phase change as an additional criterion to test the interatomic potentials. Comparison between simulated values and experimental values at given temperatures are given in Tables 1.2, 1.3 and 1.4. Based on these Tables, there is an overall agreement between the simulated and experimental results.

Two properties are important to the simulation of the heat and mass transfer as will be described in Chapter 3. The latent heat and the specific heat, for which the variations with the temperature, especially in the mushy zone (where the liquid and solid phase co-exist), are very important, can be calculated by MD with a good accuracy, as shown in Figures 1.15 and 1.21.

The values of the diffusion coefficient (calculated by the eqn. (1.96)) and the nucleation rate (calculated by eqn. (2.2)) are given in Chapter 2. These values are used as input parameters to the micro model described in Chapter 2, as shown in Figure 1. As it can be seen in eqn. (2.2), the residual chemical potential calculated by the MD simulations using the test particle method, eqn. (1.79) is used to evaluate the nucleation rate. Hence the accuracy of the interatomic potential determines the quality of the temperature-dependent nucleation rate which in turn influences the microscale simulation results to be described in Chapter 2. Summing up, based on the results presented in this Chapter, we can conclude that

- MD simulations model accurately the nanoscopic phase transition between the liquid and the solid phase
- They can be used to produce temperature-dependent databases for thermo-mechanical properties, especially values related to the inter-phase, or, mushy zone.

These databases are used as linkages to the micro and macro scale simulations as shown in Figure 1. For each binary alloy with a given composition and a set of solidification parameters, such as the cooling rate, a new set of databases must be produced in order to take into consideration the effects of the macroscopic conditions (see Figure 1).

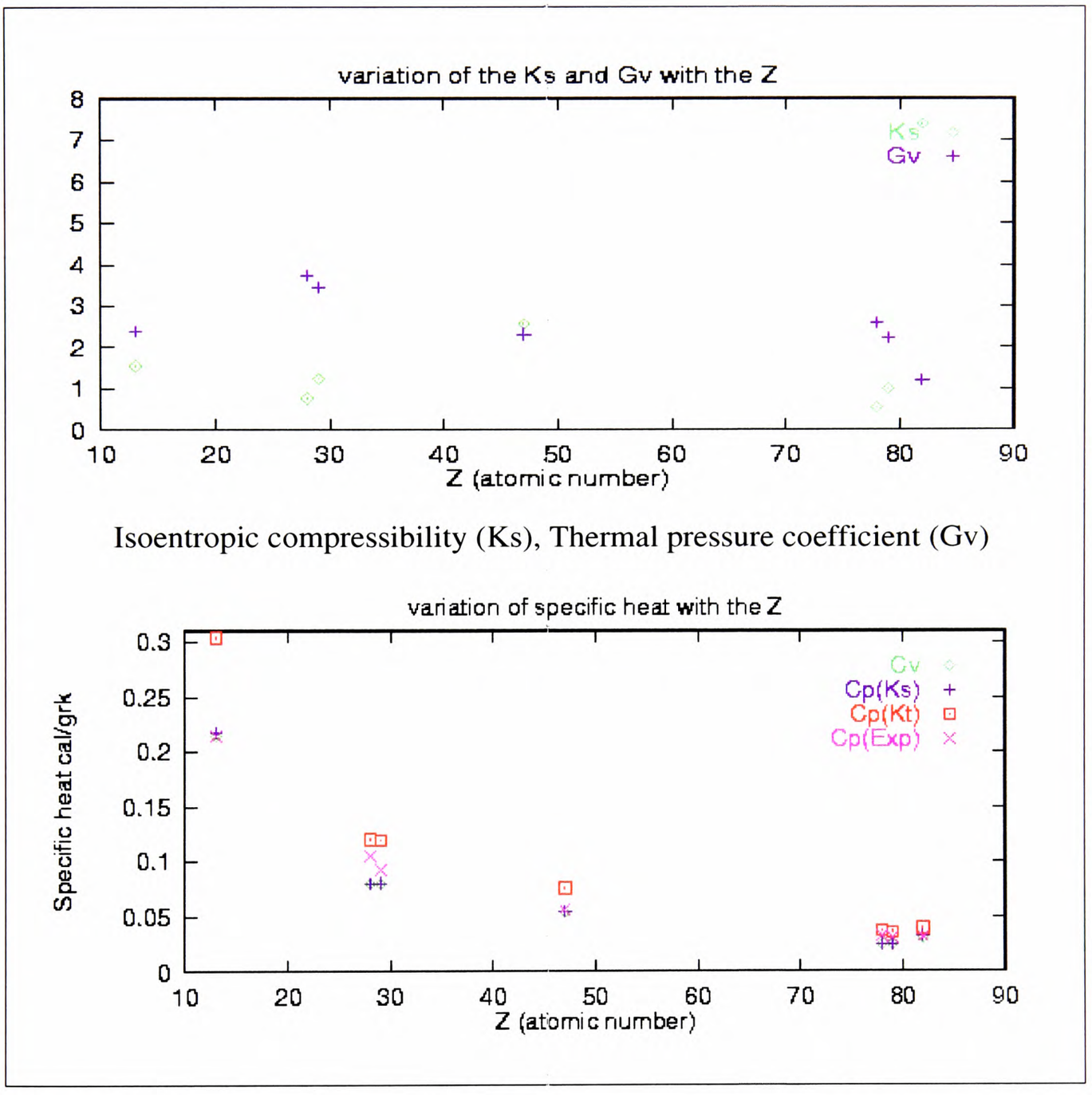

Figure 1.21: Comparison between the simulated and experimental values of specific heat, isoentropic compressibility and thermal pressure coefficient for fcc metallic systems.

Chapter 2

Microscale approach to solidification

2.1 Introduction

The transition of a metallic system from the liquid phase to the solid phase requires a certain amount of undercooling due to the presence of a potential barrier, studied in Chapter 1. The formation of solid nuclei within the undercooled liquid phase and their growth due to heat and mass transfer [12, 8] create a network of interconnected solid regions within the liquid phase that is called a *microstructure* . Due to the coexistance of the residual liquid and the solid regions during the solidification, a third phase which is partially liquid and partially solid can also be identified. This is called the *mushy zone.* The creation and expansion of this zone, based on materials and process parameters, and its influence on the thermo-mechanical properties of the final cast , have been the subject of long-term scientific and industrial investigations. Various models were proposed to predict the final microstructure of solidification in cast alloys. In this Chapter, a new model for the prediction of microstructure developement in binary alloys is proposed. This model (see Figure 1), is based on the results obtained at the atomistic level using MD simulations for the calculation of the nucleation rate and the diffusion coefficient.

The model has been applied to elemental Al, Al-3%atSn alloy, Sn-10%wtPb alloy, Ag-5%wtCu alloy and Ag-10%wtCu alloy for different thermal fields and solidification paths.

2.2 Type of microstructure

Various types of microstructure, depending on the initial composition and solidification path, can be obtained during the solidification. In the case of an elemental metal, single-phase primary crystals having columnar, equiaxed, planar or cellular structures can be observed [12, 8], depending on the process parameters such as, the cooling rate and the casting procedure (die casting, sand-chill, etc). In the case of alloys, both single-phase primary crystals and polyphase structures, can be observed. The polyphase structure can be either a eutectic (two or more solid phases grow simultaneously from the liquid) or peritectic (intersection of two liquid-solid interfaces, forming a three phase equilibrium point) [12, 8]. The existance of these polyphase structures, can create extremely complex textures in comparison to the elemental metals.

Phase diagrams, obtained by first principal calculations of free energy or experimental procedures [45], provide us with the variation of these phases within the alloying system, based on the solutes' concentration and temperature. For binary alloys two main solidification modes can be considered. If the solute concentration is less than the eutectic concentration, then the alloy solidifies in its primary phase with the solute segragating around the grain boundaries due to the last stage of solidification which is a eutectic. The last stage becomes a eutectic because at the end of solidification, due to the continuous rejection of the solute from the solid phase into the liquid, the solute concentration in the remaining liquid becomes a eutectic. If the solute concentration is equal to the eutectic concentration, then the solidification mode will be eutectic from the begining [46], which itself can be fibrous or lamellar, regular or iregular [12, 8].

In this chapter, the case of dendritic microstructure in binary alloys is considered.

2.2.1 Formation of dendritic structures

In order to explain the formation of columnar and equiaxed zones, it is necessary to describe the behaviour of the solid-liquid interface during the solidification. The liquid-solid interface is considered to be planar at the beginning of the solidification. This planar interface can be

perturbed by the convective heat flow or the rejection of the solute from the solid phase in the case of alloys [5, 12, 45]. These perturbations are initially considered to be sinusoidal. If these perturbations find themselves, in front of the interface, in an environment suitable to their growth, they will amplify and grow. In the opposite case, they will either become stable or die out and the interface will stay planar. When the interface becomes unstable, tree-like structures will be created. These tree-like structures are called the dendrites. There are three different kinds of dendritic structure

- The columnar structure, for which the growth direction is imposed by the direction of the heat flow. The growth is anisotropic and the preferential crystallographic growth directions are aligned with the heat flow. This kind of growth is called *constrained growth.*

- The equiaxed structure which itself is divided into two parts

  - The inner-equiaxed formed by an isotropic growth of all possible crystallographic directions with grains nucleating within the liquid bulk due either to the heterogeneous nucleation on impurities or the further growth of broken secondary columnar arms of columnar structures.

  - The outer-equiaxed formed by the further growth of the partially remelted columnar arms due to the formation of a solidification shrinkage air gap near the surface of the mould, or the rapid grain growth on the surface rugosities

  This kind of growth is also called the *unconstrained growth.*

2.2.2 Interface stability and microstructure formation

The creation of the microstructure within an elemental or multicomponent metallic system is closely related to the stability of the liquid-solid interface [47, 48], due to the thermal or fluid flow or even the segregation of inclusions and the creation of grain boundaries [5, 12]. The notion of stability of the interface is based on the relaxation, equilibriation or ampilification of these perturbations. These interfacial variations are considered to be sinusoidal at the

begining [47, 48]. For pure metals, the growth or relaxation of these perturbations is based on the direction of the heat flow. For a columnar structure, as the gradient in front of the interface is positive due to the heat extraction via the mould's walls, perturbations will die out and the interface will be stable. In the case of equiaxed structure, due to a negative temperature gradient in front of the perturbations (the liquid is undercooled), the interface will be unstable [12, 8].

For alloys, as opposed to pure metals, in addition to the temperature gradient and the heat flow, we also have the solute diffusion due to the solute concentration gradient, which creates a solutal diffusion layer at the solid-liquid interface. Therfore, based on the value of the solute concentration at the interface, the value of the liquidus isotherm can vary based on the phase diagram. This means that the change in the interfacial solute concentration can be transformed, via the use of phase diagrams to what is called a *solutal undercooling* which is added to the undercooling due to the thermal effects. Due to the external temperature field, the temperature gradient in the liquid phase can be different from the gradient of the liquidus isotherm at the interface. In case that these two values are identical we call the interface stable at *the limit of constitutional undercooling* for which the columnar structure is stable but the equiaxed structure is unstable [12, 8]. When the value of the temperature gradient becomes greater than the value of the gradient of the liquidus isotherm, the columnar structure will also become unstable, as any perturbation finds itself in an environment which is undercooled and, therefore, increases the growth rate [47, 48, 49].

At high growth velocities, due to the increased capillarity effect which is a consequence of a refined structure (the curvature of the interface is increased), and a decreased diffusion length, limited to the width of the interface, the dominant effect will be the capillarity and therefore, the capillarity length will limit the degree of refinement of the structure. This limited length of the microstructure corresponds to a perturbation wave length called the *limit of marginal stability* of the interface. At these high growth velocities, the solute concentration gradients in front of the peaks and depressions of the perturbation are the same due to the impossibility of the lateral diffusion (diffusion length is smaller than the interdendritic arm spacing) and, therefore, the difference between the peaks and depressions growth rates, which is the main

reason for microstructure formation in alloys , vanishes and the interface becomes stable. The growth rate at which this phenomenon occurs is called the *limit of absolute stability.* Near this limit the dendritic structure transforms into the cellular structure as is the case of the limit of the constitutional undercooling. The difference is in the degree of refinement of cells which is much much higher near the absolute stability [12].

To sumerise we can begin with a planar interface at very low growth velocity, p assing the limit of the constitutional undercooling and the formation of cellular and after that dendritic microstructure for an increasing growth velocity. By reaching high growth rates the structure becomes more and more refined until we reach again the cellular structure and by reaching the limit of absolute stabil ity the interface becomes once more planar or quasi-planar.

2.2.2.1 Differences between the columnar and equiaxed growth

In case of a columnar growth, the growth is directional and the growth direction is determined by the direction of the heat flow. The competition between different preferential crystallographic growth directions of various nucleated grains is based on the best alignment of these preferential directions with the heat flow direction. Therefore, in directional solidification the imposed direction of the heat flow will influence the final grain orientation as the only columnar dendrites to grow are those for which the preferential growth direction is the same as the imposed heat flow orientation [5, 12, 45] .

The case of equiaxed dendrites is different as the growth is isotropic and each grain regardless of its orientation can grow if the growth conditions are satisfied. The origin of equiaxed grains has been the subject of lots of discussions and different theories have been suggested in this area. Three main assumptions are as follows

- The grains are formed on the mould's walls and transported into the bulk by the flow convection [12].
- The grains are the result of mechanical fracture of secondary dendrite arms of the columnar grains or the remelt of some of these arms [45].

- The grains are due to the bulk nucleation for which different nucleation sites have been activated at the same time and compete for the growth based on the local solute concentration [5].

In reality, all these processes take place and the equiaxed region is created by the transported as well as nucleated grains within the bulk.

2.2.2.2 Differences between elemental and alloy systems

In case of a simple metal, as the only factor influencing the growth of a perturbation is the direction of the heat flow [12, 45], a columnar zone can emerge if the temperature gradient in front of the perturbation is positive, as the heat needs to be extracted via the mould's wall. For the equiaxed growth, as the heat will be extracted via the liquid phase, the temperature gradient must be negative in front of the perturbation.

In the case of alloys, the mechanism is much more complex and in addition to the heat flow the following factors must also be taken into consideration

- The effect of the rejection of the solute from the solid to the liquid phase which will affect the local equilibrium liquidus temperature due to a change in local composition at the interface based on the phase diagram [12, 45].
- The effect of the curvature on the local undercooling.
- The effect of the dendrite tip's kinetics and coarsening on the undercooling.

Based on these factors, the total undercooling within an alloying system, ΔT, has several contributions

$$\Delta T = \Delta T_{temp} + \Delta T_{cons} + \Delta T_{curv} + \Delta T_{kin} \,, \tag{2.1}$$

where ΔT_{temp} is the thermal undercooling, ΔT_{cons} is the constitutional undercooling, ΔT_{curv} is the curvature undercooling and the ΔT_{kin} is the kinetics undercooling.

2.2.2.2.1 Curvature Undercooling The curvature undercooling is due to the *Gibbs-Thompson* effect [5, 12] which represents the influence of the interface on the Gibbs free

energy of the system at equilibrium. The surface tension associated with the interface has a stabalising effect on the interface and the change in free energy of the system can be associated with a change in local quilibrium liquidus tempearture at the interface [12, 45]. The curvature undercooling is proportional to the Gibbs-Thompson coefficient (defined as the ratio of the surface tension and the entropy of fusion).

2.2.2.2.2 Constitutional undercooling For the alloys, the most important effect is the constituitional undercooling due to the rejection of the solute phase from the solid to the liquid. In order for a perturbation to grow, the solute concentration gradient must be negative in front of the tip to enable the tip to reject more and more solute within the remaining liquid phase and to grow further [12, 45] . Therefore, the growth is mainly diffusion controlled in contrast to simple metals for which the growth is mainly controlled by the thermal undercooling due to the conductive and convective heat extraction.

2.2.2.2.3 Kinetic undercooling Kinetic undercooling is related to the attachement kinetic of the atoms on the atomic clusters. Rough clusters create a favourable environment for particle attachement whatever the orientation of the surface. Rough surfaces at atomistic scale create smooth surfaces at micro level and are, therefore, associated with a small kinetic undercooling. On the other hand, smooth atomistic surfaces will lead to faceted surfaces at micro level and are associated with a high level of kinetic undercooling [5, 12].

2.3 Modelling the microstructure formation

The influence of the morphological aspects of microstructure on the final cast properties and the complexity of their formation call for a reliable and physically based method of microstructure modelling. The need for modelling becomes even greater when one considers only the cost and time consuming aspects of the experimental procedures and the fact that few parameters can be really monitored during the experiment, especially within the transition zone of interest. As mentioned in Chapter 1, the clusterisation of particles to form stable solid nuclei

due to the variations of local density, is a stochastic process. On the other hand the growth of existing nuclei due to the total undercooling is a combined deterministic and stochastic process due to the moving interface undergoing surface fluctuations. Therefore to model the nucleation and growth at the same time one needs to take into account both of these aspects. In addition to these processes, the crystallographic anisotropy will also influence the growth procedure as described for the columnar growth. Different models focus on different aspects of the whole process. We can divide the microstructure modelling methods into four major groups as follows.

- The deterministic models using first principle thermodynamic calculations of grain nucleation and growth, comprising the solute diffusion and segregation.
- The probabilistic models using statistical or stochastic distributions for nucleation and growth, taking into account the crystallographic anisotropy and preferential growth directions.
- Combined probabilistic and deterministic models for nucleation and growth.
- Micro-macro models, linking the microstructure evolution at the micro level to the temperature and flow field at the macro level.

What makes the modelling of the microstructure difficult is the notion of a stochastic nucleation, based on the value of the local undercooling, and grain growth and competition due to the thermal, solutal, kinetic and curvature effects within an anisotrope crystalline structure and imposed external heat and fluid flow fields. Therefore, a comprehensive model of microstructure formation must take into account all these aspects simultaneously, which is difficult to achieve. In the following a short review of each one of these methods is given. In this Thesis a combined probabilistic and deterministic approach to microscale modelling of the microstructure was adopted with links to atomistic and macroscopic levels as shown in Figure 1.

2.3.1 Probabilistic models

In all the probabilistic models the need for a modelling procedure capable of reproducing the randomness of the process is compulsory. There are several well known procedures, such as Monte Carlo [13, 15] and Cellular Automata [37, 15], which allow us to implement probabilistic behaviours based on a predefined set of rules. Spittle et al. [50] proposed a method based on the Monte Carlo simulation in order to simulate the solidification of small castings. This model is purely probabilistic and non-deterministic. It is an adaptation of the Monte Carlo method used to simulate several solid state transformations such as recrystallisation [51, 52, 53, 54]. The model is based on the minimisation of the energy of the solid-liquid interface. This is achieved by considering the unlike sites (different sites) and by allowing the transformation (from liquid to solid or vice versa) to occur between these sites on the basis of randomly generated numbers. The selection of the grains on the surface of the mould and also the columnar-to-equiaxed transition are reproduced by this method. In addition to the limitations inherent in any probabilistic model, this model has the disadvantage that it depends on the directionality of the Monte Carlo network used for the simulation, also the way the grains are selected in the columnar zone does not reflect the true crystallographic anisotropy.

Monte Carlo methods are also used to predict qualitatively the growth of grains and the evolution of the microstructure with time, as proposed by Srolovitz et al. [55]. In this model the distribution of grain size and location is predicted in the presence of particle dispersion in the melt.

An example of Cellular Automata model (CA) used for grain recrystallisation is given by Hesselbarth [56]. In this model the CA is used to model the kinetics of the grain nucleation and recrystallisation of copper. Due to the stochastic nature of grain nucleation during the solidification or the recrystallisation [5], these probabilistic approaches provide us with a good qualitative representation of the microstructure, such as the selection of the grains in the columnar zone and the columnar-to-equiaxed transition, but they cannot reproduce quantitatively accurate results regarding the influence of the solute concentration on the grain structure as they do not count for the real physics of the problem. These models are mainly

suitable for modelling the nucleation process. These models can provide us with qualitative information regarding different variables influencing the microstructure and can allow us to distinguish between the important and less important process or alloy parameters, without providing us with quantitative details on the grain size, grain distribution or the grain growth velocity.

2.3.2 Deterministic models

Deterministic models are based on the solution of the solute diffusion equation and its coupling to the mass and momentum conservation equations [57]-[58]. One of the most important growth models based on the solute phase diffusion is proposed by Kurz et al.[57] known as the (KGT) model. This model which is discussed in the following section, describes the growth of dendritic structures as well as planar interfaces near the limit of absolute stability and for marginally stable interfaces as described in Section 2.2.2. Hunt et al.[59] proposed a similar method for the evolution of the cellular and dendritic structures. This model describes steady state or non-steady state cellular growth of an axisymmetric cell or dendrite structure. It solves for the solute phase diffusion in the liquid using finite difference methods. Heat flow is also included by assuming a moving linear temperature field. Rappaz et al. [60] proposed a diffusion-controlled growth model for the simulation of an equiaxed dendritic grain, based mostly on the KGT model. The main assumptions of this model is that the main factor influencing the growth is the constitutional undercooling and that the dendrite interface is an iso-concentration surface (as this is the case near the absolute stability). This model predicts the evolution of the diffusion layer around the dendritic interface by considering a total mixing of the solute within the liquid phase and no back-diffusion within the solid. The diffusion around the envelope of the dendritic grain is supposed to be spherical (isotropic). As in the case of Hunt's approach, [59] a finite difference method is used to discretise the diffusion equation. Similar methods were proposed by Wang et al. [61] and Gandin et al. [62] for the growth of the equiaxed and columnar zones. Some models like the one proposed by Beckermann et al. [63] also consider the effect of solute movement by convection due to the

thermal field. The back-diffusion in the solid phase can be modelled by a model like the one proposed by Tong at el. [64] using a diffusion boundary layer and the concept of finite-rate solute diffusion in solid as well as in liquid phase. A three-dimensional equiaxed dendritic growth model was recently proposed by Steinbach et al. [66]. This model is based on the calculation of the temperature field between the grain envelopes, defined as smooth surfaces enveloping the dendritic structures and the notion of stagnant-film growth for dendrite tips, proposed by Cantor and Vogel [67], as an improvement to the well-known Ivanstof solution of the heat flow equation around a growing isothermal paraboloid of revolution representing the dendrite tip [5, 12]. The Ivanstof solution is also used in the KGT model [57]. These models are suitable for modelling the growth process even in the presence of a convective flow and they do provide us with accurate quantitative results regarding the final grain size and the growth velocity.

The validity of these deterministic models is limited because they do not take into acount the grain selection on the surface of the mould based on the crystallographic orientation of the grains and, therefore, the columnar and columnar-to-equiaxed transition zones can not be predicted as mentioned by Rappaz et al.[68, 69].

2.3.3 Combined stochastic and diffusion controlled growth models

In order to take into consideration the real physics of the growth and also the stochastic nature of the grain nucleation and crystallographic anisotropy, models combining the Monte Carlo or Cellular Automata models for the grain nucleation and diffusion controlled models for the growth were proposed [70]-[73]. One of the early models, proposed by Maxwell et al. [70], was based on the heterogeneous nucleation of the grains computed for the various grain densities, coupled to an spherical diffusion controlled growth. An important contribution to these models was proposed by Rappaz et al. [68]. In this model an empiricallly fitted statistical distribution to an experimentaly obtained cooling curve is used to simulate the nucleation process.

This distribution is used to calculate the number of newly nucleated grains at each time step and per unit volume, for a given increase in the undercooling. These values are used in

a cellular automaton code to simulate the nucleation process. The growth is based on the KGT model described earlier. A similar model for the nucleation and growth of the equiaxed grains in a three dimensional space as an extension to the two dimensional model described in [68] was also proposed by Rappaz et al. [73] using octahedral cells instead of squared cells. Methods proposed by Rappaz et al. are mainly applied to dendritic alloys and they do not consider the fluid flow due to the convection or pouring process.

Charbon et al. [71] proposed a three dimensional stochastic model for the nucleation and growth of eutectic alloys in the presence of the grain sedimentation and thermal convection. They considered the impingement of already nucleated grains, which were randomly distributed in a uniform and unsteady temperature field. The important factor considered by these authors was the fact that grains were allowed to move within the solidifying liquid. Grains were considered to be spherical and their movement was modelled by a change in their center of mass coordinates.

One of the advantages of these models is that they can acount for the preferential growth directions and the columnar-to-equiaxed transitions. They provide us with a qualitatively correct microstructure and a more detailed morphology of these microstructures at the end of the solidification on based of which mechanical properties can be predicted.

2.3.4 Micro-macro models

A range of models, coupling different microscale models as discussed above, to the macroscale models for the solution of general enthalpy equation [38] have been proposed [74]-[82]. The link between the micro and the macro scales is mainly established by incorporating the evaluation of the release of the latent heat within the macroscale volume mesh, provided by a cellular automata model, into the general heat or enthalpy equation for heat transfer. An example, using the controlled volume method for the macroscale and a cellular automamta model for the microscale, was proposed by Lee et al. [74] and applied to a planar flow casting. An earlier model, which can be applied to both dendritic and eutectic structures, coupling a finite element method for the macroscale to a cellular automata for the microscale was proposed by Thevoz

et al. [75]. This model takes into account the nucleation of grains within an undercooled liquid as well as the growth kinetics of the dendrite tips of the eutectic front and in the case of dendritic alloys, the solute balance at the scale of the grains. In this method a two level time stepping model is proposed which avoids the bouncing effects of reheating meshes and which improves the convergence of the results. One of the models proposed for linking the change in fraction solid due to the microscopic solidification kinetics and the evaluation of the source term in heat transfer equation was proposed by Stefanescu et al. [76] in which a computer aided cooling curve analysis was coupled to a CA model. For a given fraction solid obtained by the micromodel, the new temperature field was calculated and fd back to the micromodel.

One of the most elaborate micro-macro models, combining the stochastic nucleation, diffusional growth and macroscopic heat conduction was proposed by Gandin et al. [77] as an extension to the stand alone CA model. This cellular automata finite element model (CAFE) applies to a non-uniform temperature field. The temperature at each cell location and each time step is interpolated using the values at neighbouring nodal points in the finite element mesh which in turn will be used to calculate the evolution of the microstructure using the CA code. The corrected solid fraction is fed back into the FE code to evaluate new temperature field.

A somewhat novel approach, using the *morphology-independent-stereological* parameters was proposed by Marsh et al. [78]. In this model, the coupling of micro and macro models is achieved via the association of a unit volume of microstructure to each grid point. Therefore, the state variables at each grid point represent the average conditions within the unit volume of microstructure. An advantage of this method is the fact that both macro and micro models are treated at the same length scale and the numerical mesh spacing determines the spatial resolution of the microstructure. Stereological parameters such as, volume fraction and specific surface area per node, are used to evaluate the microstructural geometry. An interesting model, predicting the average microstructural lengthscale was proposed by Martin et al. [79]. This model deals with the coarsening processes at the microscale and predicts the evolution of the primary and secondary dendrite arm spacings with respect to process parameters such as the solidification time and cooling rate.

As a summary we can say that in all these models, the variation of the solid fraction during the solidification is calculated using the microscale model and the result is passed to the macroscopic model for the calculation of the latent heat released and therefore the evaluation of the new temperature field which in turn will be passed to the microscale model to determine new fraction solid. The macroscale model is based on a finite element or finite volume method [38, 83, 84] and is solved for a given number of nodes and time steps.

2.4 Modelling solidification at microscale

2.4.1 Introduction

In this Thesis, the Rappaz et al. [68] microscale model is used as a basis for the microstructure modelling. This model was chosen due to its ability to reproduce the correct physical tendencies of the microstructure evolution based on process and alloy parameters, such as cooling rate and alloy composition. As shown in Figure 1, the Rappaz model gets its input from the nanoscale model and its output is used as input to the macro model to be described in Chapter 3. Before describing the Rappaz model, the notion of cellular automaton (CA) and the kinetics of the dendrite tip growth, described by Kurz et al. [57], known as the KGT model of grain growth, will be detailed since in the Rappaz model, the nucleation process is based on the use of CA and the tip growth velocity is obtained via the KGT model.

The nanoscopic extension to the Rappaz model will follow, divided in two parts, one related to the nucleation process and the second one related to the dendrite tip growth process.

2.4.2 Cellular automaton

What is a cellular automaton? Briefly, we can say that *cellular automata are stylised, synthetic universes defined by simple rules much like those of a board game. They have their own kind of matter which move around in a space and time of their own.* [37]. A cellular automaton is a discrete dynamical system whose behavior is completely defined by a set of predefined rules based on local relationships between neighbouring cells which discretise its space domain.

They can be used to simulate a great number of physical systems. Their ability to simulate deterministic as well as probabilistic processes, based on imposed internal and external variables of different type, make them appropriate for the simulation of complex processes such as the microstructure formation during solidification. In any cellular automaton model, four important aspects of the model must be well defined, in order for CA model to work.

- How the space is discretised?
- For each cell within the discretised space, what are the variables associated with it?
- What are the states defined for each cell?
- What are the rules defined for the state evolution of an individual cell within the CA environment?

In the case of a 3-dimensional space, each cell can be a polyhedral unit volume. One of the most widely used for a volume is an octahedral unit volume. In the case of a 2-dimensional space, polygons can be used to discretise the domain. Squares and hexagons are the most commonly used.

Variables used to define the system are those characterising the physical process. In the case of solidification, the local temperature, tip velocity and solid fraction can be used as the set of physical variables defining the system.

The state of each cell must be one of the possible states defined for the whole sytem which in the case of solidification can be zero or one for solid or liquid states respectively. A continuous range of states is also possible to consider, for example zero for solid, one for liquid and anything between for the mushy zone characterising the relative value of the solid fraction (value between 0 and 1) of the individual cell.

Transition rules can be of two kinds, global or local [15]. Global rules are used when for each individual cell, the transition from one state to another, during the time is influenced by the states of all the other cells. Local rules, which are more commonly used, are based only on the neighbouring cells of each cell and/or its own previous state.

2.4.3 Cellular automaton used in the Rappaz model

The CA model used to simulate the nucleation and growth of the dendritic structure during solidification, is based on the discretisation of a 2-dimensional space by using the square cells. The local temperature and tip velocity is associated to each cell and there are two possible states, liquid or solid. The transition rules are local and are based on *von Neumann* neighbouring rules which considers the influence of the first neighbours of each cell for the state evolution for each time step (the neighbouring environments are also possible such as the *Moore* environment which considers the first and second neighbours). To summarize the CA model used by Rappaz

- The 2-dimensional space is divided into cells of equal size, squared shaped and arranged in a regular lattice.
- Each cell is characterised by local temperature, crystallographic orientation and states, such as liquid or solid.
- The neighbouring environment is characterised by the von Neumann rule for first neighbours.
- The rules of transition (e.g. liquid-solid) of a cell during time evolution, are defined according to the values of variables and states of its first neighbouring cells.

2.4.4 The Kurz, Giovanola and Trivedi (KGT) growth model

The fact that dendritic structures are produced during the solidification of metallic alloys demonstrates that the planar interface is unstable and any perturbation originated on the interface will grow within the open region of the liquid [5, 12]. These growing perturbations produce the dendrite tips and as described in Section 2.2.2, they are *marginally unstable* [12, 57]. The solid-liquid interface is near the limit of the *absolute stability* which means that at high velocities, the interface is stabilised by the combined effects of thermal and solutal diffusions and the capillarity effect, driven by surface tension [5, 12, 57] as described in Section

2.2.2. The wave length of the interfacial perturbations near the absolute stability defines the minimum dendrite tip radius imposed by the diffusion length and tip curvature [57]. For the alloys the main growth factor for dendrites, from their initial radii, is the solute concentration gradient in front of the tip, providing the thermal undercooling due to the local thermal gradient can be neglected [5, 12]. Therefore the driving force of the dendritic growth can be defined as solute supersaturation, defined as [57]:

$$\Omega = \frac{C^* - C_\circ}{C^*(1-k)} = I_v(P_e)\,, \tag{2.2}$$

where Ω is the supersaturation (the excess of the solute concentration in the liquid phase in comparison to the solubility limit of the solutal phase in the liquid), $C_\circ$ is the initial solute concentration, C^* is the solute concentration in the liquid at the tip, k is the partition coefficient (the ratio of solute concentration in the solid and liquid phases) and $I_v(P_e)$ is the Ivanstov function of the solute Peclet number, where the Peclet number is defined as [38, 57]:

$$P_e = \frac{Rv}{2D}\,, \tag{2.3}$$

where R is the tip radius, v the tip velocity and D the tip diffusion coefficient. The value of the dendrite tip radius, based on the growth velocity and undercooling, is given by [57]:

$$R = 2\pi\sqrt{\left(\frac{\Gamma}{mG_c\xi_c - G}\right)}\,, \tag{2.4}$$

where Γ is the Gibbs-Thomson coefficient (defined as the ratio of the surface tension and the melt entropy), m is the slope of the alloy phase diagram, ξ_c is a function of Peclet number, which is close to unity for low growth velocities and is approximated by $\xi_c = \frac{\pi^2}{kP_e^2}$ at high growth velocities and low temperature gradients [57], G_c, is the solute concentration gradient, and G is the temperature gradient. The undercooling is related to the supersaturation via [57]:

$$\Delta T = mC_\circ\left[1 - \frac{1}{1-\Gamma(1-k)}\right]\,. \tag{2.5}$$

Assuming a paraboloid of revolution as the geometrical form of dendrite tips and no back diffusion in the solid state and a saturated liquid at the dendrite tip [57], the solution to eqns. (2.2) - (2.5) will provide us with a quadratic equation giving the value of the dendrite tip growth velocity for a given undercooling [57]:

$$\begin{aligned} & A v^2 + B v + C \,, \\ & A = \tfrac{\pi^2 \Gamma}{P_E^2 D^2} \,, \\ & B = \tfrac{m C_o (1-k) \xi_c}{D[1-(1-k) I_v(P_e)]} \,, \\ & C = G \,, \end{aligned} \tag{2.6}$$

where [57]

$$I_v(P_e) = P_e \exp(P_e) E_1(P_e) \,, \tag{2.7}$$

where $E_1(P_e)$ is the first Eulerian integral. Using this expression we can calculate, at each time step, the dendrite tip growth velocity based on the interface undercooling.

The KGT model is a good approximation to the solute diffusion at the dendrite tips with nearly realistic geometrical assumptions on the dendrite tip geometry and can be applied to a range of growth velocities from the limit of solute undercooling to the absolute stability.

2.4.5 The probabilistic Rappaz model of microstructure formation

This model, based on the use of the CA model, can be divided in two different parts, one related to the nucleation phase, which is purely random, and the second to the growth phase, which is diffusion controlled [68, 69]. In this model the temperature field is supposed to be uniform and therefore all cells have the same temperature at each time step (time-dependent, isothermal field), therefore the ΔT_{temp} can be neglected which allows us to consider the same growth kinetics for the columnar and equiaxed growth [68]. The attachement kinetics is also neglected, therefore the main growth factor is the constitutional undercooling. The incubation time for grains, the time necessary for the transformation of a stable spherical grain to an unstable dendritic grain, is neglected as well as the coarsening effects of the secondary and ternary arms. Based on these assumptions, we can consider three factors to be responsible for

the nucleation and growth of the grains:

- The heterogeneous nucleation of the grains in the bulk and on the surface of the mould.
- The preferential growth directions due to crystallographic anisotropy.
- The growth kinetics of the dendrite tip based on the KGT model [57]

Due to the uniformity of the temperature field, which in turn implies the uniformity of the constitutional undercooling, the liquid-solid interface made up of the dendrite tips can be considered as an isoconcentration surface of the solute [68].

2.4.5.1 The nucleation process

At the start of the process, cells are at the same temperature above the liquidus and their state is liquid. The cells on the mould's walls, carry a special reference number [68]. When the time stepping begins, the temperature at each time step, δt, is given by the cooling curve of the alloy, normally obtained experimentally, or from a heat flow calculation solving the enthalpy equation [77]. For a time step, the variation in the undercooling, $\delta(\Delta T)$, is calculated. This in turn is used to calculate the number of newly nucleated grains per volume, $\delta n_v = n_v\left[\Delta T + \delta t(\Delta t)\right] - n_v(\Delta T)$,

$$\int_{\Delta T}^{\Delta T+\delta(\Delta T)} \frac{dn_v}{d(\Delta T')} d(\Delta T') \,. \tag{2.8}$$

The function giving the value of grain density for a given undercooling, used in the integrand, is an empirical function having the functional form of a Gaussian distribution and fitted to the experimental data [68, 69]. This empirical Gaussian distribution is fitted to satisfy the maximum grain density and to reproduce the columnar-to-equiaxed transition which occurs due to the competing growth and nucleation processes between the growing grains on the mould's walls and the nucleation of new solid nuclei within the liquid bulk.

Choosing a Gaussian distribution for the temperature-dependent grain density corresponds to the fact that a continuous nucleation theory of nuclei of different critical radii is assumed

over the whole freezing range of the alloy [5]. The nucleation density which is the integral of this function will be a step-like function with an inflexion point [68, 69]. In theory, if the cooling rate is high enough, the big-bang nucleation can be observed which corresponds to a Dirac distribution function to which corresponds a step function representing the grain density [5].

The same procedure is applied to the surface nucleation with a different grain density distribution on the surface of the mould given by a different Gaussian distribution having a smaller minimum undercooling [68]. The lower undercooling for the surface distribution is due to the fact that on the mould's surface, due to the existence of the impurities and also the surface roughness, heterogeneous nucleation is taking place which decreases the critical undercooling for nucleation of grains.

The characteristics of the bulk and surface distributions (the mean undercooling, standard deviation and the maximum grain density) can only be determined via experimental observations and their asymptotic fitting [68, 69].

Based on these two distributions, for each cell in the cellular automaton network we can define, at each time step, a probability P_v indicating the chance that a new nucleus nucleates

$$P_v = \frac{\delta N_v}{N_{ca}} = \delta n_v \frac{V}{N_{ca}} = \delta n_v V_{ca} \,, \tag{2.9}$$

where N_{ca} is the total number of cells in the network, V is the total volume and V_{ca} is the volume per cell. Stereological transformations giving the number of newly nucleated grains within a two dimensional space are used:

$$\begin{aligned} n_v &= \sqrt{\tfrac{\pi}{6}\left[n_v^*\right]^{\frac{3}{2}}} \\ n_s &= \tfrac{\pi}{4}\left[n_s^*\right]^2 \end{aligned} \tag{2.10}$$

in which $n_s^*[m^{-2}]$ and $n_v^*[m^{-3}]$ are the site densities for the surface and bulk nucleation respectively in the CA model.

During each time step, all of the cells are scanned and for each of them a random number $r(0 \leq r \leq 1)$ is generated. If the cell is in the liquid state and if $r \leq P_v$ then the cell

transforms into solid and a randomly generated number between 1 and 48 is assigned to the cell representing its ⟨100⟩ crystallographic direction relative to the x axis. In the case of cubic systems for which we have a four-fold symmetry, only grains with relative orientations of 0 to 90° need to be considered and by dividing the interval to sub intervals of 2°, we obtain an interval of 1 to 48, used as a numerical representation of the grain's crystallographic orientation and assigned randomly as mentioned above.

The ⟨100⟩ direction is chosen due to the fact that the preferential growth direction for cubic systems is along the ⟨100⟩ direction [68].

The remelt of dendrite arms is considered as at each time step all the CA cells are scanned and not only those which are still liquid. Therefore, the number of potential nucleation sites considered is smaller than it would be. This decrease in the number of potential nucleation sites can be considered as a decrease in total number of grains due to the remelt of some of the nucleated grains [68].

2.4.5.2 The grain growth

Once a grain has nucleated, its growth must be calculated based on its crystallographic orientation and nearest neighbours. Since grains are considered as square shapes and due to the uniformity of the temperature field at each time step, each solid cell will grow as a square. Therefore, the four corners of each solid cell can be considered as growing dendrite tips [68]. The distance moved by each dendrite tip between its nucleation time t_n and time t is given by:

$$L(t) = \int_{t_n}^{t} v\left(\Delta T(t')\right) d(t') \tag{2.11}$$

where v is the tip velocity. The expression giving the tip velocity for a given undercooling is obtained by KGT model.

If we consider a grain denoted by A, based on von Neumann rule, it has four neighbours B_1 , B_2 , B_3 and B_4 as shown in Figure 2.1. In order for a tip of cell A to grow and to trap

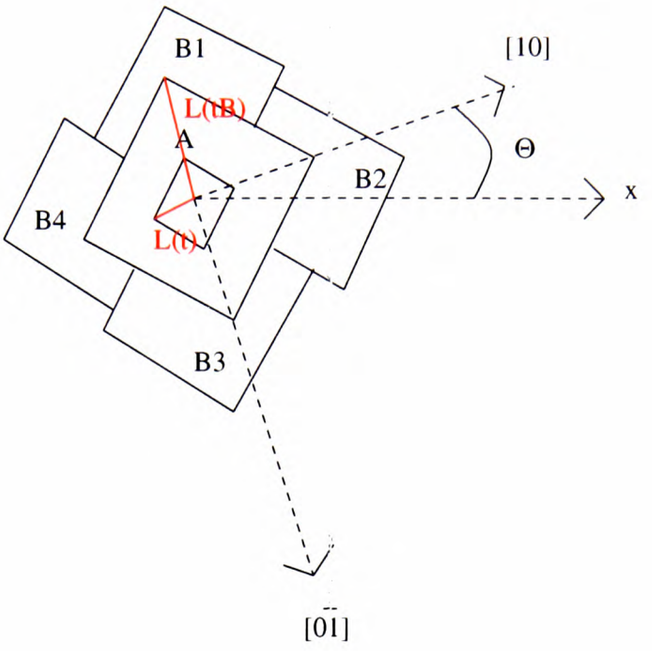

Figure 2.1: Grain growth in Rappaz Model

its neighbours the distance $L(t_B)$ given by [68]:

$$L(t_B) = l_\theta = l(\cos\theta + \mid \sin\theta \mid), \tag{2.12}$$

where l is the distance between cells, must be covered by the dendrite tip with orientation θ with respect to the x-axis (the orientation is defined as the direction of the $\langle 100 \rangle$ crystallographic direction). During the time step δt the distance $L(t)$ can be smaller than l_θ due to the diffusive behavior of the dendrite tip as a consequence of thermal agitation, self diffusion of the substrate atoms and diffusion of the solute phase particles (what is called globally the diffusional noise) [68]. Therefore, we can define a growth probability which is a function of the undercooling and grain orientation

$$P_g = \frac{L(t)}{l_\theta} \tag{2.13}$$

where P_g is the probability for a solid cell to be extended to its nearest neighbours if they are still liquid, during δt. Therefore, for each one of the B cells, which are still liquid and

have a certain probability to be captured by cell A, we assign a random number r_g, where $(0 \leq r_g \leq 1)$, and if $r_g < P_g$ then the considered cell will become trapped and the orientation of the cell A will be assigned to it. Once the growth of cell A is finished by trapping all its first neighbours, it will not be considered any more and the growth of B cells will be considered and the process continues. As the growth is calculated for all solid cells at each time step, the grain growth competition, based on the $\langle 100 \rangle$ crystallographic directions, will select the most favourable directions based on the alignement of the $\langle 100 \rangle$ direction with the direction of the heat flow within the solidifying alloy. In addition to the growth competition at each time step, the nucleation of new nuclei at each time step can stop the growth of already solidified grains [68].

One of the disadvantages of this kind of growth procedure is its dependency on the cellular automata network due to the fact that only the first neighbours have been considered for the growth calculation of each solid cell [68]. In order to overcome this problem, we can either consider the first and second neighbours (Moore model) [15] or apply at each time step and to each solid cell a correction procedure such that at each time step, the positions of the four dendrite tips of cell A are corrected using one triangle at each side of the cell A. Any liquid cell which will be trapped by any of these triangles will become solid and a part of the growing grain as can be seen in Figure 2.1.

2.5 Nanoscopic extension of the Rappaz model

We now consider our extension of the Rappaz model [68] in which we replace the *empirically-based* temperature-dependent grain distribution used in that model with the microscopic density of the newly nucleated grains *computed* at each time step, from the data generated at the atomistic scale via the Molecular Dynamics (MD) simulation technique [16] and reported in Chapter 1. Our approach, therefore, provides a nanoscopic input to the Rappaz model, giving a physically sound basis for the nucleation phase and making it independent of experimental observations and empirical considerations.

We then introduce a *stochastic dynamics* into the CA-based simulation of the *growth stage*

of the dendritic grains in the Rappaz model, by treating the dendrite tips, i.e. the corners of the nucleated CA cells in that model, as stochastically propagating points executing a combined drift-diffusion motion, described mathematically by the Ito stochastic differential equation [85]. The diffusion coefficeint which is used in the Ito stochastic dynamics is also calculated at the atomic level. Links between the nano and the micro scales are shown in Figure 1.

2.5.1 Computaion of the grain density

As described in Chapter 1 the nucleation rate depends on the values of the residual chemical potential, surface tension and a shape factor representing the geometrical characterisation of the nucleus

$$I_v[\Delta T] = 10^{33} exp\left[\frac{-4\eta^3\gamma^3}{27k_{\mathrm{B}}T\Delta\mu^2}\right], \tag{2.14}$$

given in Chapter 1.

In order to compute the nucleation rate and, therefore, the nucleation density which is used as input to the nucleation part of the Rappaz model, via nanoscopic simulations, the values of the residual chemical potential used in eqn. 2.14 were obtained via MD simulations applied to atomic clusters. Therefore, the coupling between the nanoscale and the nucleation part of Rappaz model is based on the evaluation of the variation of the residual chemical potential during the solidification as shown in Figure 2.2. To do so, a series of classical MD simulations were performed in which the energetics and dynamics of the clusterization process of an assembly of atoms during the cooling of a molten atomic liquid were derived from the many-body interatomic potentials [23, 16] as described in Chapter 1. The values of the residual chemical potential, $\Delta\mu$ [23, 16] were computed at different temperatures as described in Section 1.6.6. From I_v we then obtain the δn_v (see Figure 2.2)in eqn. (2.9) as

$$\delta n_v = I_v \times \delta t \tag{2.15}$$

where $\delta t = 1s$ is the CA-based simulation time step. For the nucleation on the rough surface

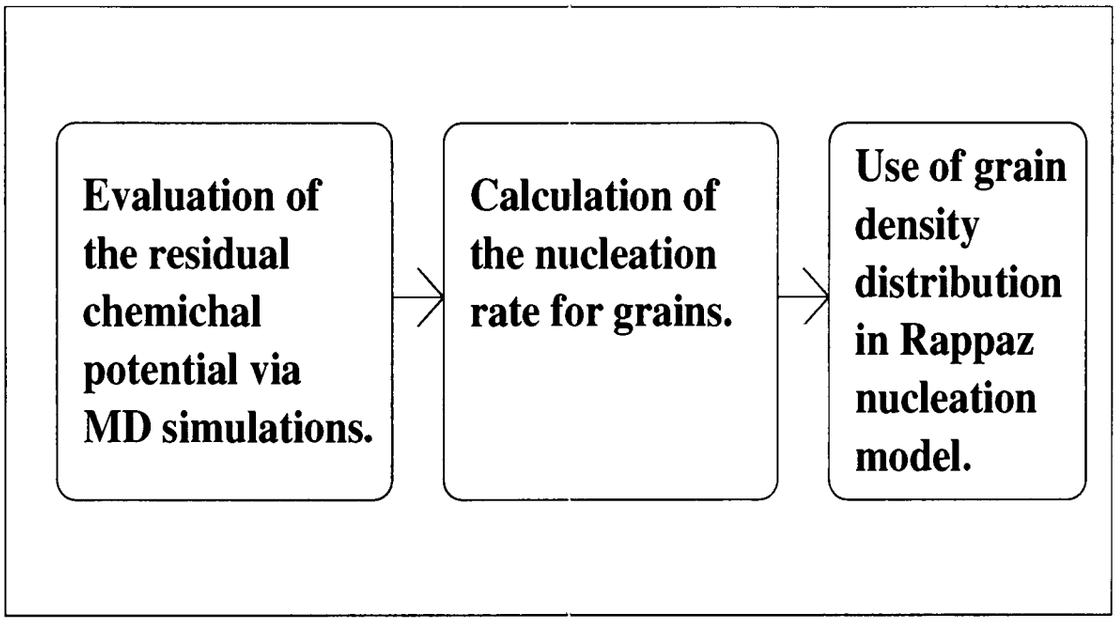

Figure 2.2: The coupling of the nanoscale and the nucleation part of the Rappaz model via the evaluation of the $\Delta\mu_{res}$ using MD simulations.

of the mould or on the impurities in the liquid bulk, we have [5]

$$G_{\Gamma_s} = G_{\Gamma_v}(2 - 3\cos\phi + \cos^3\phi)\,, \tag{2.16}$$

where ϕ is the contact angle at the liquid/mould interface or the liquid/impurity interface in the bulk defined as

$$\cos\phi = \frac{\gamma_{l,imp} - \gamma_{s,imp}}{\gamma_{l,s}}\,, \tag{2.17}$$

where $\gamma_{s,imp}$, $\gamma_{s,l}$and$\gamma_{l,imp}$ are respectively, the solid-impurity, solid-liquid and liquid-impurity surface tensions. Once the bulk and surface grain densities are calculated for different temperatures, and therefore cooling rates, via atomistic calculations, they can be used directly in the Rappaz model as shown in Figure 1.

2.5.2 Stochastic extension of the growth phase

In the Rappaz model, due to the use of an isothermal field at each time step, the growth velocity calculated via the KGT model described in Section 2.4.4 is the same for all the corners of each individual cell which are considered as dendrite tips for that particular cell. Even if this method is capable of reproducing some aspects of dendritic structures, it really doesn't take into account the whole physics of the dendrite tip growth. The drift velocity of the liquid-solid interface calculated by the KGT model and based on the solute diffusion, due to the build up of the solute concentration near the interface is only one of the aspects of the growth phenomenon, representing the average behavior of the interface. This deterministic velocity must be used in the context of a combined drift-diffusion or drift-stochastic growth. The notion of diffusional growth of a dendrite tip must be understood in the context of the diffusional noise, combining the thermal agitation of tips, the self-diffusion of the substrate's atoms at the tip and the diffusion of the solute atoms present at the tip.

We therefore justify our stochastic model of grain growth, since in the Rappaz model the tip velocity represents the *average* velocity of the moving liquidus isotherm without taking into account the *random contributions* to the tip motion due to the *marginal instability* [5, 12],

according to which the moving interface is on average of a planar topology while undergoing stochastic fluctuations. These fluctuations can lead to the creation of dendritic or cellular structures (dendritic for velocities less than the absolute stability limit and cellular for velocities higher than the absolute stability [57, 87]) during solidification of alloys due to the morphologically unstable liquid-solid interface under the destabilising effects of constitutional undercooling [86], thermal agitation and self-diffusion.

The interface is stabilising due to the surface tension effect and kinetic anisotropy [86, 87]. In order to implement the drift-stochastic motion of the tips, the *Ito stochastic dynamics* [85] was used. The Ito stochastic differential equation is applied [85]

$$d\mathbf{r}(t) = \mathbf{A}[\mathbf{r}(t), t]dt + D_{\tilde{c}}^{\frac{1}{2}} d\mathbf{W}(t)\,, \tag{2.18}$$

to describe the space-time trajectory of the tip (fluctuation), where the first term, $\mathbf{A}[\mathbf{r}(t),t]$, describes the dynamical variable of the dendrite tip and is referred to as the deterministic drift velocity of the moving liquidus isoterm, the second term is the stochastic contribution and $d\mathbf{W}$ is a given Gaussian Wiener process. As it can be seen in eqn. (2.18), the stochastic term depends on the diffusion coefficient of the atomic system. This value is calculated directly at the nanoscale, therefore, the coupling factor between the nanoscale and the growth part of the Rappaz model is the system's diffusion coefficient as shown in Figure 2.3. Details of the numerical implementation of this equation can be found in [88]. The drift velocity is obtained from the KGT model in a similar fashion to the Rappaz model, where the cell undercooling is used in the parabolic equation of the Ivanstov from which the drift velocity is calculated.

2.6 Applications and Discussion

2.6.1 Introduction

The results presented in this Chapter are aimed at validating the nano-micro model proposed earlier in this Chapter. Three type of validations are necessary for the model.

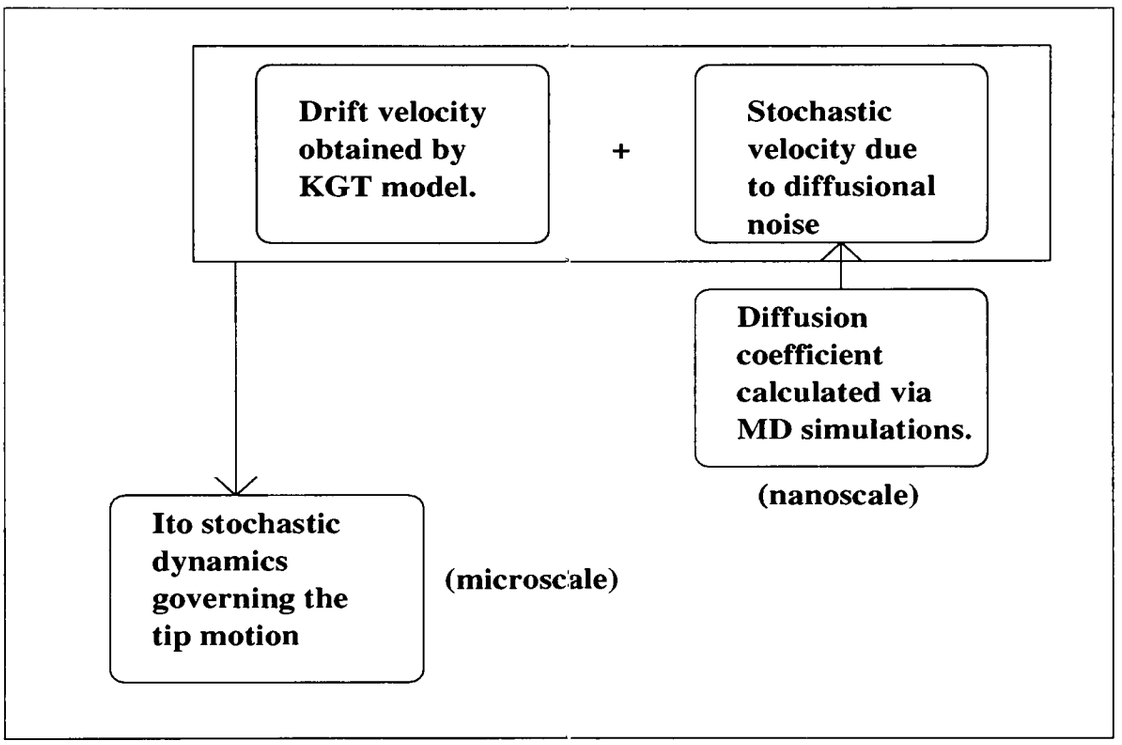

Figure 2.3: The coupling of the nanoscale and the growth part of the Rappaz model via the evaluation of the diffusion coefficient using the MD simulations.

- As we did not have access to the code used by Rappaz et al., the program needed to be writen and therefore, it needed to be tested in order to find out if qualitatively it can produce the same physical tendencies as the Rappaz model.

- We also did not have access to the code for KGT model therefore the program evaluating the growth velocity based on the KGT model needed to be tested in order to verify the accuracy of the calculations.

- Once the correctness of the programs were established, our nano-micro model had to be validated qualitatively and quantitatively (where possible) by comparing its results to other experimental or computational results corresponding to the similar alloy and process parameters.

Five different metallic systems were used to validate various aspects of the model.

- The Al system was used to test the Rappaz model, based on different cooling rates, growth velocities and contact angles. Results obtained were compared qualitatively with ones obtained originally by the Rappaz model [68].

- The Ag-Cu alloy, where Cu is the solute phase, was used to validate the KGT program by comparing its results to those of the original authors [57].

- The Al-3%atSn and Sn-10%wtPb alloys were used to validate the model as a whole by comparing the results to experimental results where available [50].

For each one of these simulations, two set of results are presented. First the results obtained by the atomistic simulations using MD, used as input to micro model and then, the results produced by the micro model using atomistic input. Before going further into the detailed results, the way by which results were obtained is discussed.

2.6.2 Implementation of the nano-micro model

In order to implement this coupled model, we have to proceed as follows:

- Preparation of the input file for the nanoscale simulation which must correspond to the exact percentage of the solute initial concentration and crystallographic structure of the metallic system.

- Calculation of the residual chemical potential and the diffusion coefficient using the Molecular Dynamics simulations at different tempeartures as described in Chapter 1.

- Calculation of the bulk and surface nucleation rate distributions for different undercoolings and a range of contact angles as given by eqns. (2.14) and (2.16) respectively.

- Determination of the variation of the dendrite tip growth velocity with the undercooling by establishing databases providing relationships between the velocity and radius, velocity and undercooling and undercooling and radius based on the KGT model.

- Linking the distributions and the databases to the Rappaz model to create the microstructure using the cellular automaton model.

In following sections, results from MD simulations are given without the description of atomistic simulations as they are already given in Section 1.7. Colours in the results outputed by the micro model, represent the $< 100 >$ crystallographic directions of grains with regard to the "x" axis of cellular automata grid. The correspondence between the colors and the orientations are given in Figure 2.4.

2.6.3 Results for the Ag-Cu alloys

In this Section, the values of the homogeneous and heterogeneous nucleation rates (the number of grains nucleated per unit of time and volume with contact angles of 180° or smaller respectively) as well as the critical Gibbs free energy are presented. Their variations based on the values of the contact angle and also the solute concentration are discussed. The variation of the growth velocity with different undercoolings and various solute concentrations are also given. If we consider Figures 2.5 and 2.6 obtained by the MD simulations, it can be observed that by increasing the amount of the solute phase, the critical undercooling necessary for the

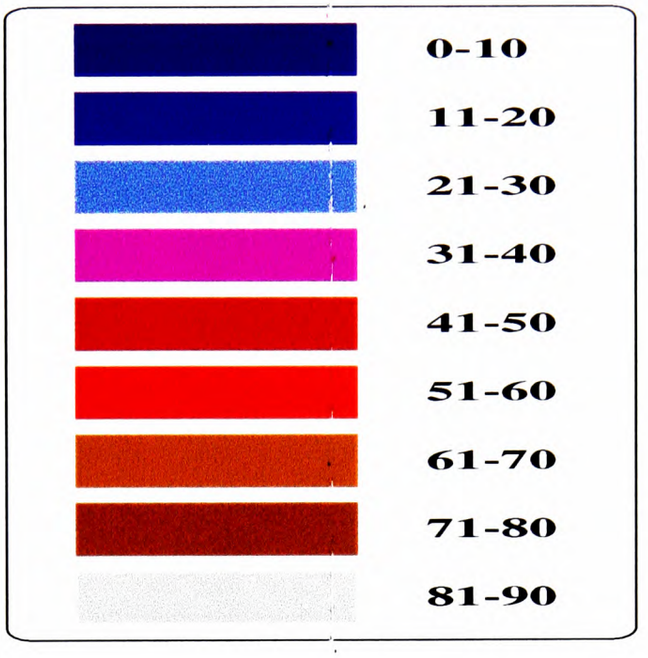

Figure 2.4: Colours used in the Rappaz output, and the crystallographic orientation of grains based on the < 100 > crystallographic orientations.

solidification decreases. This is mainly due to the increase in constitutional undercooling and a decrease in the local freezing temperature. By approaching the eutectic composition, the alloy must cool down to temperatures near the eutectic temperature after which it becomes solid rapidly with a eutectic structure. It is also shown in Figures 2.5 and 2.6, that the total amount of potential nuclei is increased. These two effects combined, will produce a greater amount of equiaxed microstructure in the case of Ag-10%wtCu than in the case of Ag-5%wtCu alloy. The effect of the contact angle is shown in Figures 2.7 and 2.8. In these Figures, the variation of the nucleation rate with undercooling for two different contact angles are given. By decreasing the contact angle from 180° for the homogeneous nucleation to 45° for heterogeneous nucleation with a small contact angle, the value of the critical undercooling was reduced from $25°C$ to only $2°C$. The reason lies within the increased possibility of clusterisation due to the decrease in critical Gibbs free energy as shown in Figure 2.9. As shown in the latter figure, the value of the Gibbs free energy was reduced from 12.25 eV to nearly 0.75 eV since nucleation of new grains on existing impurities within the bulk or in the grooves on the mould's surface

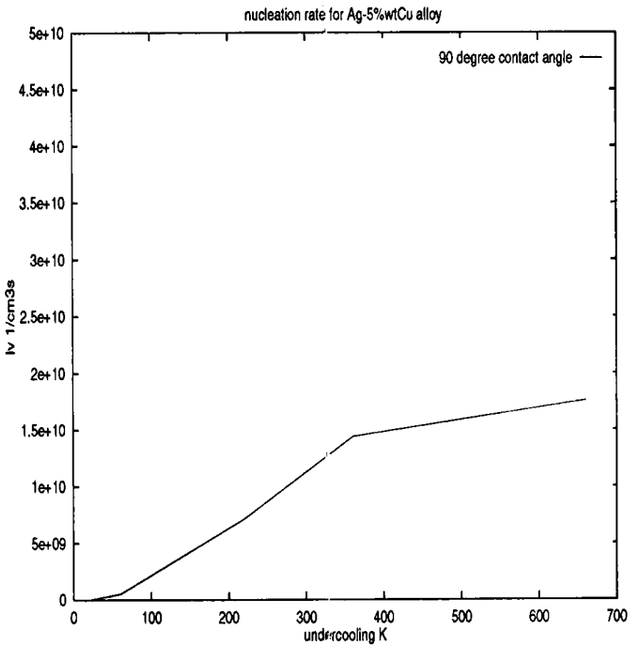

Figure 2.5: Variation of the nucleation rate with the undercooling for the Ag-5%wtCu alloy with 90° contact angle

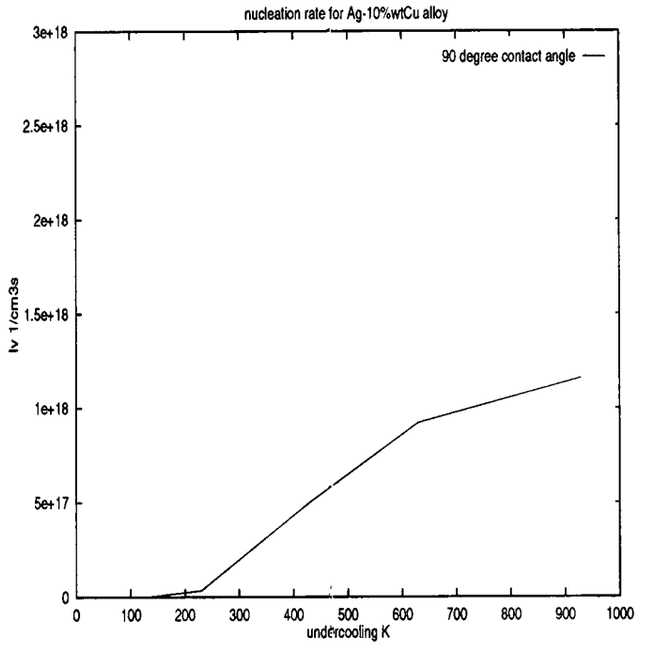

Figure 2.6: Variation of the nucleation rate with the undercooling for the Ag-10%wt Cu alloy with 90° contact angle

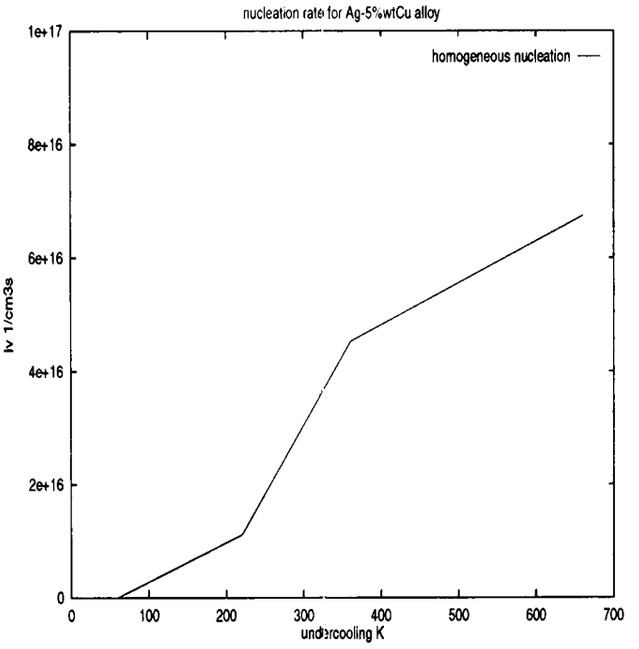

Figure 2.7: Variation of the nucleation rate with the undercooling for the Ag-5%wtCu alloy with 180° contact angle

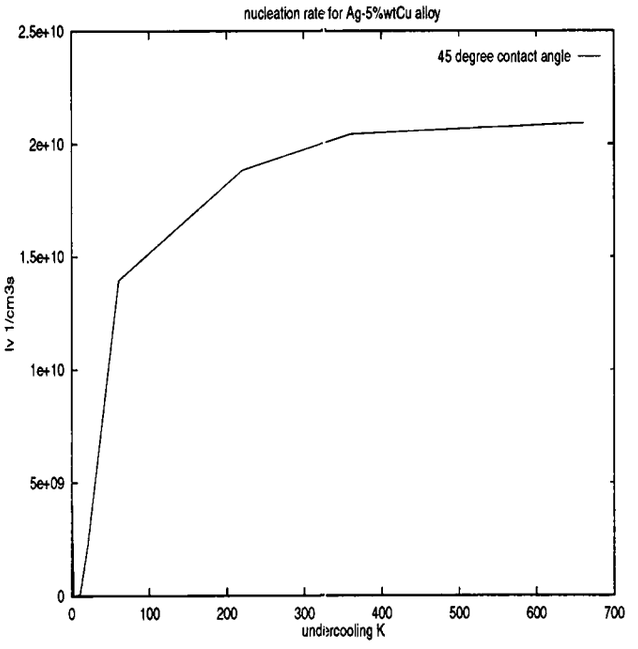

Figure 2.8: Variation of the nucleation rate with the undercooling for the Ag-5%wtCu alloy with 45° contact angle

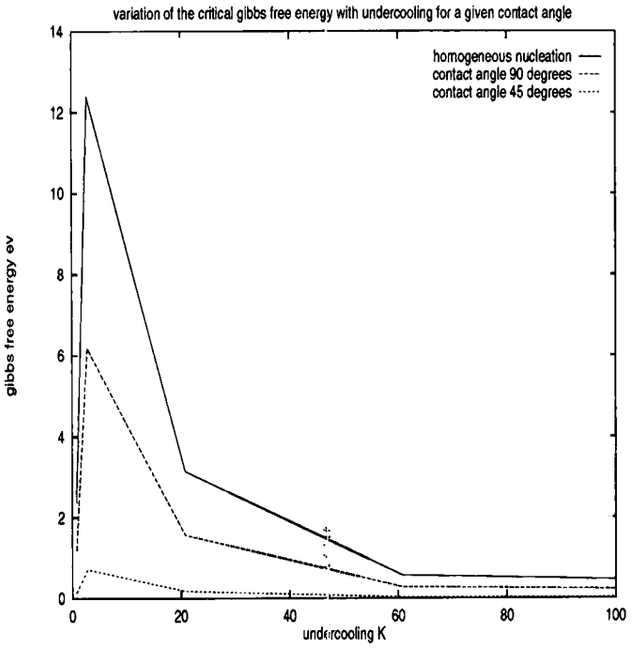

Figure 2.9: Variation of the critical Gibbs free energy with undercooling for different contact angles within the Ag-5%wtCu alloy

requires much less interfacial energy. To investigate the effects of the solute concentration on the growth velocity using the KGT model, the concentration of the Cu was changed from 2 to 25%wt. It is shown in Figures 2.10 and 2.11 that for the same undercooling, the increase in the solute concentration leads to a decrease in the growth velocity and therefore, a decrease in the dendrite tip radius from values around μm to several hundreds of $\dot{A}$, as shown in Figure 2.11.

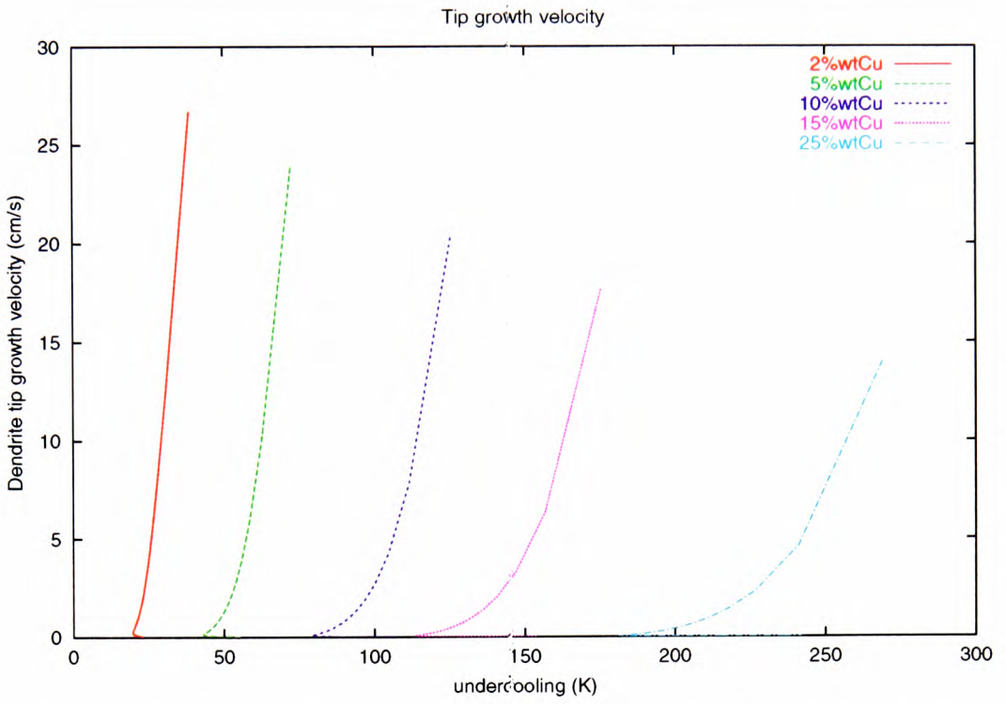

Figure 2.10: Dendrite tip growth velocity obtained via the KGT model for different solute concentrations in the Ag-Cu system.

This decrease in the growth velocity as well as in the radii of the dendrite tips is consistent with the comparison made in Figures 2.5 and 2.6, giving a higher nucleation rate for 10%wtCu than for 5%wtCu. These results are consistent as well with those calculated by the authors of the KGT model [57]. The variation of the growth velocity with the undercooling is parabolic, as described by KGT model.

2.6.4 Results for the Al system

In this Section, the first results based on the Rappaz model with or without the use of the stochastic dynamics for the grain growth are presented. The empirical distribution functions were replaced by calculated homogeneous and heterogeneous nucleation rates provided by the MD simulations. In order to test the model, various cooling rates and contact angles were used. In the case where stochastic dynamics were used for the growth process, the variation of the diffusion coefficient with tempearture, calculated by the MD simulations, are presented.

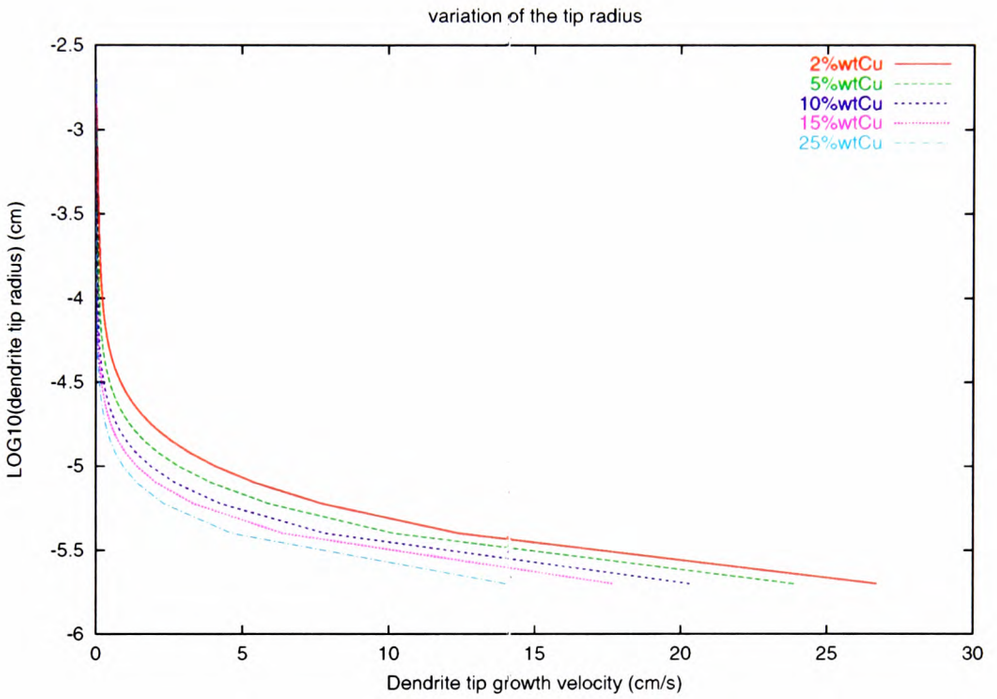

Figure 2.11: Variation of the dendrite tip radii with growth velocity for different solute concentrations for Ag-Cu alloys.

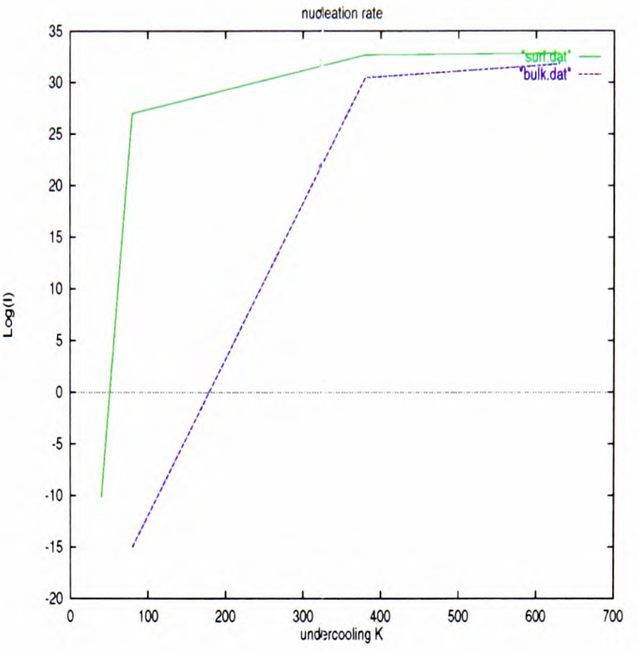

Figure 2.12: Values of the homogeneous and heterogeneous nucleation rates for Al, varying with undercooling.

As shown in Figure 2.12, the heterogeneous nucleation (90° contact angle is considered) rate necessitates a much lower undercooling than the homogeneous nucleation. The former is used for the nucleation on the mould's walls and the latter in the bulk liquid. As was the case for the Ag-Cu system, by decreasing the contact angle from 180° to 11.25° the critical undercooling was decreased from nearly 60°C to around 10°C as shown in Figure 2.13.

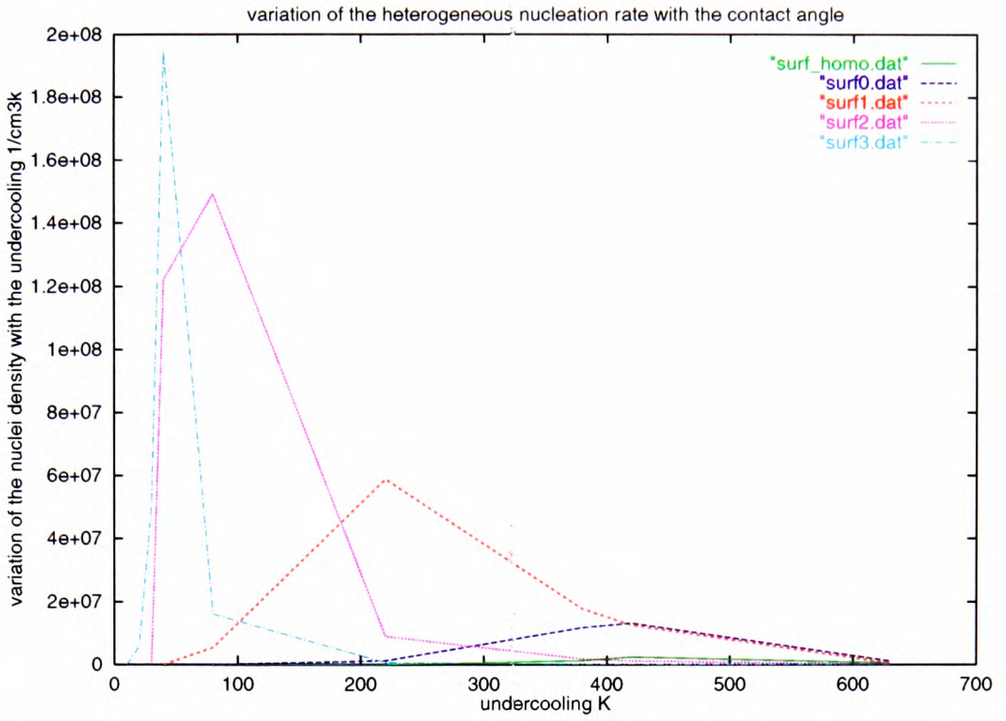

Figure 2.13: Variation of the heterogeneous nucleation rate with the undercooling for different contact angles, for the Al system

density

These nucleation rates were used to simulate nucleation on the surfaces with various roughness while simulating the formation of microstructure of solidification. The critical Gibbs energy also decreases, as expected, by a decrease in the contact angle from 30eV to near 2eV as shown in Figure 2.14.

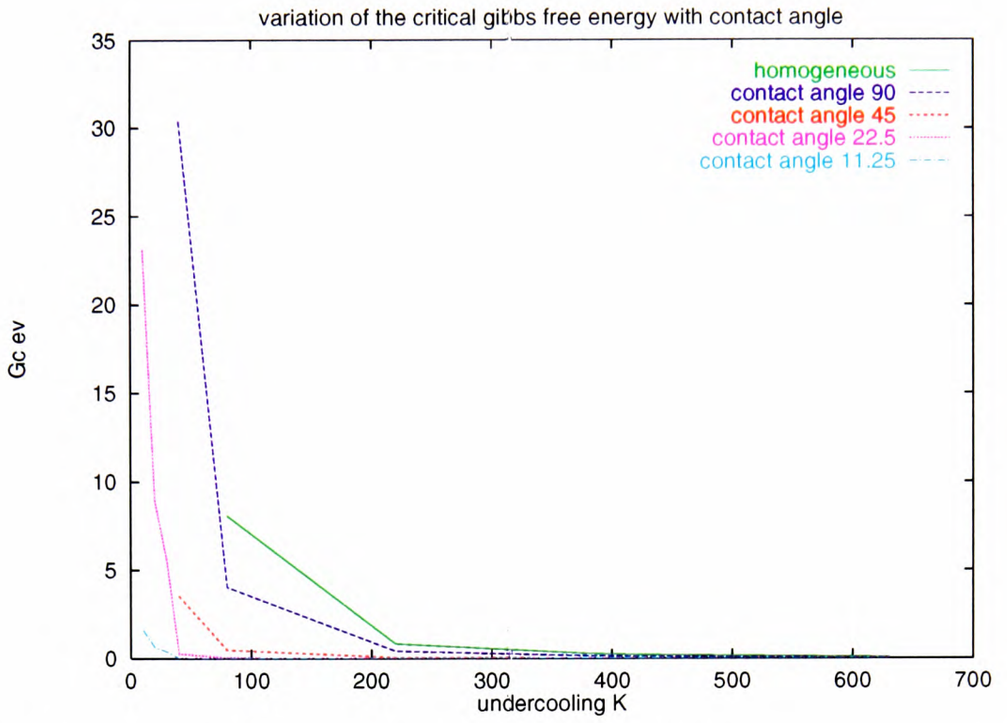

Figure 2.14: Variation of the critical Gibbs free energy with undercooling given a contact angle for the Al system.

2.6.4.1 A set of computational experiments for the validation of the Rappaz model

In this Section, the results related to a set of 16 different simulations, are presented. These simulations are aimed to test the ability of the model to reproduce microstructure of solidification based on different process parameters, in our case, the cooling rate and the surface roughness (use of various contact angles). Both the KGT model and the Ito stochastic dynamics are used. As shown in Table 2.1, contact angles take one of two values of 90° or 45°, the cooling rates vary between 2.5 and 10.5 K/s and the random velocity can be on or off based on the use of Ito stochastic dynamics in the growth model.

Table 2.1 (Al system)

Contact angle	Cooling rate K/s	random velocity	simulation number
90	2.5	on	1
90	4.5	on	2
90	6.5	on	3
90	10.5	on	4
45	2.5	on	5
45	4.5	on	6
45	6.5	on	7
45	10.5	on	8
90	2.5	off	9
90	4.5	off	10
90	6.5	off	11
90	10.5	off	12
45	2.5	off	13
45	4.5	off	14
45	6.5	off	15
45	10.5	off	16

The first simulated microstructure as shown in Figure 2.15 corresponds to a 90° contact angle, 2.5 K/s cooling rate and the Ito stochastic dynamics were used. In Figures 2.16 to 2.18 only the cooling rate was changed from 4.5 to 10.5 K/s respectively. By examining these Figures, the influence of the cooling rate on the microstructure can be understood. A higher cooling rate activates a greater number of nuclei at the same time and therefore the microstructure is more equiaxed than columnar.

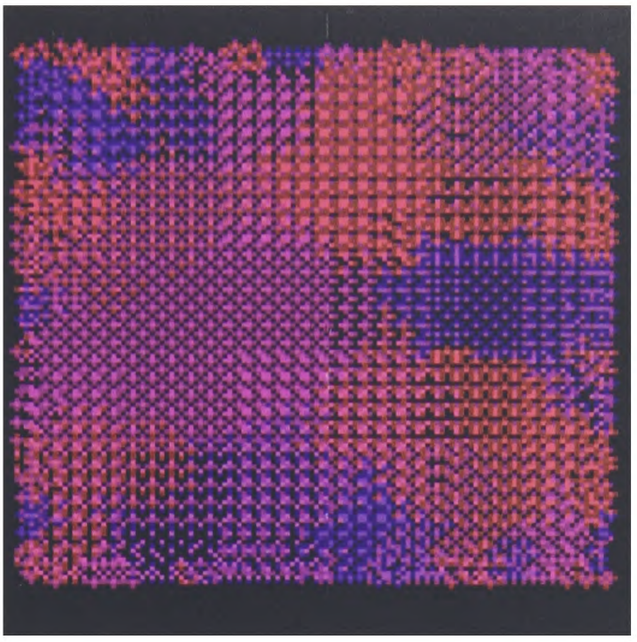

Figure 2.15: Microstructure of solidification, 90° contact angle, 2.5 K/s cooling rate and the Ito stochastic dynamics used.

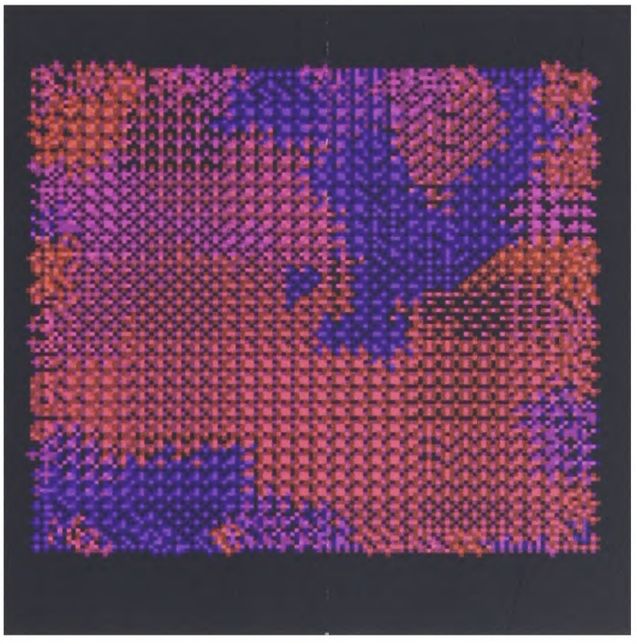

Figure 2.16: Microstructure of solidification, 90° contact angle, 4.5 K/s cooling rate and the Ito stochastic dynamics used.

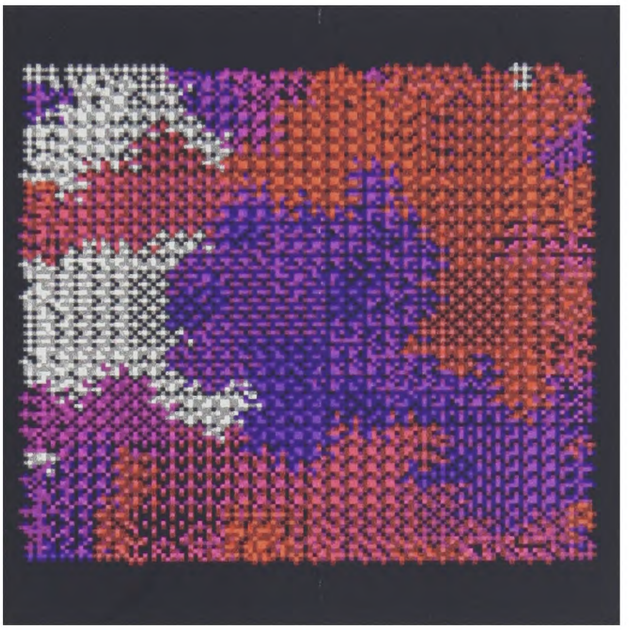

Figure 2.17: Microstructure of solidification, 90° contact angle, 6.5 K/s cooling rate and the Ito stochastic dynamics used.

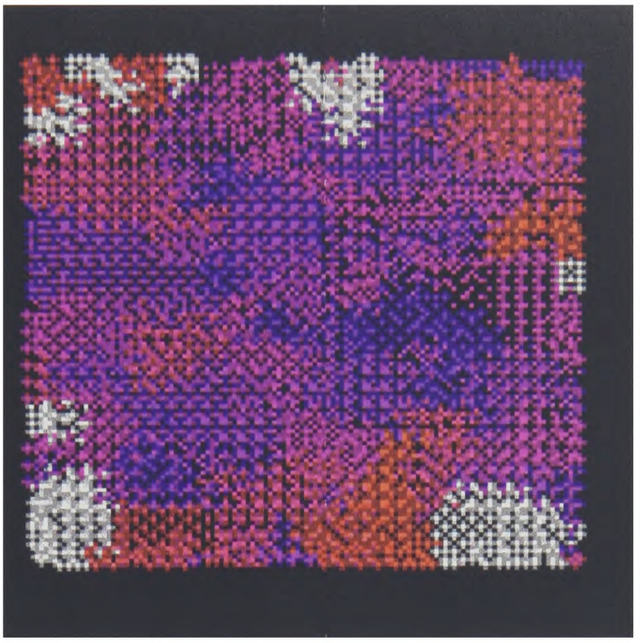

Figure 2.18: Microstructure of solidification, 90° contact angle, 10.5 K/s cooling rate and the Ito stochastic dynamics used.

The simulation number, 5 shown in Figure 2.19, is the same as simulation number 1 with the only difference that the contact angle is 45° instead of the 90°. In Figures 2.20 to 2.22, the cooling rate increased from 4.5 to 10.5 K/s. If we compare Figures 2.15 to 2.18 with Figures 2.19 to 2.22, it can be seen that for the same undercooling, a decrease in the contact angle produces higher proportions of the elongated (columnar-like) grains. The reason is in the decrease of the critical undercooling as shown in Figure 2.13. Therefore, the nucleation of grains begins at an earlier stages of the process, which means more growth time for already nucleated grains. Therefore, they can overtake other potential nucleation sites before they nucleate and to grow bigger and bigger.

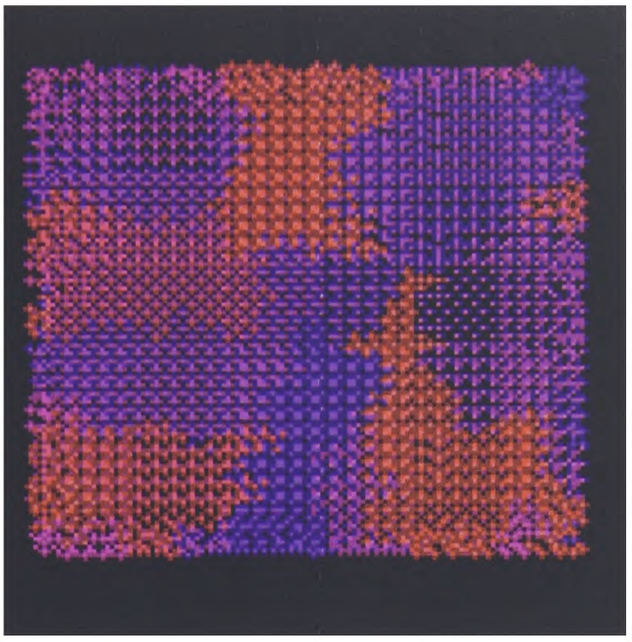

Figure 2.19: Microstructure of solidification, 45° contact angle, 2.5 K/s cooling rate and the Ito stochastic dynamics used.

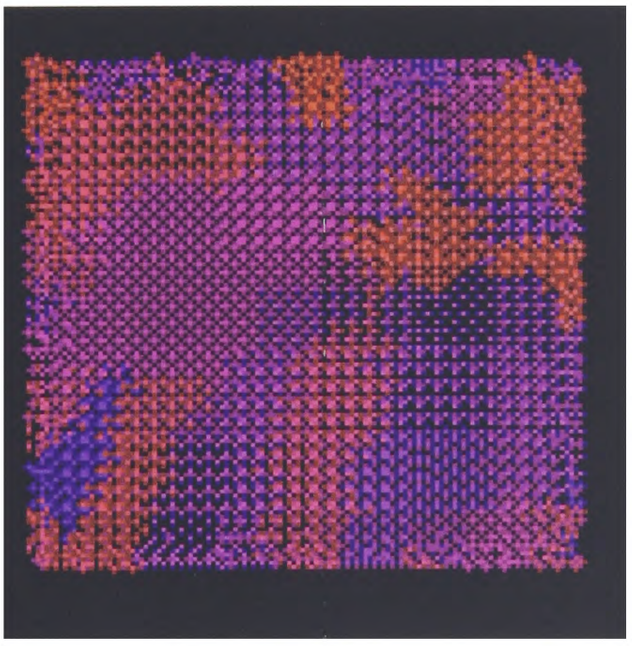

Figure 2.20: Microstructure of solidification, 45° contact angle, 4.5 K/s cooling rate and the Ito stochastic dynamics used.

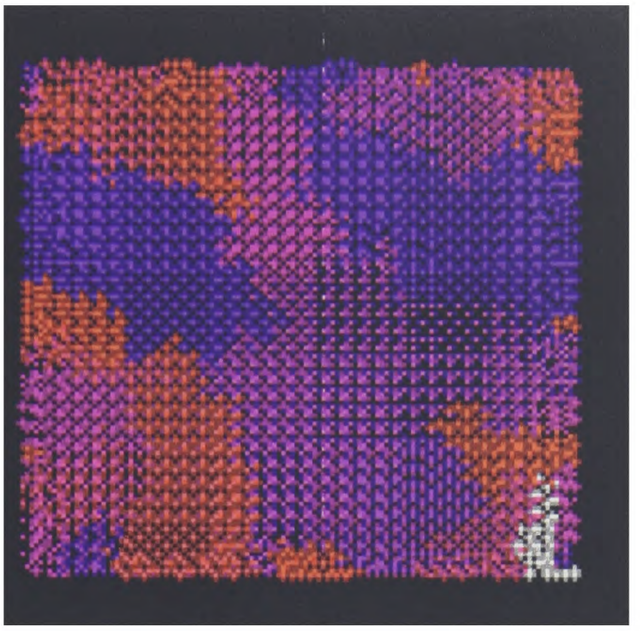

Figure 2.21: Microstructure of solidification, 45° contact angle, 6.5 K/s cooling rate and the Ito stochastic dynamics used.

The second part of these tests concerns the use of the Rappaz model without the Ito stochastic dynamics. The growth was calculated only by the KGT model and the diffusional noise was not considered. If we compare Figures 2.15 to 2.23, it can be seen that for the same cooling rate and contact angle, Figure 2.23 shows more equiaxed structure than Figure 2.15. The reason is in the model used for the growth. As in the case of Figure 2.15 the growth velocitry is higher than in the case of Figure 2.23 due to the addition of the stochastic velocity to the KGT drift velocity, the grains which nucleate at an earlier stage in the process can grow faster than those observed in Figure 2.23. By comparing Figures 2.24 to 2.30 to Figures 2.16 to 2.22, the same tendency of higher proportion of equiaxed structure can be observed. The columnar-to-equiaxed transitions can be observed quite clearly in Figures 2.18, 2.22, 2.26 and 2.30. The microstructures produced by our model can be compared qualitatively with those obtained by the Rappaz model [68]. Based on these comparisons, our model reproduces the correct tendencies of the microstructure formation based on changing process parameters, such as the cooling rate and growth velocity.

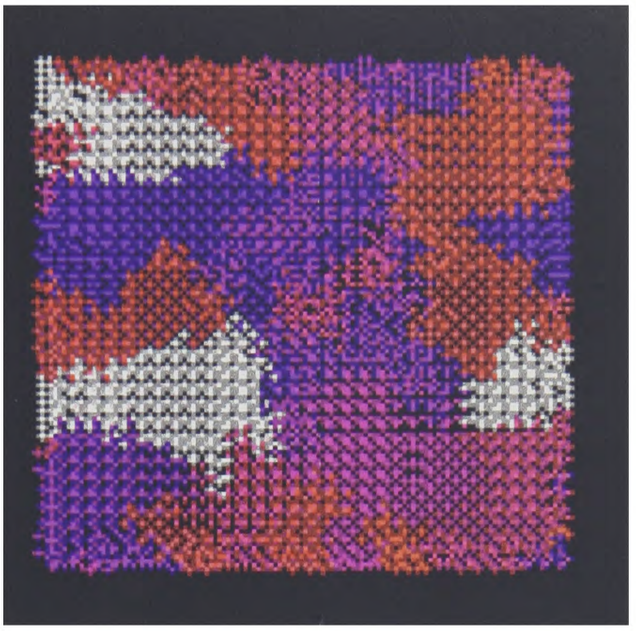

Figure 2.22: Microstructure of solidification, 45° contact angle, 10.5 K/s cooling rate and the Ito stochastic dynamics used.

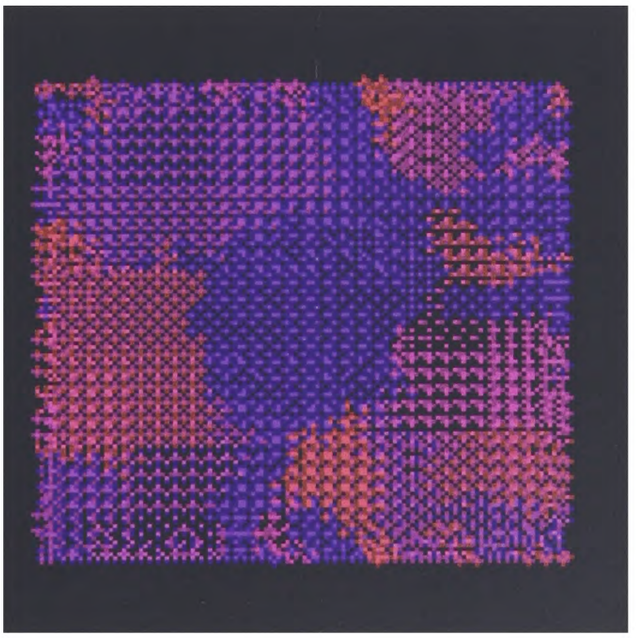

Figure 2.23: Microstructure of solidification, 90° contact angle, 2.5 K/s cooling rate and the Ito stochastic dynamics not used.

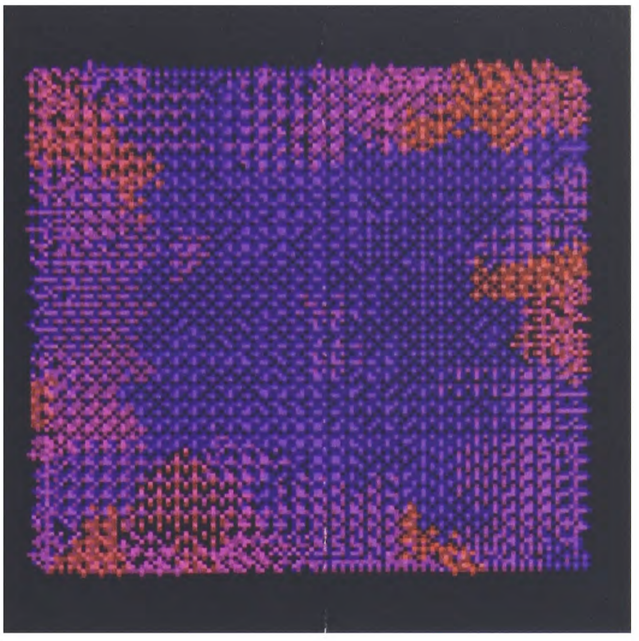

Figure 2.24: Microstructure of solidification, 90° contact angle, 4.5 K/s cooling rate and the Ito stochastic dynamics not used.

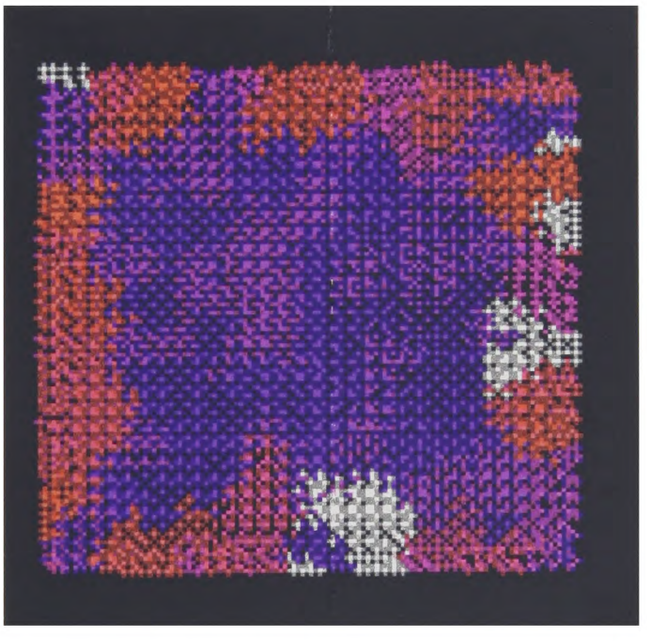

Figure 2.25: Microstructure of solidification, 90° contact angle, 6.5 K/s cooling rate and the Ito stochastic dynamics not used.

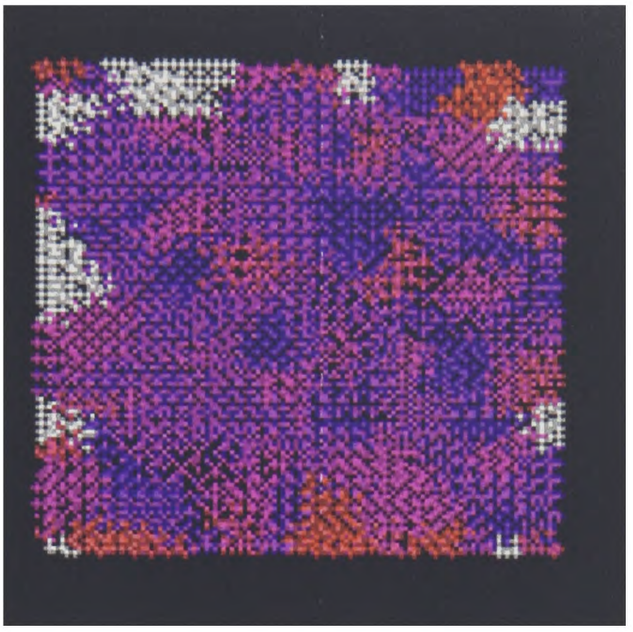

Figure 2.26: Microstructure of solidification, 90° contact angle, 10.5 K/s cooling rate and the Ito stochastic dynamics not used.

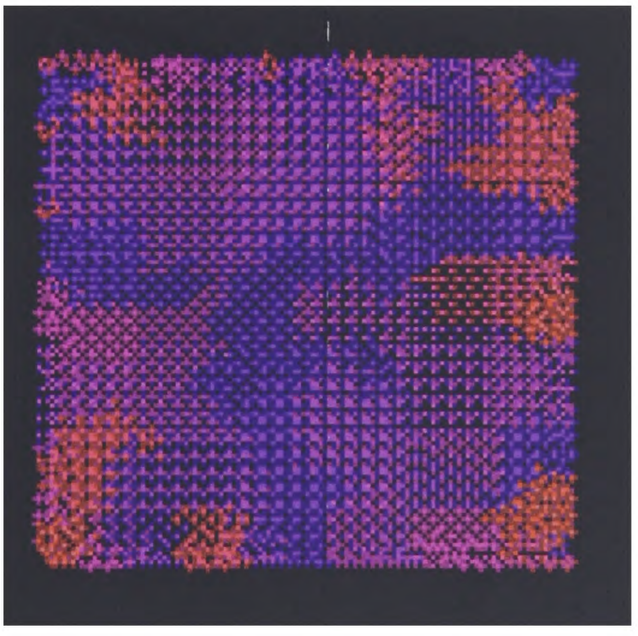

Figure 2.27: Microstructure of solidification, 45° contact angle, 2.5 K/s cooling rate and the Ito stochastic dynamics not used.

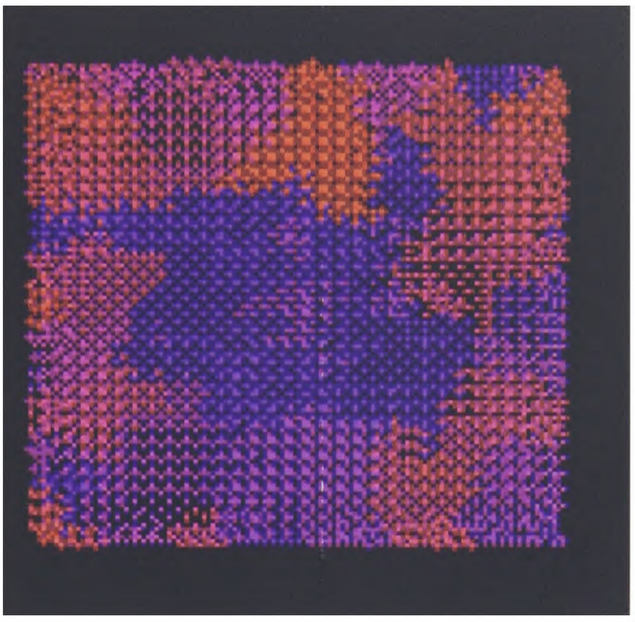

Figure 2.28: Microstructure of solidification, 45° contact angle, 4.5 K/s cooling rate and the Ito stochastic dynamics not used.

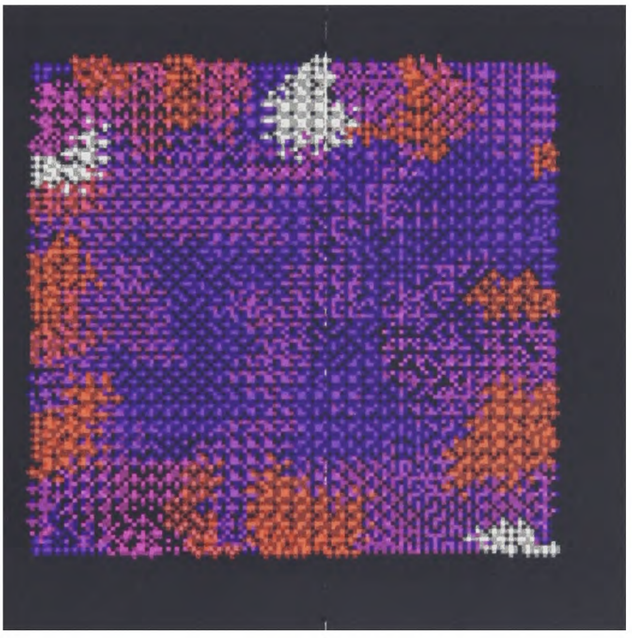

Figure 2.29: Microstructure of solidification, 45° contact angle, 6.5 K/s cooling rate and the Ito stochastic dynamics not used.

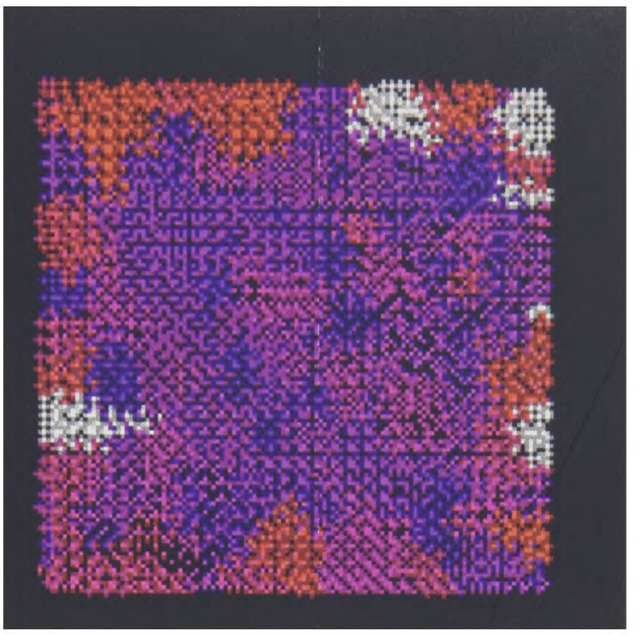

Figure 2.30: Microstructure of solidification, 45° contact angle, 10.5 K/s cooling rate and the Ito stochastic dynamics not used.

Maybe one of the most important aspects related to the change in the microstructure of a cast is that it influences the way by which the solidifying system releases its heat during the process. This aspect of heat release is crucial to the change in the solid fraction and therefore to the evaluation of the volume source in the enthalpy equation solved in the macroscale. As described in Chapter 3, the output of the micro model related to the variation of the solid fraction with temperature was used as input to the macro model used for the simulation of the heat and mass flow. By comparing Figures 2.32 and 2.31 it can be seen that the increase in the cooling rate will make the solidification more abrupt and the functional form of the solid fraction curve will approach a step function. On the other hand the use of the stochastic dynamics increases the growth velocity, therefore for the same cooling rate the solidification takes place more rapidly. Comparison between Figures 2.31 and 2.33 or Figures 2.32 and 2.34 shows the effect of the contact angle on the functional form of the solid fraction. As shown, for the same cooling rate the decrease in the contact angle produces an increase in the growth rate and therefore a less smooth solid fraction variation.

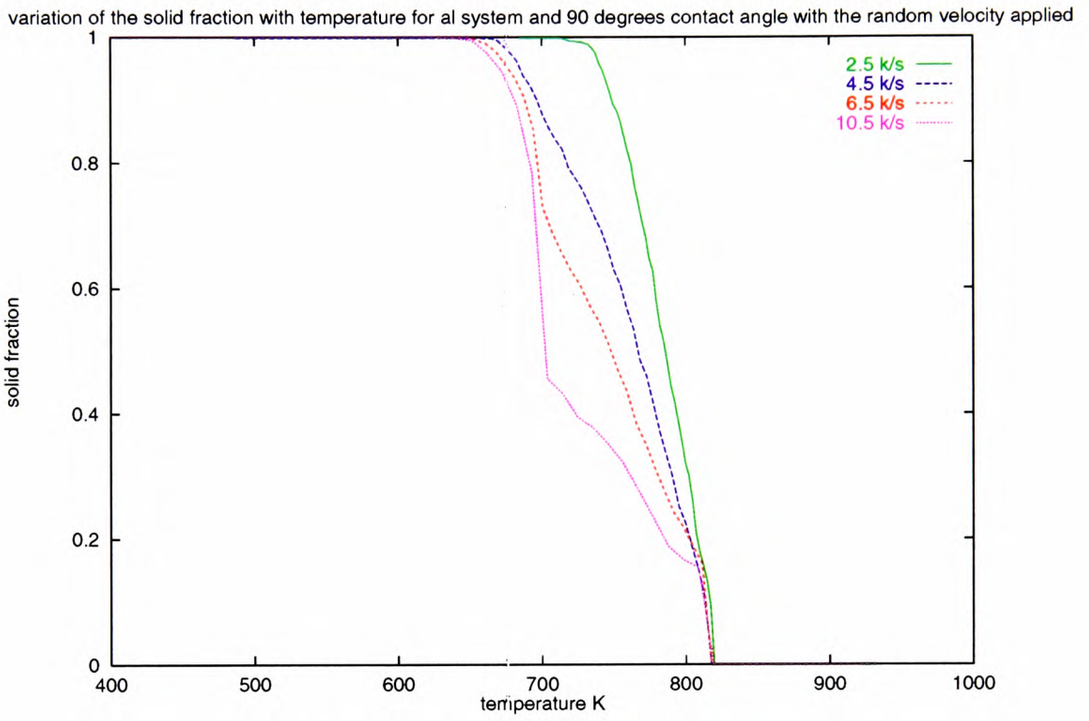

Figure 2.31: The variation of the solid fraction with temperature, 90° contact angle, stochastic dynamics is used, cooling rate is the varying parameter

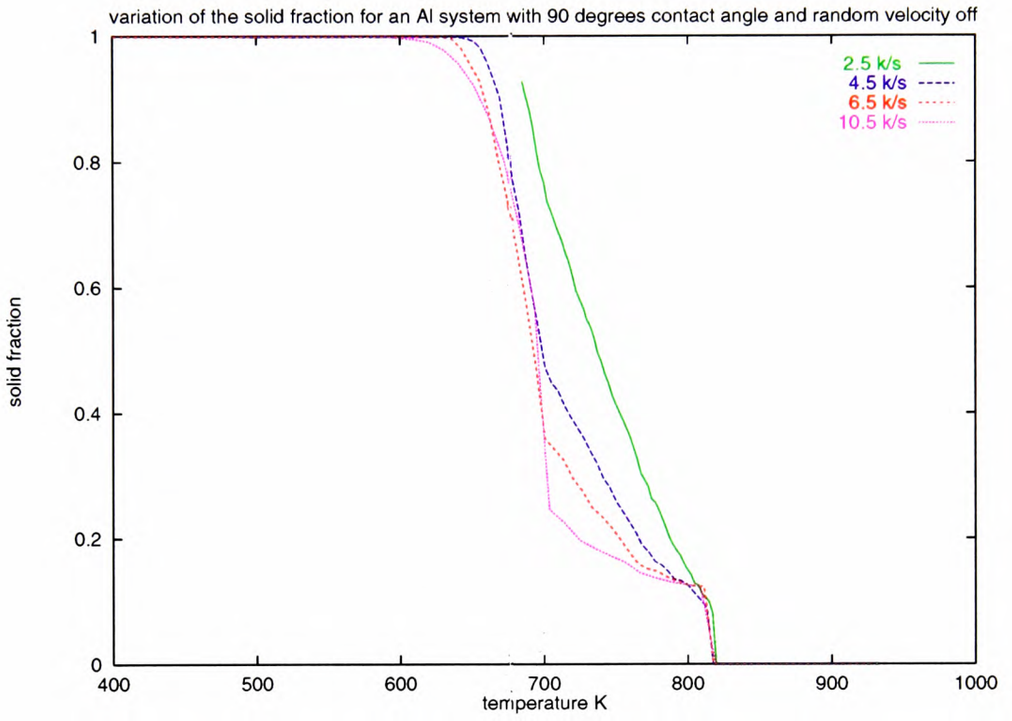

Figure 2.32: The variation of the solid fraction with temperature, 90° contact angle, stochastic dynamics is not used, cooling rate is the varying parameter

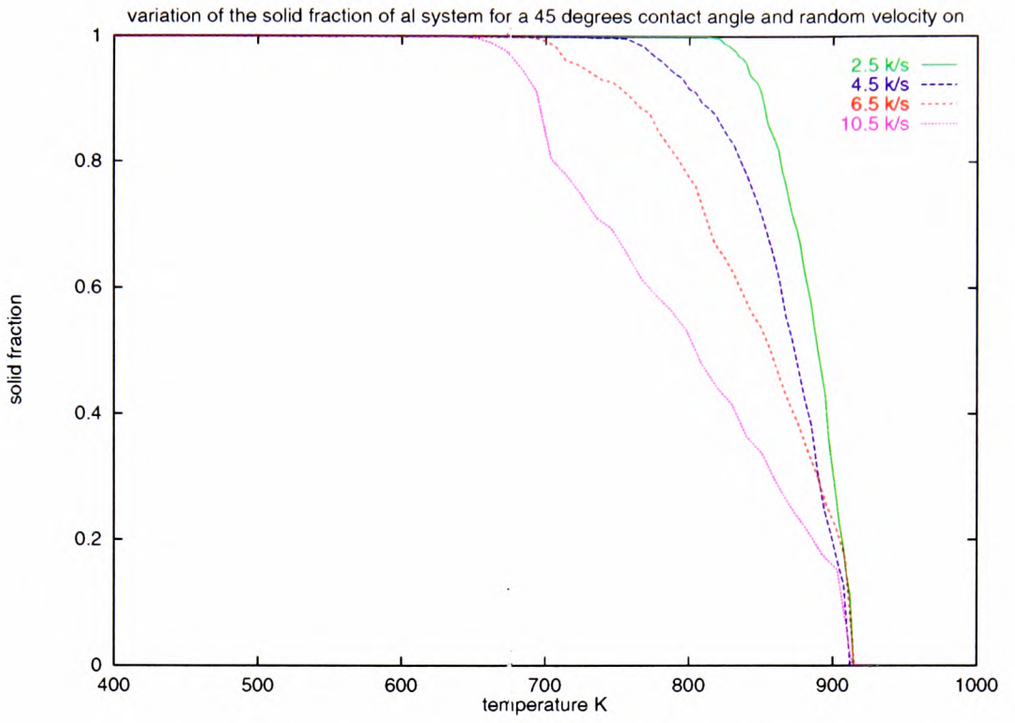

Figure 2.33: The variation of the solid fraction with temperature, 45° contact angle, stochastic dynamics is used, cooling rate is the varying parameter

By using the micro model as a preprocessor (the program is run before the macro program is executed) to the macro model, the correct variation of the source term can be incorporated within the macro simulatiom model to be described in Chapter 3.

2.6.5 Results for the Al-3%atSn alloy

Aluminium-based alloys play an important role in the automotive and airspace industry, and in contrast to the pure aluminium, which is soft, its alloys can be quite hard and tough and suitable for industrial applications. The reason, as described and observed in this Section, is the formation of an equiaxed region within the alloy which contributes to fortify the structure by opposing the movement of defects within the crystalline structure. The homogeneous and heterogeneous nucleation rates, based on the values of the residual chemical potential obtained by the MD simulations, are given in Figure 2.35. The heterogeneous nucleation has a greater value than that of the homogeneous due to the smaller value of the contact angle

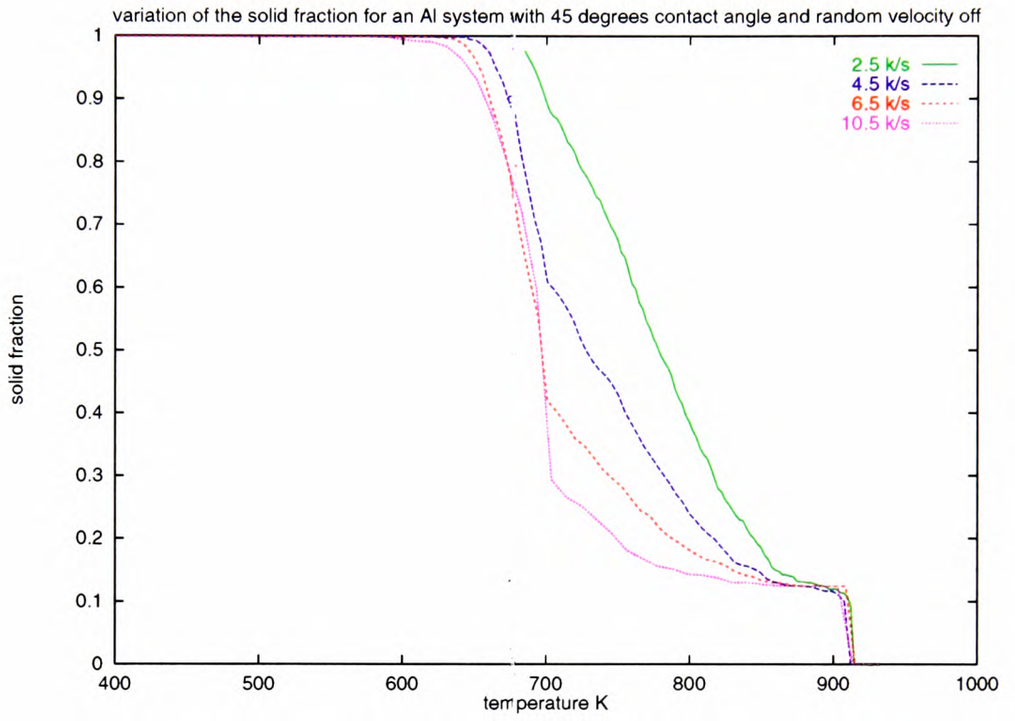

Figure 2.34: The variation of the solid fraction with temperature, 45° contact angle, stochastic dynamics is not used, cooling rate is the varying parameter

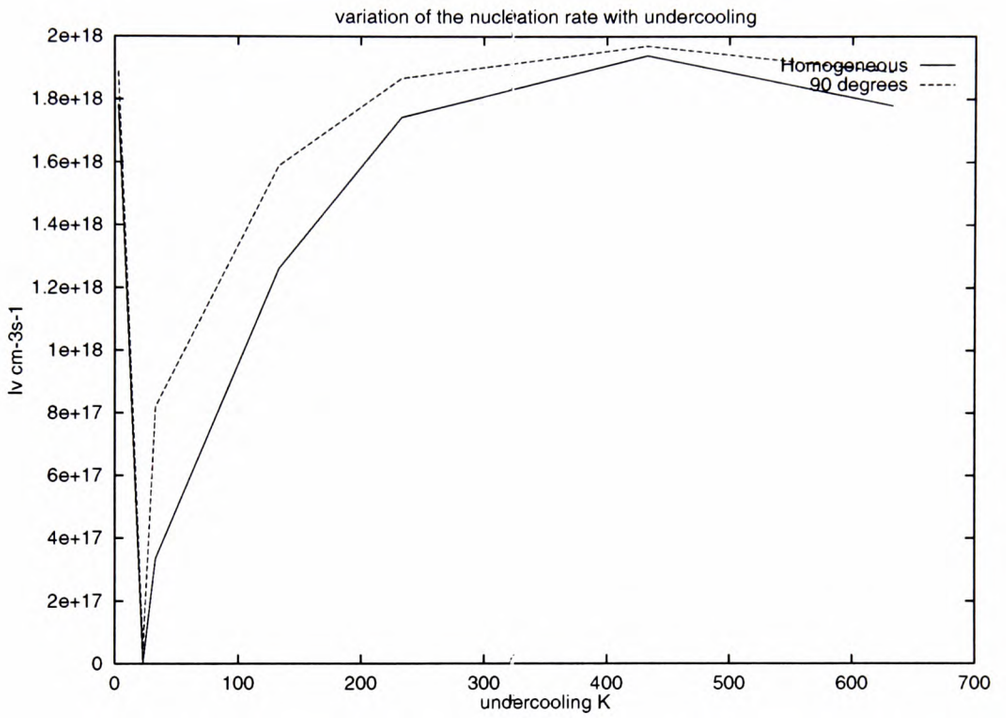

Figure 2.35: Variation of the nucleation rate with temperature and contact angle for Al-3%atSn alloy

(90° contact angle is considered). These values are used to generate the microstructures given in Figure 2.37 in which the pure aluminum is compared to the Al-3%atSn. The diffusion coefficient calculated directly by the MD simulations is also given in Figure 2.36. This value is used within the random part of the Ito stochastic dynamics. A jump (discontinuity) in the value of the diffusion coefficient near the melting point, can also be observed in Figure 2.36. The effect of the addition of the solute can be observed in figure 2.37 and compared to

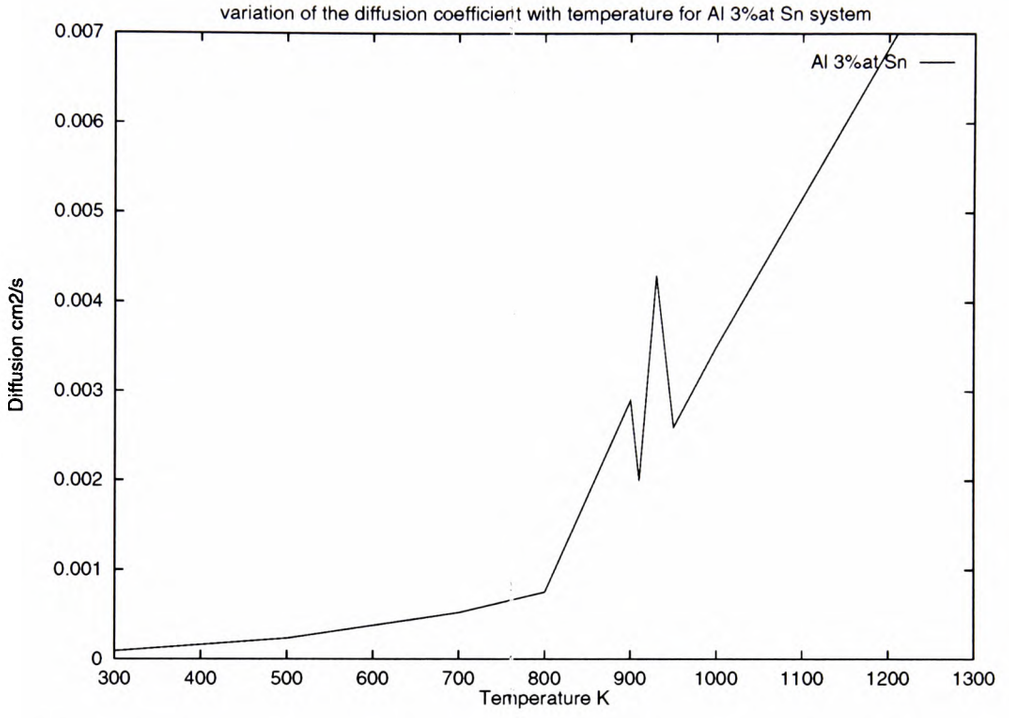

Figure 2.36: Diffusion coefficient for the Al-3%atSn alloy, using MD simulations

experimental results in [57]. The addition of 3%atSn changed the microstructure from a simple columnar to a columnar and inner equiaxed microstructure. The reason is the constitutional undercooling which lowers the local freezing temperature and allows more nucleation sites of different crystallographic orientation to nucleate at the same time and therefore to produce an equiaxed structure and to stop columnar growth. These equiaxed structures have a great influence on the thoughening effects of solute addition within the aluminium alloys. More and smaller grains make it difficult for defects to move arround the structure.

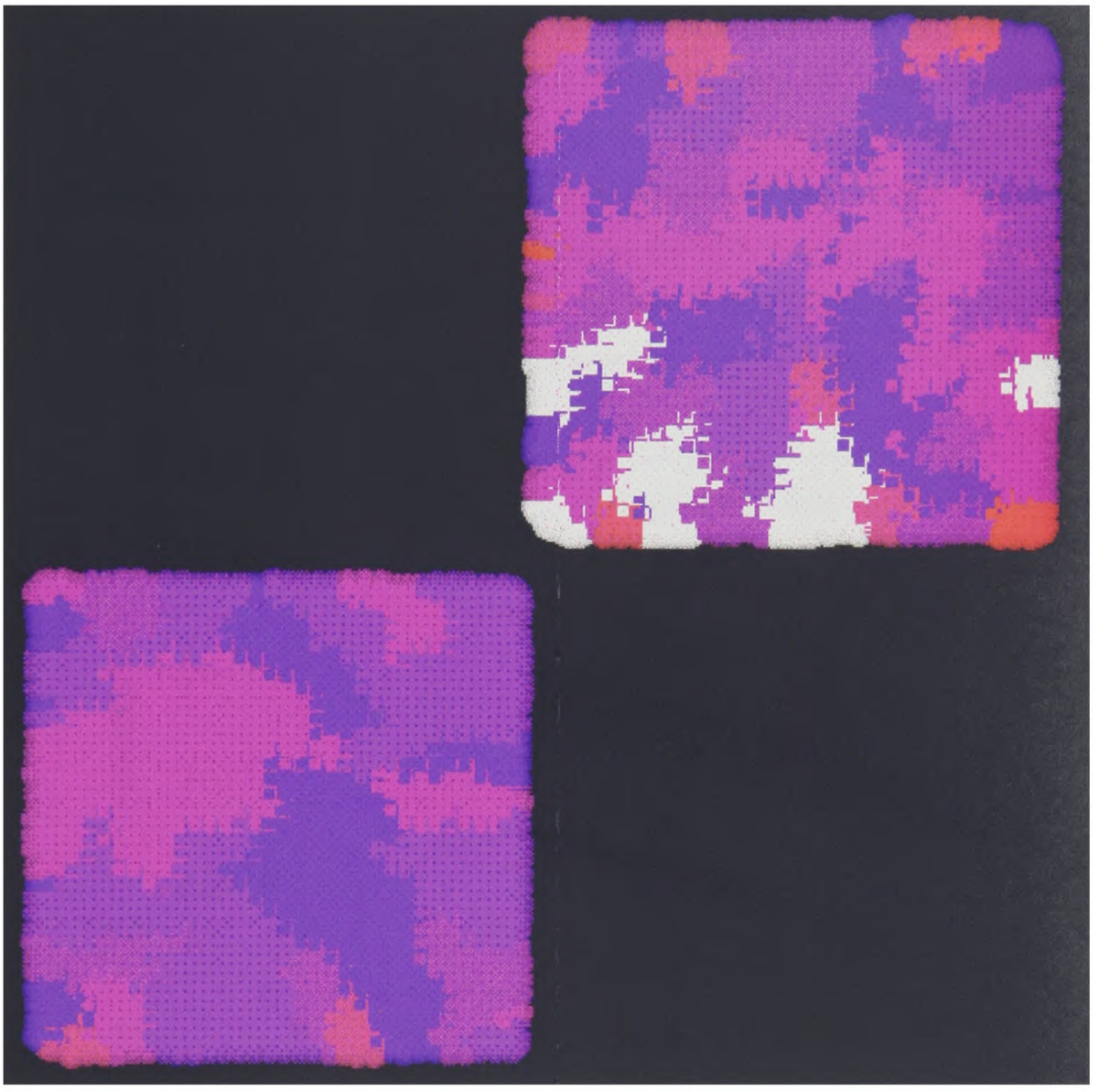

Figure 2.37: Comparison between the Al and Al-3%atSn microstructures: top-right, Al-3%atSn microstructure for 1K/s cooling rate and 90° contact angle, bottom-left, Al pure microstructure for the 1K/s cooling rate and 90° contact angle.

2.6.6 Results for Sn 10%wtPb

The last case studied in this Section is the case of the Sn-10%wtPb alloys. These alloys (more precisely a eutectic composition) are mainly used in the electronic packaging industry as solder materials. The knowledge of the microstructure is important in order to evaluate the mechanical properties of the alloy especially the level of the internal stress. Four simulations were conducted, based on the results obtained by the MD simulations. Two different values of the cooling rate and two sets of contact angles were used and their relative microstructures compared. The value of the nucleation rate, based on the MD, is given in Figure 2.38 and the diffusion coefficient is given in Figure 2.39. As in the case of Al-3%atSn, a discontinuity can be observed in the value of the diffusion coefficient near the melting point. The microstructures

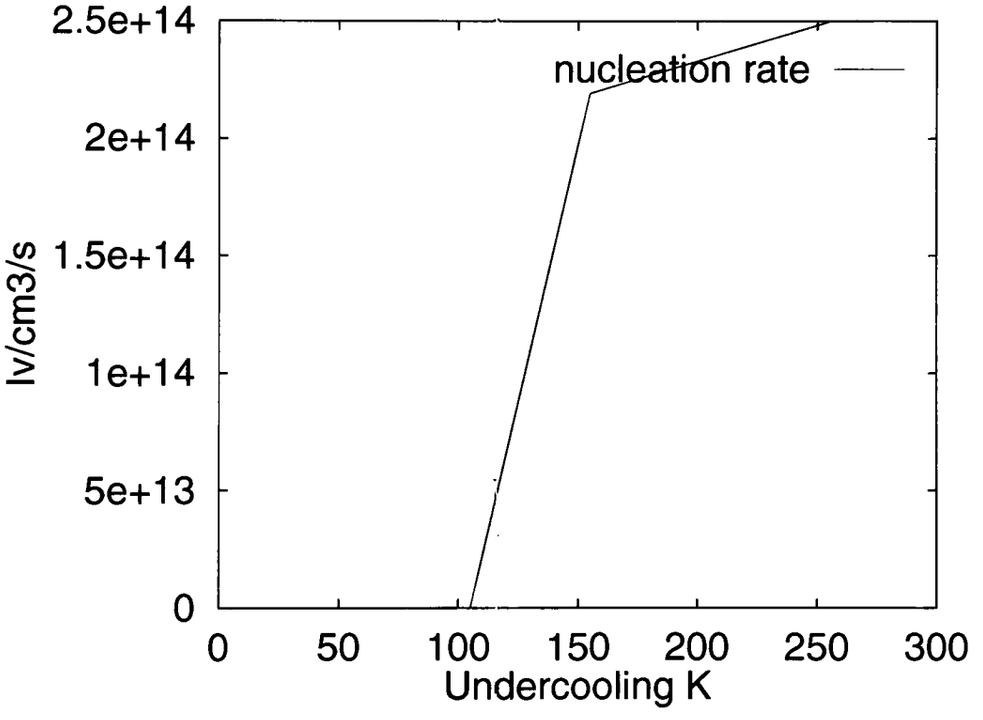

Figure 2.38: Variation of the nucleation rate with undercooling for the Sn-10%wtPb obtained by MD simulations.

based on the MD output are given in the Figure 2.40. By comparing Figures 2.40 a and b, as the cooling rate was increased from 6K/s to 10K/s respectively, the equiaxed microstructure was formed for the latter case. In the case that the cooling rate is kept constant and the

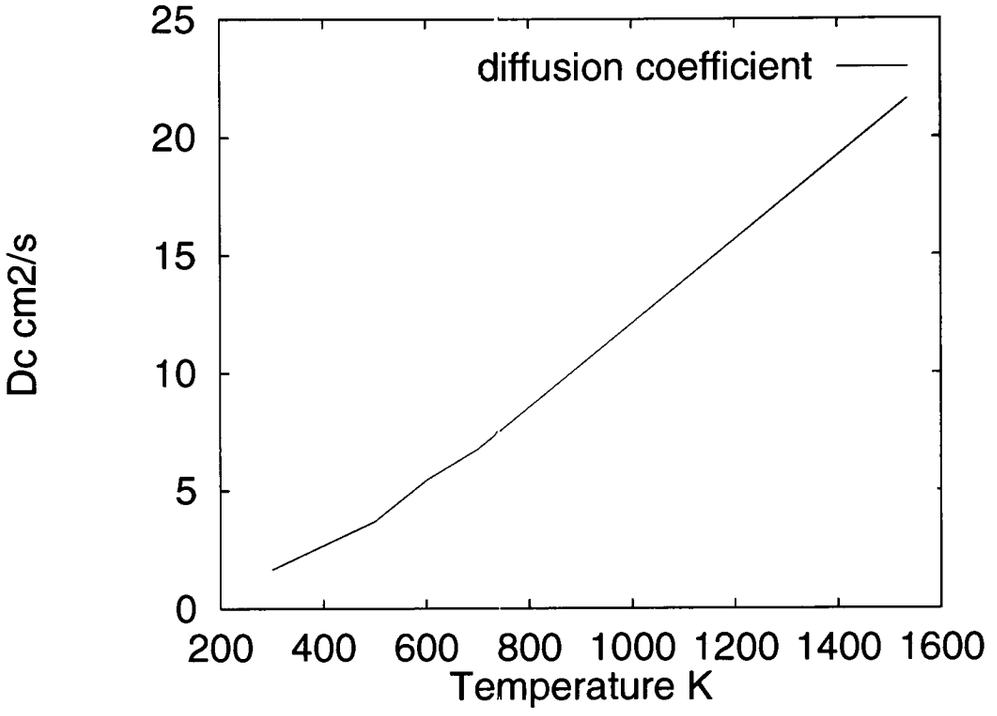

Figure 2.39: Variation of the diffusion coefficient for Sn 10%wtPb alloy using the MD simulations.

contact angle increases, the amount of the equiaxed will be increased as shown in Figures 2.40(c) and (d) in comparison to the Figures 2.40(a) and (b). The variation of the liquid fraction with temperature, which is used in the Chapter 3, is given in the Figure 2.41. As shown in this figure, by increasing the cooling rate the functional form of the liquid fraction approaches the step function as was the case in Figures 2.31 and 2.33.

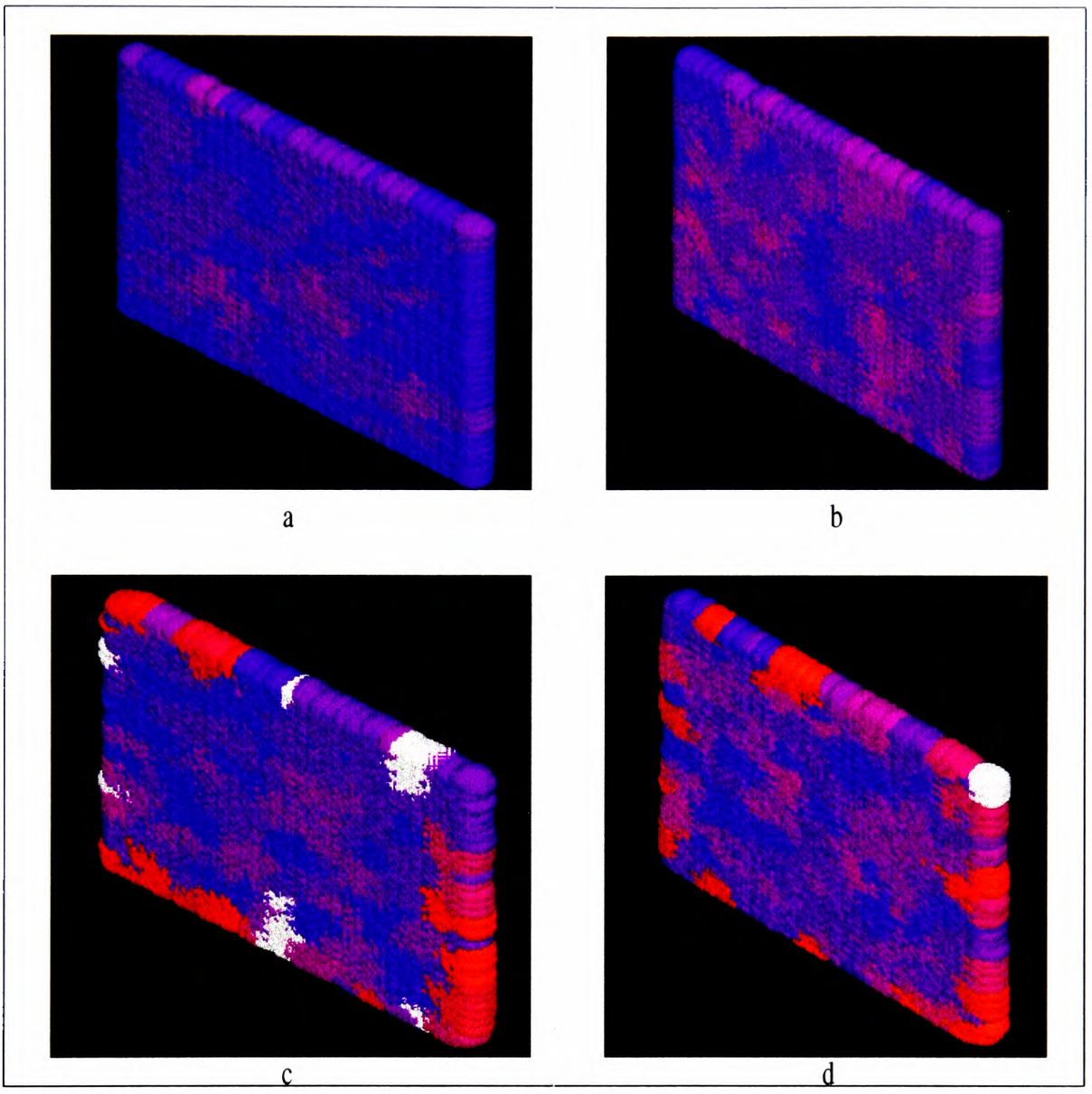

Figure 2.40: Variation of the microstructure with the cooling rate and contact angle: a) 6K/s cooling rate and 45° contact angle, b) 10K/s cooling rate and 45° contact angle, c) 6K/s cooling rate and 90° contact angle, d) 10K/s cooling rate and 90° contact angle.

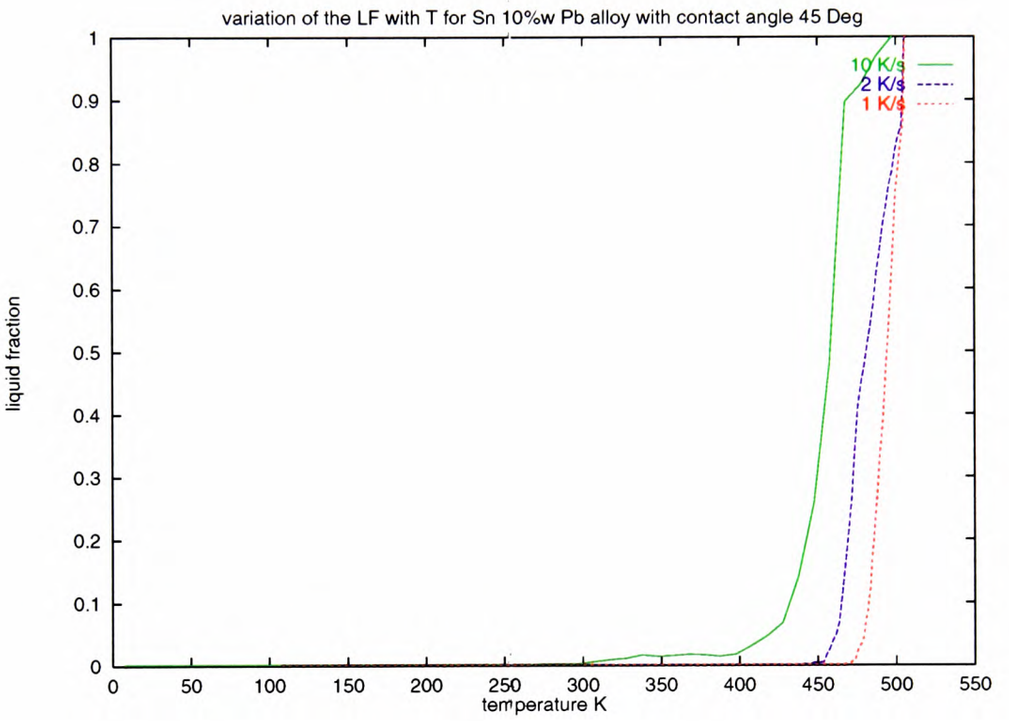

Figure 2.41: Liquid fraction variation with cooling rate for a contact angle of 45deg, Sn 10%wtPb system

2.6.7 Discussions and conclusion

In this Chapter, the three following aspects were investigated

- Variation of the heterogeneous and homogeneous nucleation rates based on the cooling rate, contact angle and solute concentration.
- Behavior of the CA model with and without the Ito stochastic dynamics for different cooling rtaes and contact angles.
- Behavior of the KGT model [57] for different solute concentrations.

By comparing Figures 2.15 to 2.30 with the CA results obtained by Rappaz [68], the following points can be observed

- An increase in the value of the cooling rate increases the surface area of the inner equiaxed zone due to the simultaneous activation of a greater number of nucleation sites.
- A decrease in the value of the contact angle (Rappaz decreases artificially the surface undercooling of the fitted Gaussian), corresponding to an increased surface roughness or bulk impurity, increases the surface area of the columnar zone due to the extinction of potential nucleation sites by the growth of already nucleated grains.
- The columnar-to-equiaxed transition zone and its evolution are modelled correctly.
- The $< 100 >$ preferential growth directions are modelled properly in accordance with the heat flow direction.

We can therefore consider that the Rappaz model was implemented correctly in our multiscale model and that it qualitatively produces the same tendencies as the original Rappaz model.

By considering the same set of Figures 2.15 to 2.30, the effect of the introduction of the Ito stochastic dynamics into the dendrite growth mechanism can be observed. For the same cooling rate and contact angle, models using the Ito stochastic dynamics produce more columnar structure than those not using it due to an increase in the dendrite tip growth velocity by diffusional noise.

The variation of the homogeneous and heterogeneous (contact angle smaller than 180°) nucleation rates with the undercooling, based on a given value of cooling rate, contact angle and solute concentration as observed in Figures 2.5, 2.6, 2.35 and 2.38 can be summarized as follows

- The decrease in the contact angle will decrease the critical undercooling.
- An increase in the cooling rate will increase the nucleation rate and grain density.
- An increase in the solute concentration will increase the nucleation rate.

Therefore, the variation of the nucleation rate evaluated via the atomistic modelling is in agreement with theoretical expectations [5].

By considering Figures 2.10 and 2.11, for an increasing solute concentration there is a decrease in the growth velocity and also in the critical radius in agreement with the KGT model [57], therefore, the KGT model was implemented correctly. The effect of the solute on aluminium, simulated by the nano-micro model, is given in Figure 2.37 and compared to experiment [50]. As shown in the Figure and the experiemnt, the addition of the solute increased the equiaxed region surface area.

The atomistic modelling could therefore improve the Rappaz model by

- Evaluating the correct nucleation rate based on the local undercooling, calculated via the change in the residual chemical potential of the system, for a given undercooling, alloy composition and surface rugosity. No more empirical considerations (no more fitted empirical function to experimental observation) for the nucleation of the grains and consideration for the surface rugosity (an angular factor is used for surface nucleation), impossible in the Rappaz model.
- The additional contribution of the diffusional noise of the dendrite tip is taken into considration, changing the local growth velocity of the dendrite tip based on the atomistic calculation of the diffusion coefficient.

As a conclusion to this Chapter, the following points can be deduced as a confirmation of the microstructure formation theory regarding the cooling rate, contact angle and solute concentration based on the nano-micro model output:

- By increasing the contact angle (in opposition to the Rappaz model, the contact angle can be explicitely incorporated into the program) which means by increasing the rugosity of the surface of the mould, we can decrease the critical undercooling for the surface distribution, therefore an early creation of columnar grains which decreases our chance of having an equiaxed zone.

- By increasing the cooling rate we can reach much more quickly the critical undercooling in the bulk and on the surface at the same time, therefore we can observe a higher concentration of equiaxed zone.

- When using the random velocity, as the growth velocity is higher than the case without difussional noise, for the same cooling rate and contact angle we observe much higher concentration of the columnar zone in comparison to the equiaxed zone.

- For low cooling rates, as we have mainly the columnar zone, only the grains with their prefrential growth direction near to the x axis can survive (x axis is supposed to be the heat flow direction) but when cooling rate is high other directions have also the chance to develop and to survive.

- The addition or increase in solute concentration (figure 2.37) will decrease the local solidification (freezing) temperature which will in turn increase the nucleation sites density in the bulk and on the surface, leading to agreater number of grains with different orientations to compete for growth and therefore a more refined structure due to a higher concentration of equiaxed zone. This can be confirmed by comparing Figure 2.37 with experimental results given in [57].

Chapter 3

The coupled nano-micro-macro model

3.1 introduction

The effects of heat transfer and fluid motion during the casting of alloys have been investigated in great detail for more than fifty years. These studies allow design engineers to determine the influence of process parameters on the formation of macro defects, such as macrosegregations, voids formations, macroshrinkage and hot spots [90]. The process parameters include the cooling rate, the pouring temperature, the position of the chill and the feeder, the type of the casting used (die, sand, permanent mould, etc) and the pouring velocity [90]. A large number of commercial computer codes have been developed during the last two decades to provide the capability to model the casting process on the computer avoiding costly experiments. Some of these tools (e.g. Procast [1] and Magmasoft [2]) can accurately predict the thermal profile, hence macro defects such as hot spots can be avoided.

Unfortunately, these models do not provide predictions of the casting final microstructure. The microstructure, as mentioned in Chapter 2, influences some of the most important mechanical properties in metallic systems such as the hardness, ductility, total elongation, fatigue life and crack formation [91]. Additionally, the macroscopic models can only accurately simulate the heat and fluid flow if

[1] UES Software Inc., Dayton, Ohio, USA
[2] MAGMA Gmbh, 52072 Aachen, Germany

- An extensive and accurate database on the temperature-dependent thermo-physical properties under study was available.

- The volume and surface sources, used in the definitions of heat and fluid flow conservation equations [92], are accurately known.

Unfortunately for a great number of industrial alloys, these two conditions are not satisfied, and therefore predictions are not reliable. Experimental measurements of these values are costly, hence modelling provides a possible alternative.

A remedy for these short-comings was a full multiscale study of the solidification phenomena, beginning at the atomistic clusterisation level, up to the macroscopic segregation level in order to cover the whole range of length, time and energy scales involved in the casting process. The major problem in implementing this kind of strategy was the mechanism by which these various scales have to be linked together and the way information flows from one scale to another.

The methodolgy proposed in this Thesis was based on a *parametric study* of different scales involved in the overall process, beginning with the nanoscopic clusterisation, continuing with the microstructure formation and culminating with the macroscale solidification. The nanoscale approach to solidification, the methods used to evaluate the material properties and the detection of the phase transition based on the positions and velocities of individual atoms in the metallic system, has been described in detail in Chapter 1. The microscale modelling, based on nucleation and growth of dendritic structures and the linkage between the nano and micro scales, to produce a *modified Rappaz model of microscale formation*, has been discussed in Chapter 2. In the present Chapter, a description of the macro model used, and the linkage between the *nano-micro model* and the *macro model* was presented. The full implementation of the coupled *nano-micro-macro* model was applied to two industrially important alloys, the Sn-Pb and Al-Sn systems. The micro model was also used as a post processor (the micro model was used to process the temperature field produced by the macro model in order to generate the localised microstructure) for the Al-Ni system.

3.2 Description of the macro model

The macro model used consists of a code developed at the University of Greenwich, named *Physica*. Physica was a multi-physics and modular software which solves at the same time for computational fluid dynamics (CFD) and for computational solid mechanics (CSM) and also for the interactions between these two. The discretisation method for CFD was a cell centred finite volume method (Figure 3.2) [93] and for CSM, a vertex based finite volume method (Figure 3.2) [94]. Both structured and unstructured, orthogonal or non-orthogonal meshes (Figure 3.1) can be used [95] which gives the programme the flexibility necessary to handle complex geometries.

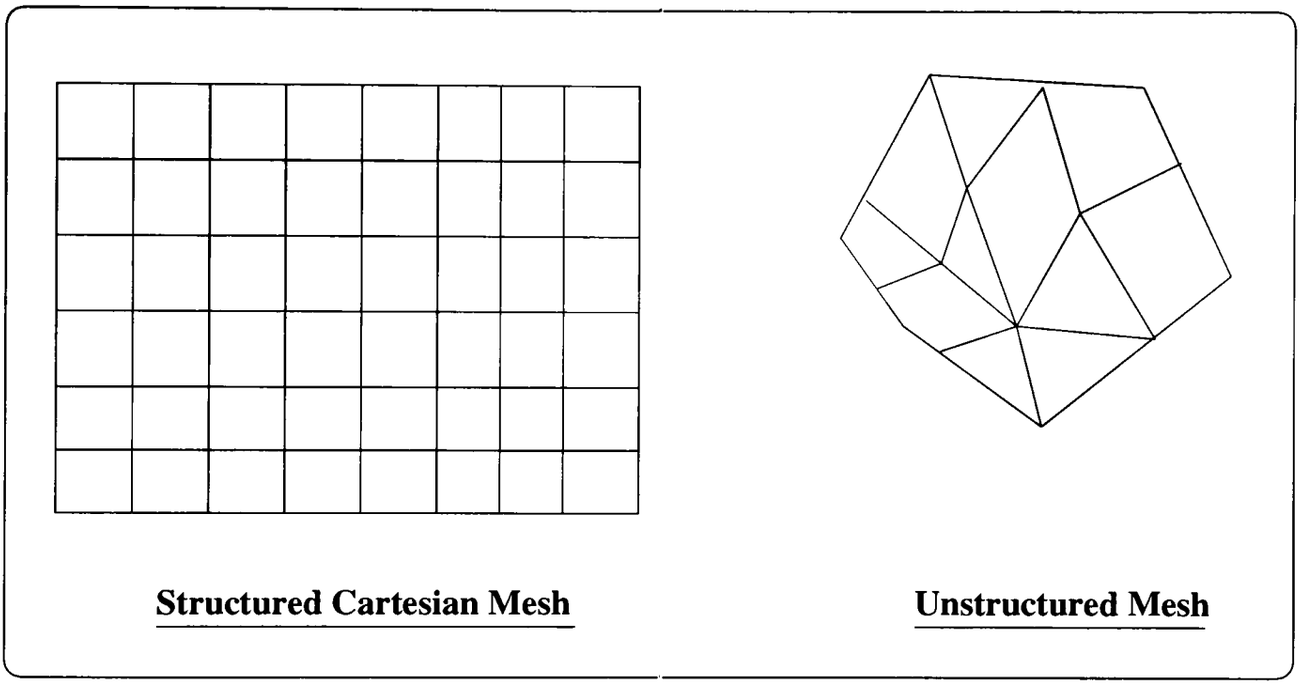

Figure 3.1: Structured and unstructured meshes used in Physica

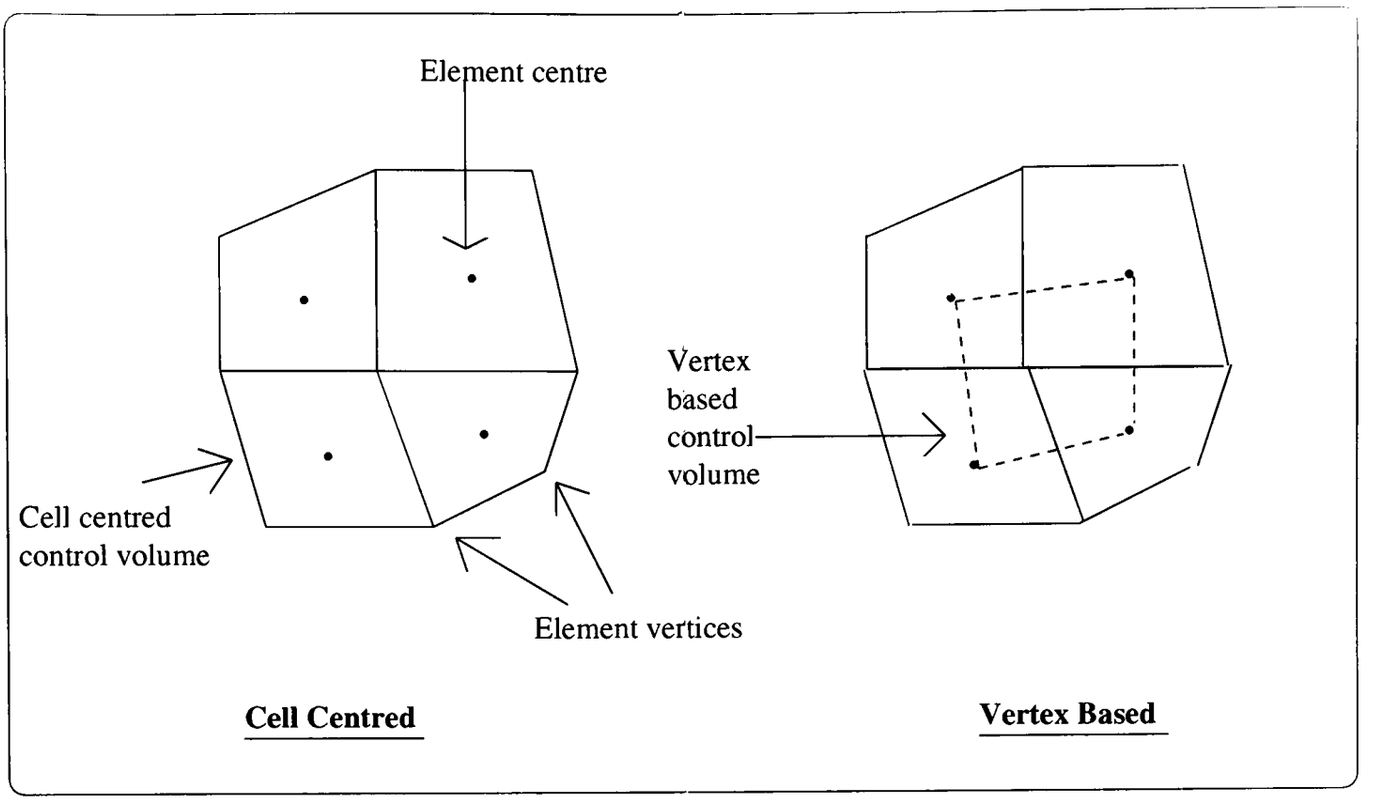

Figure 3.2: Cell centred and vertex based finite volume methods

3.2.1 Structure of Physica

Physica is a modular software package. A module template is used to create different modules. Each module has its own source code and the module is listed within a module directory and a unique name is associated to it. One of the modules provided by Physica is the *USER* module which allows a user to implement his/her own codes and subroutines within the Physica software in order to customise the code. The user module can be used for example to calculate material properties, based on external databases or programmes, or to supply user-defined analytical functions, for different temperature-dependent variables, used in various modules of Physica software.

Physica relies on two main files to run, as described below

- The "inform" file, which:
  - defines the type of the problem to be solved by providing the name of the modules in the module directory that must be used for the specified problem.
  - values of different material properties used in the specified modules.
  - the name of the geometry file created for the problem under study.
  - definition of the initial and boundary conditions imposed on the system.
  - values of the surface and volume sources used in different conservation equations.
  - time steping format and values, tolerance of residual values for iterative processes and the choice of integration method used.
  - the method of visualisation of the results produced by the programme.
- The geometry file which defines:
  - number of nodes, faces, elements and patches associated to them.
  - element connectivities and interfaces.

Once these files are setup properly and the Physica kernel compiled for the specified platform on which it must run, the programme can be executed. The geometry file is produced by

FEMGV software which is a pre and post processing toolkit. As a preprocessor it generates the geometry and the mesh which can then be used as input to Physica and as the postprocessor can analyse the Physica's output regarding the temperature, velocity, stress and fraction solid fields. Therefore, the results produced by physica are also visualised by this software.

3.2.2 Heat transfer and solidification modelling in Physica

This thesis utilises the heat transfer and solidification modules, hence they are described below. The conservation of energy is expressed as a function of enthalpy or temperature, eqn. (3.1), [97]

$$\begin{aligned}
&\frac{\partial(\rho C_p T)}{\partial t} + \nabla \bullet (\rho C_p \upsilon T) = \nabla \bullet (k_t \nabla (T)) + S_t, \\
&\text{when we solve for temperature, or} \\
&\frac{\partial(\rho h)}{\partial t} + \nabla \bullet (\rho \upsilon h) = \nabla \bullet \left(\frac{k_t}{C_p} \nabla (h)\right) + S_t, \\
&\text{when we solve for enthalpy}
\end{aligned} \tag{3.1}$$

The source term is defined as:

$$-L\left(\frac{\partial(\rho f)}{\partial t} + \nabla \bullet (\rho \upsilon f)\right). \tag{3.2}$$

In eqn. (3.1) ρ is the density, C_p is the isobaric specific heat, k_t is the thermal conductivity, υ is the flow velocity, T is the temperature, h is the enthalpy, t is the time, L is the latent heat and f is the liquid fraction. As given by eqn. (3.2), the solidification effect due to the change in the liquid fraction is based on a scalar value (this scalar value is either given by a step-like function or a linear function based on a given temperature) which is updated at each time step using a source based algorithm [94, 96, 97].

In this Thesis, the temperature is solved and the source term contained both the thermal conductive and convective effects of the heat transfer.

3.3 Linking the nano, micro and macro models

In order to describe the model two aspects of the linkage must be considered.

- How the scales are linked together computationally as shown in Figure 3.4 .
- How the information flows from one level to another as shown in Figure 3.3.

Beginning with the finite volume mesh used for the macro model (Physica), there is a cellular automata volume associated with each control volume. The CA volume uses the averaged value at the center of the control volume to return properties (solid fraction) to the volume. Similarly, with each cellular automata volume used in the modified Rappaz model, there is an associated molecular dynamics (MD) simulation box. The MD simulation, provides the *grain nucleation rate* and the *diffusion coefficient.*

The macro mesh can range from centimetres to metres, the micro mesh from microns to millimetres, and the nano simulation box from several angstroms to a fraction of microns.

The information flows as described below (see Figure 3.3)

- the composition of the alloy and the solidification path is passed from the microscale to the nanoscale,
- the grain nucleation rate is passed to the nucleation part of the micro model and the diffusion coefficient to the growth section of the micro model,
- the cooling rate and the temperature field are passed from the macroscale to the microscale model,
- the liquid fraction, via temperature, and the microstructure within the cast are passed from the micro level model to the macroscale level, and
- the material properties, such as the latent heat, the specific heat and the shear viscisity, are passed from the nanoscale to the macroscale.

The information is passed from one scale to another by creating relevant databases at each level and these are used as inputs to the other levels. *This mode of linkage is called*

the pre- and post-processing modes in which different programmes are executed seperatly in contrast to a fully coupled method which includes everything in the same programme and only one programme is executed and different levels are linked via the passage of arguments from one programme's subroutine to another for each node at each time step. Due to the extreme differences in the time and length scales involved, and also the execution time of different programmes at each scale, the pre- and post-processing modelling is adopted to link the coupled nano-micro model to the macro model.

- As pre-processor, the nano-micro model generates databases which are used as the input files of Physica and in its USER module.
- As post-processor the nano-micro model generates microstructures based on the local cooling rates and thermal history of selected elements in the finite volume mesh calculated by Physica.

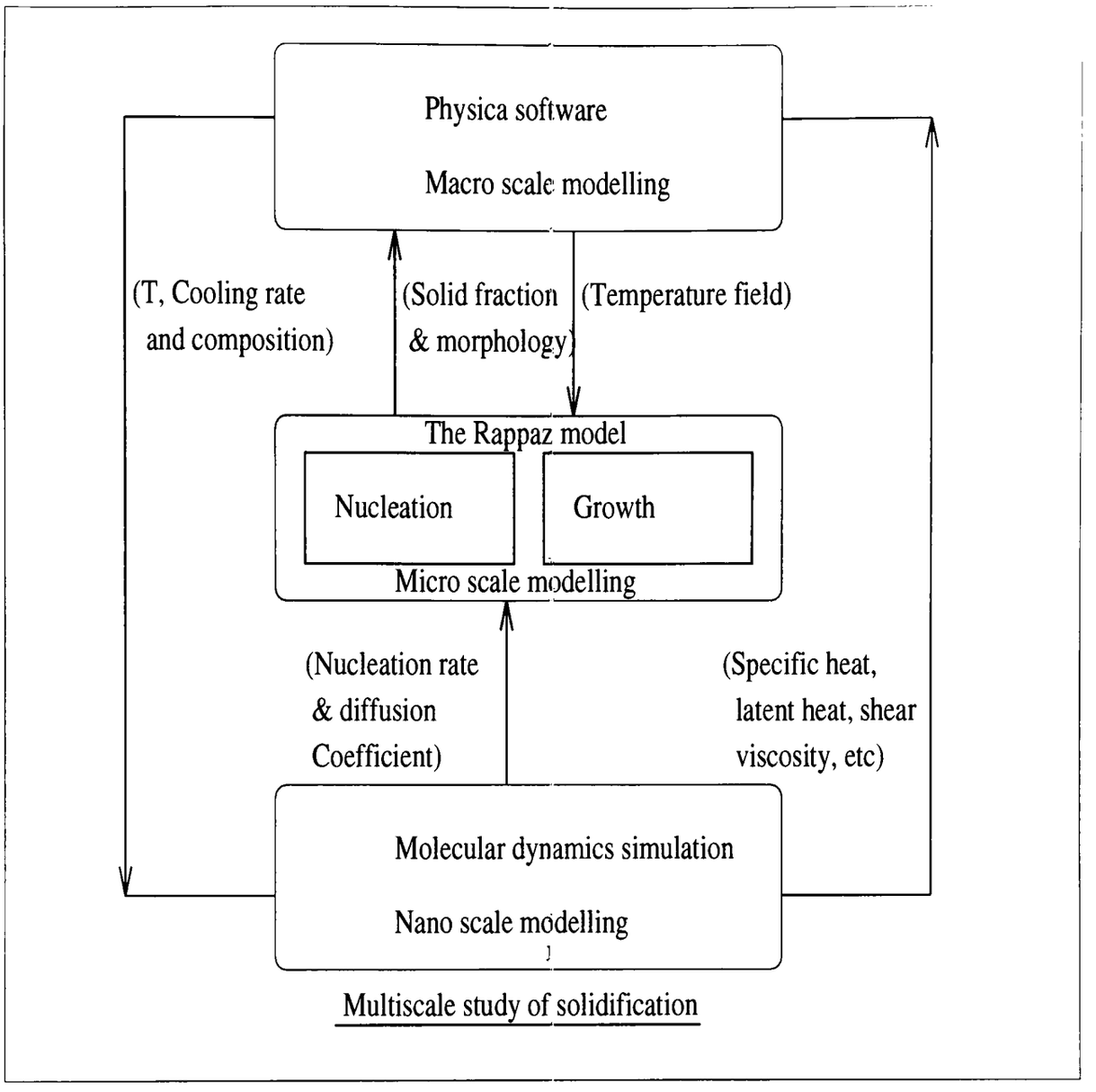

Figure 3.3: The flow of information

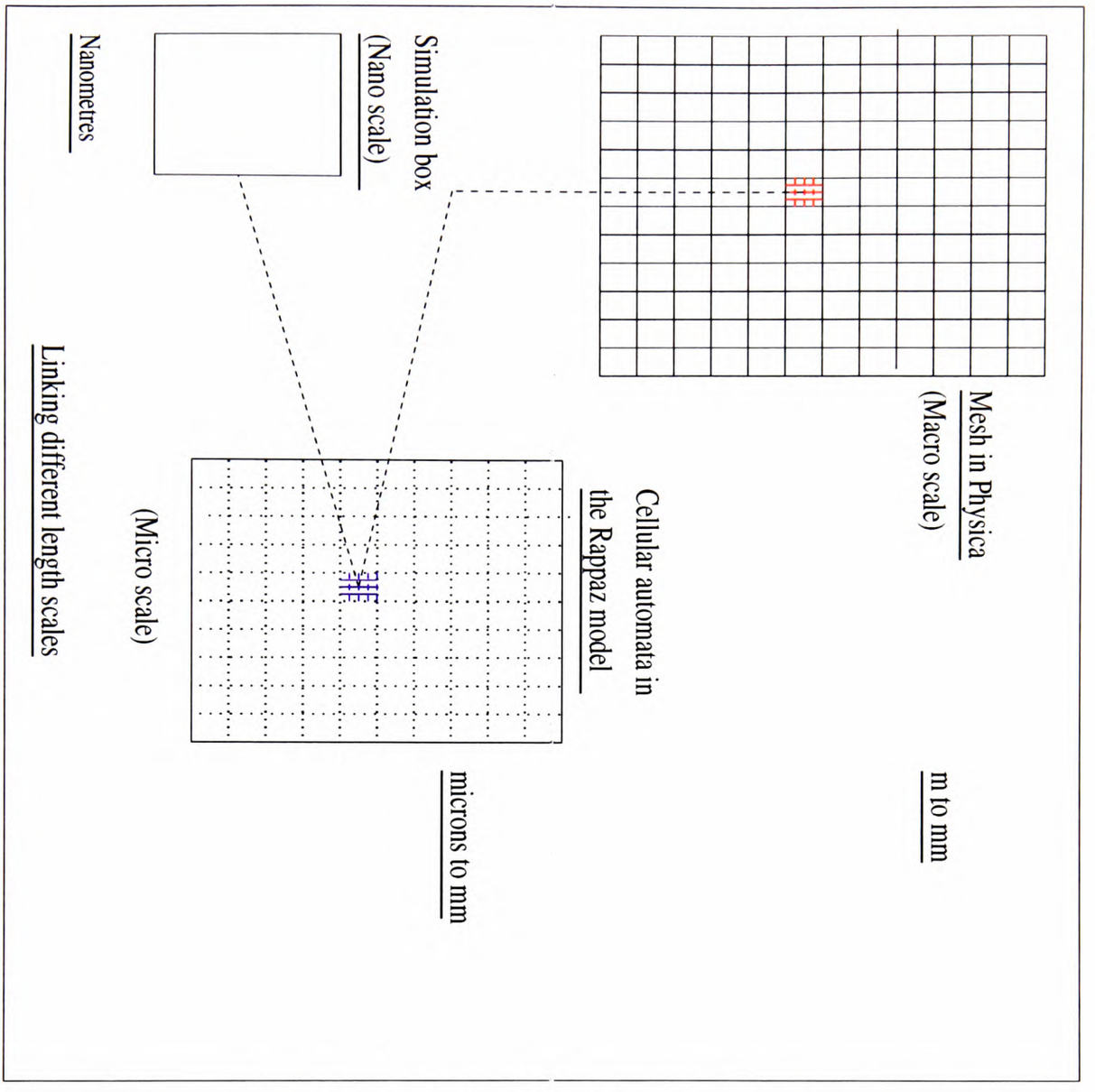

Figure 3.4: Zooming down the scales

3.3.1 Linking the nano-micro model to Physica

The linkage between the nano-micro model and Physica is achieved by adding two new subroutines to the USER module in Physica. One subroutine replaces the existing specific heat evaluation and the other one provides the variation of the liquid fraction with temperature.

By default, Physica uses a constant specific heat value and a linear function for the variation

of the liquid fraction. The use of a linear liquid fraction is inapropriate for a great number of alloys as the functional form of liquid fraction changes with the solidification path as can be seen in Figures 3.9 and 3.15 . Due to the fact that the variation of liquid fraction is used for the itterative evaluation of the source term in the enthalpy equation, the functional form used will influence the final temperature distribution of the cast. This means that using a wrong approximation for the liquid fraction variation with temperature can lead to incorrect prediction of hot spots and thermal stresses which in turn will influence the evaluation of mechanical properties.

In our model, based on the cooling rate imposed on the system by Physica, a database is created by the modified Rappaz model, which is used by Physica to evaluate the value of the source term at each time step and for each element. The subroutine in the USER model must provide four different values to the solidification module in Physica:

- the value of the liquid fraction based on a given temperature,
- the correction term defined by $T - F^{-1}(f)$ where T is the temperature and f is the liquid fraction.
- the gradient of the liquid fraction at a given temperature, and
- the value of the temperature for a given liquid fraction $(F^{-1}(f))$.

The constant value of the specific heat is also replaced by a temperature dependent analytical expression provided by the MD simulations.

3.4 Results and discussions

In this Section, results related to the Al-3%atSn, Sn-10%wtPb and Al-2%wtNi metallic alloy systems are discussed. For the first two cases, a full implementation of the coupled nano-micro-macro model is presented and for the last case,microstructures are produced by post processing.

Two cases are studied, for the first two systems. The first case is Physica alone, without any link to the nano-micro model, for which the microstructures are produced by postprocessing. The second case has the same initial and boundary conditions for the tempearute field and the same process parameters, such as the cooling rate, but linked to the nano-micro model via databases, for which microstructures are also produced.

3.4.1 Al 3%atSn binary system

3.4.1.1 Model description

A plate with dimensions of 10cm length, 10cm width and 1cm thickness is considered. The initial pouring temperature is set at 940K. The side faces and the bottom face of the plate were in contact with a chill set at 750K, and the top face is in contact with air set at 300K. The cooling rate is 1.9K/s and the simulation is done for 100 time steps with a time step, Δt, of 1s. Solidification range is from 933K to 850K. The heat equation is solved for the temperature field.

3.4.1.2 Physica with no link

The temperature field for Al-3%atSn, is given in Figure 3.5. The system is completely solidified after 100 seconds with a maximum temperature of 708K near the chill and a minimum temperature of 367K on the surface.

Microstructures were produced for 4 different control volume centers at 677K, 584K, 491K and 398K as seen in Figure 3.6. The control volume at 677K which is in contact with the mould by three of its faces had the smallest local cooling rate. The element at 398K is in contact with air and had no contact with the mould and has the highest local cooling rate. The differences in their respective microstructures are obvious. For the former element, columnar grains with some distributed equiaxed grains, with different $< 100 >$ crystallographic orientations are visible. In the latter case, the structure is equiaxed with gains having their $< 100 >$ crystallographic directions within the range of [0-9] degrees. The main reason for this variation in the microstructure is the boundary conditions at the mould. The mould temperature is higher than air, therefore elements in contact with the mould have higher final temperatures than those in contact with air. On the other hand, the roughness of the mould's surface, will activate nucleation sites on the surface of the liquid and will also lower the critical undercooling for the grains associated with non prefered growth directions (higher than 10 degrees) due to the heterogeneous nucleation.

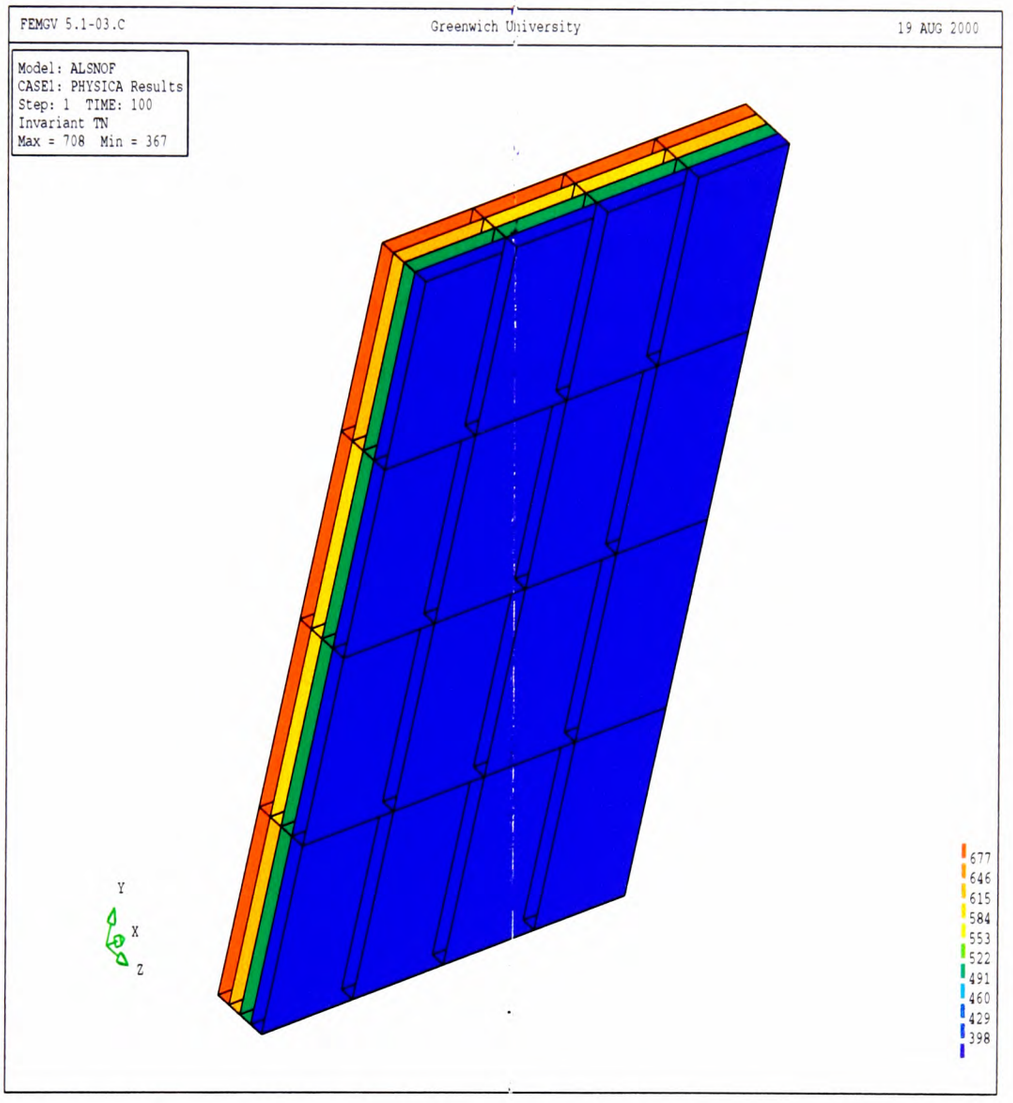

Figure 3.5: Temperature field for Al 3%atSn binary system after 100 seconds, produced by Physica

3.4.1.3 Physica linked to nano-micro model

The Physica programme is run for the same system, with the same set of initial and boundary conditions but with input coming from the nano-micro model. The temperature field is given in Figure 3.7, produced by Physica. As in the previous case, the system is completely solidified after 100 seconds with a maximum temperature of 746K near the mould and a minimum temperature of 389K near the surface. In comparison to the previous case, the temperatures were higher and local cooling rates were smaller. This means that one must observe larger columnar zones than the previous case as nucleated columnar grains have more time to grow. This can be seen in Figure 3.8 in comparison to Figure 3.6. Microstructures are given for 4 elements at 719K, 614K, 514K and 416K. The same differences can be observed between elements at 719K and 416K as described in the previous case.

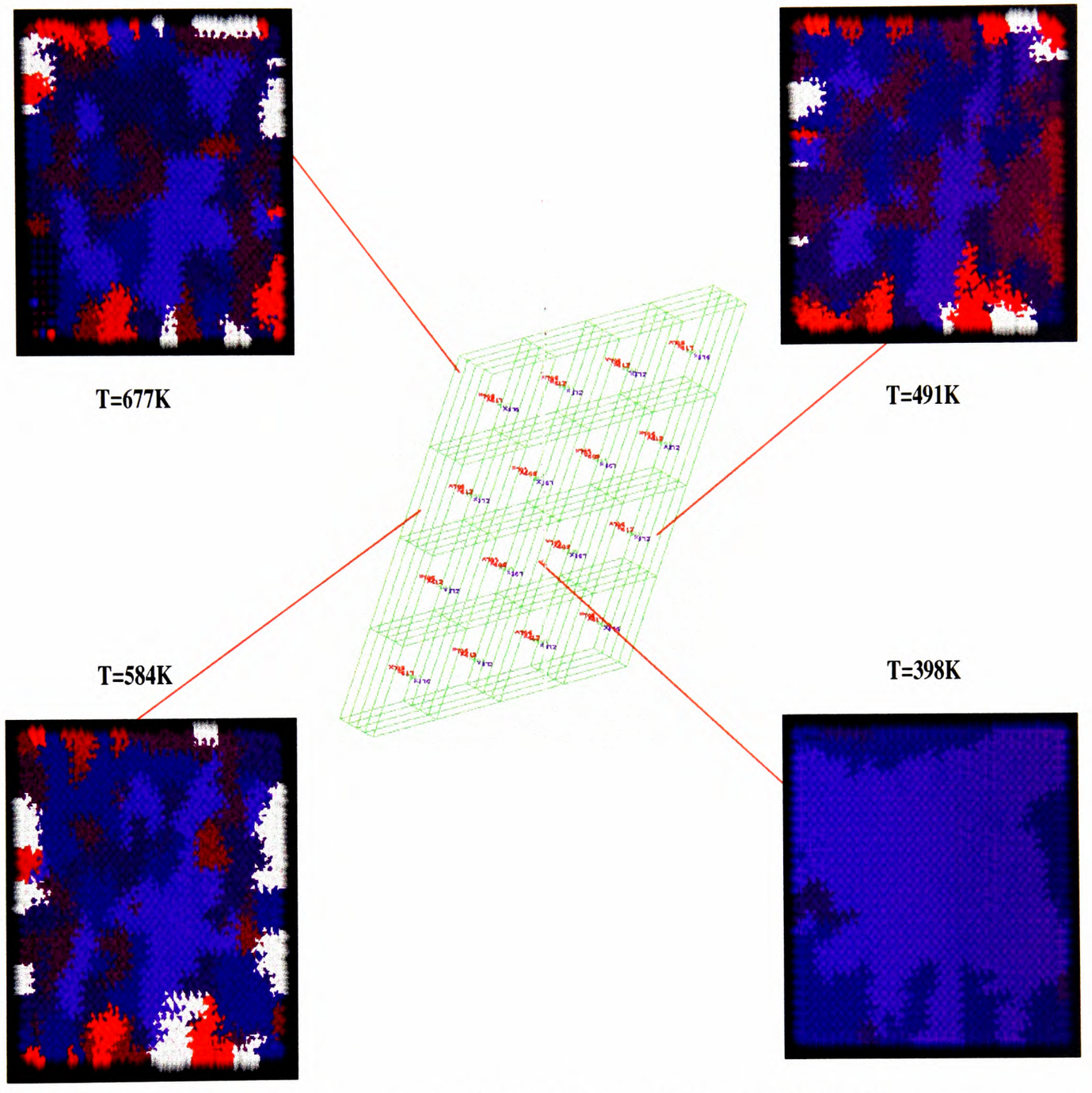

Figure 3.6: Microstructures obtained after 100 seconds for Al 3%atSn binary system

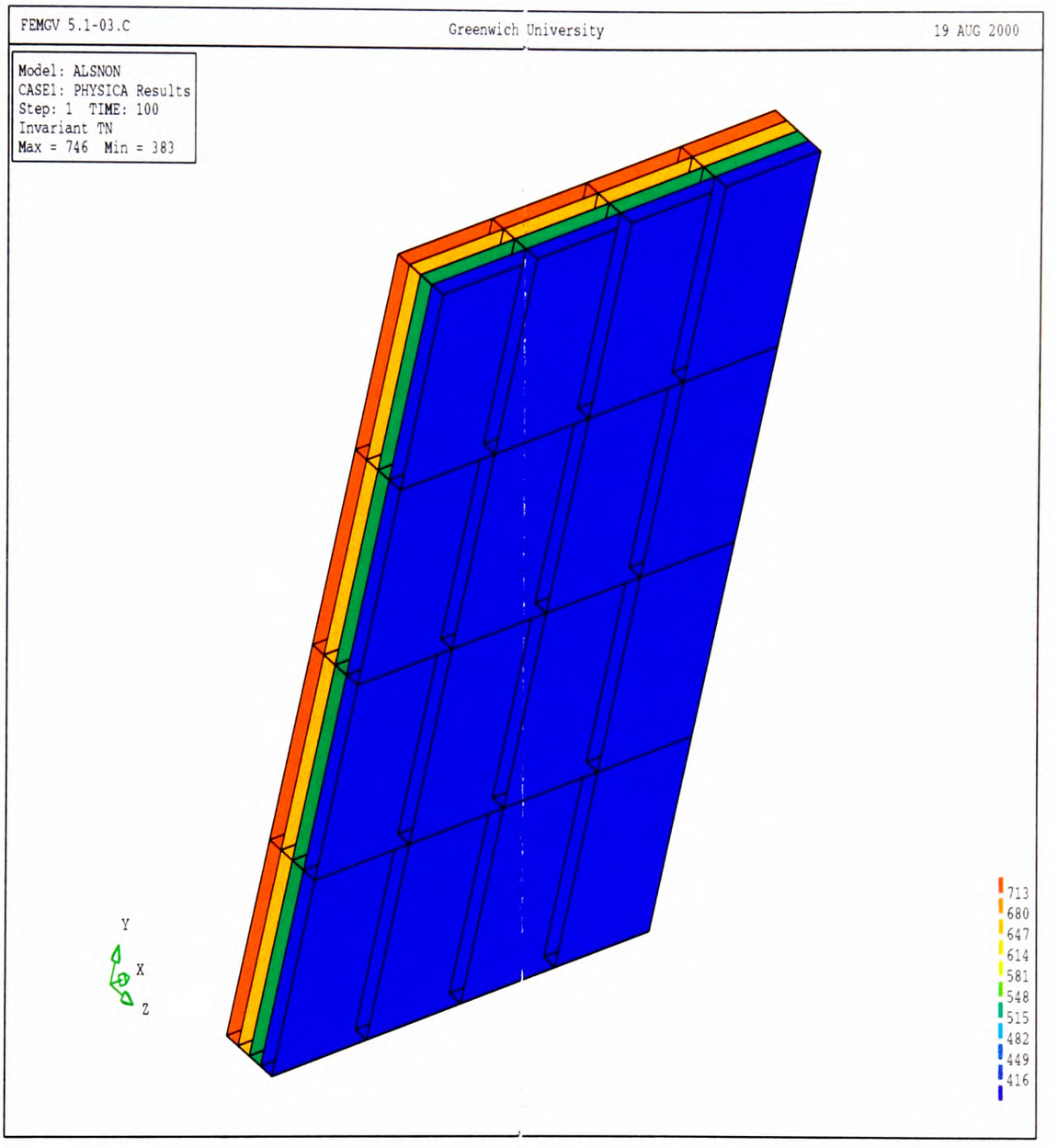

Figure 3.7: Temperature field obtained after 100 seconds for Al 3%atSn binary system, produced by Physica

By comparing Figures 3.8 and 3.6 two main conclusions can be obtained

- Without the link to the nano-micro model, the system releases heat much more quickly than it should. This was due to the assumption made for the variation of the liquid fraction with temperature. In the case where the nano-micro model was used, the variation of the liquid fraction with temperature was given by Figure 3.9. A table lookup was used, instead of a fitted function for computer overall efficiency.

- The prediction of the solidification microstructure was only possible due to the use of the nano-micro model as a post-processor to Physica even when no output of the nano-micro model was used as input.

If the multiscale methodology were not used, the macro model would only have been able to predict the temperature and stress field with a limited accuracy due to constant material properties and the approximation of the liquid fraction temperature relationship. The use of the multiscale strategy enabled us to not only remove several major empirical assumptions from both micro and macro levels, but also to produce qualitatively correct local microstructures.

Therefore, at this stage, *virtual casting* and *computational metallography* can be presented. Even at this early stage of development, the virtual casting can be considered as a serious complement and in some cases as alternative to costly and time consuming laboratory experiments. Multiscale modelling of solidification has been shown to be a viable method for the virtual casting and computational metallography.

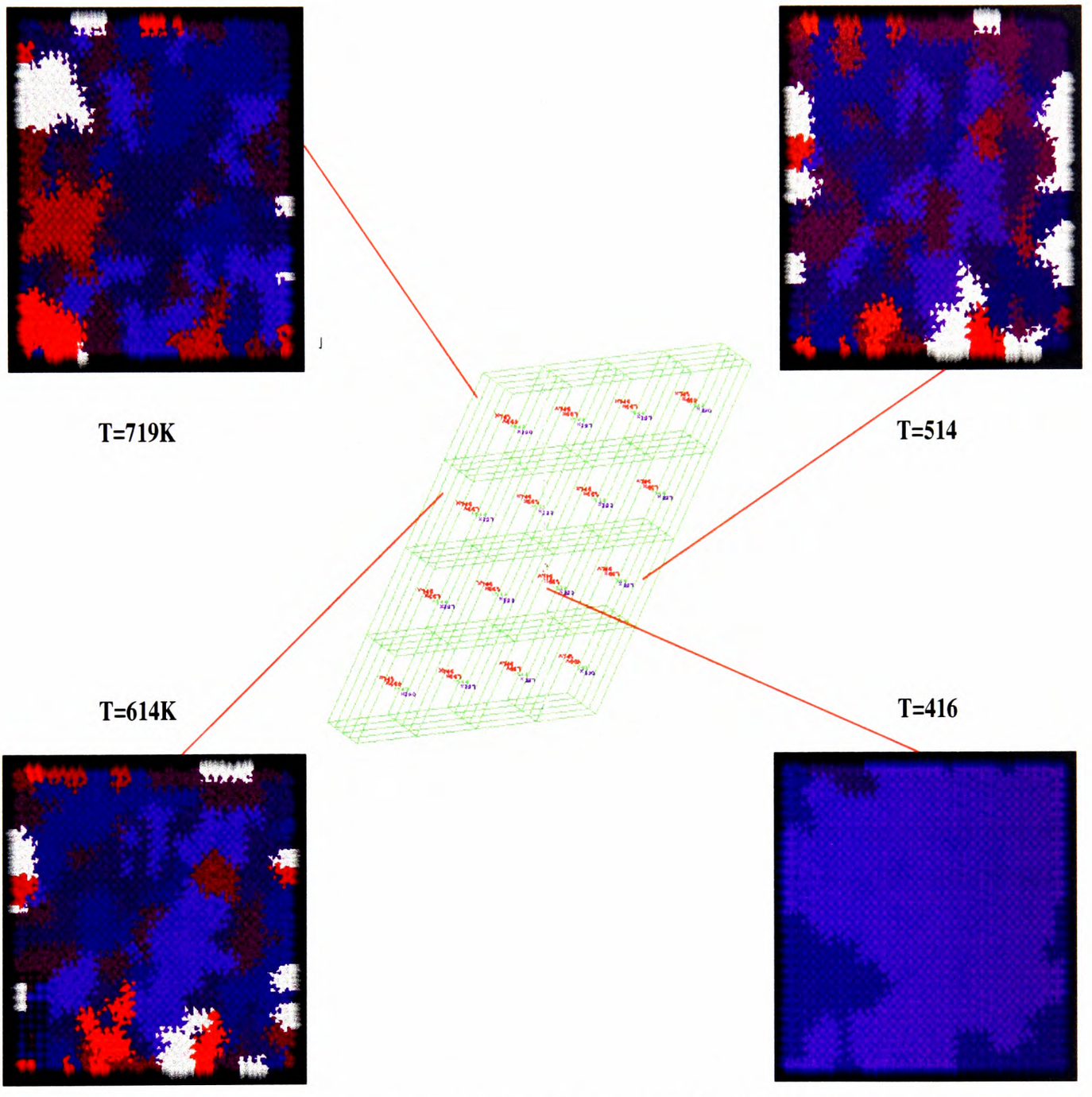

Figure 3.8: Microstructures obtained after 100 seconds for Al 3%atSn binary system

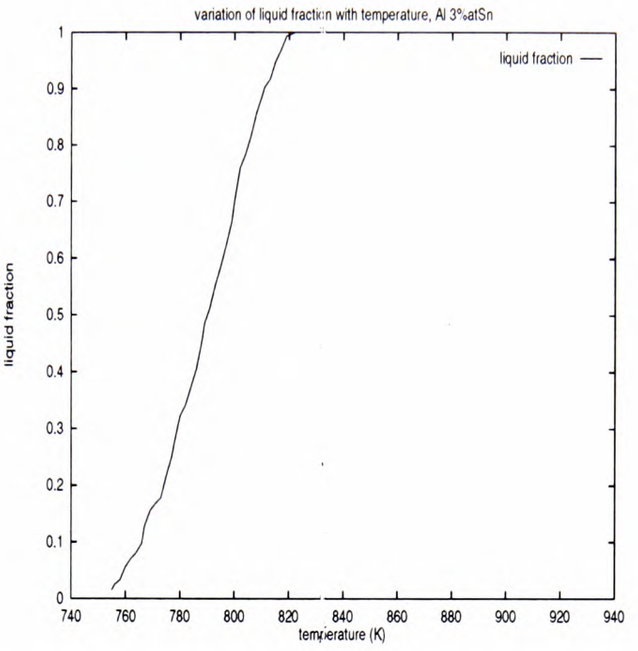

Figure 3.9: Liquid fraction via temperature for Al 3%atSn binary system

3.4.2 Sn-10%wtPb binary alloy

3.4.2.1 Model description

A plate with dimensions of 10cm length, 10cm width and 1cm thickness was considered. The pouring temperature was 600K. Side and bottom faces were in contact with the chill set at 400K and the top face was in contact with air at 300K. The cooling rate was 2.0K/s and the programme was run for 100 time steps, each time step was equal to 1s. The solidification range was from 505K to 468K.

3.4.2.2 Physica with no link

The temperature field produced by Physica was given in Figure 3.10 with a maximum temperature of 408K near the chill mould and a minimum temperature of 329K near the surface. Microstructures were presented for 4 control volume centres at 401K, 379K, 351K and 336K as shown in Figure 3.11. The system was completely solidified after 100 seconds.

The case of Sn-Pb was different from Al-Sn due to the shorter solidification range (505K to 468K instead of 933K to 850K). A larger number of grains nucleate over a small range of temperature, therefore a shorter growth period and the possibility for grains with a random crystallographic orientation to remain in the final cast. Therefore, more equiaxed grains (no preferential growth directions) were observed in comparison to Figure 3.6. Despite this difference, there were still more equiaxed grains where the undercooling was higher (336K) and far from the mould wall (the mould walls activate more nucleation sites as described in Chapter 2) and at a smaller undercooling.

As already described in Chapter 2, the surface nucleation was dealt with by decreasing the critical undercooling at the wall, using a small contact angle and by having an unisotrope growth law which privileges grains with their $< 100 >$ crystallographic direction aligned with the heat flow. As the CA volume was thermally uniform and time dependent a general direction had to be imposed on the whole CA volume in order to simulate the effects of the heat flow within a larger volume comprising the CA volume. This was how the elongated grains similar to columnar structures are produced by the model.

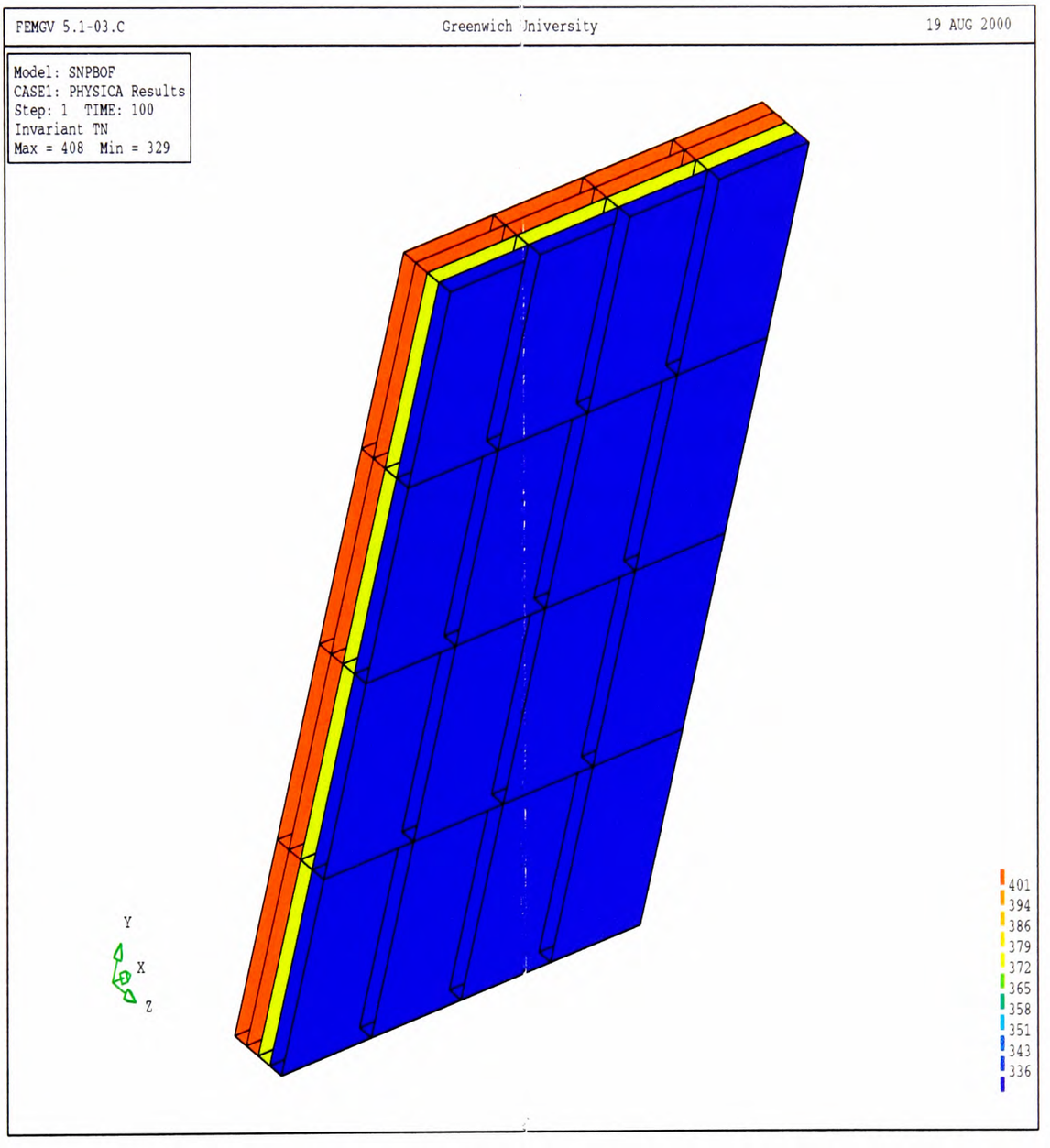

Figure 3.10: Temperature field obtained after 100 seconds for Sn 10%wtPb binary system, produced by Physica

3.4.2.3 Physica linked to the nano-micro model

The temperature field produced by Physica was given in Figure 3.12 with a maximum temperature of 475K near the mould and a minimum temperature of 356K near the surface. Microstructures are presented for 4 control volume centres at 465K, 471K, 400K and 367K. It was shown in Figure 3.14 that after 100 seconds, the alloy was not completely solid and there were some elements in the middle of the cast which were still mushy. By comparing the cases of linked and unlinked Physica simulations, not only we could observe higher temperature as we did for the Al-Sn system but in addition, the linked case could predict the existence of hot spots (last regions of liquid to be solidified) not detected by the unlinked simulation. The comparison between elements at 465K and 471K was quite interesting. The former element was outside the solidification range and despite its high temperature was totally solid but the latter element had a temperature which was within the solidification range and the value of liquid fraction was around 0.25 which meant that despite a solid appereance the element was still mushy. Microstructures are presented in Figure 3.13. As local cooling rates were smaller than the unlinked case, the columnar zone was more developed.

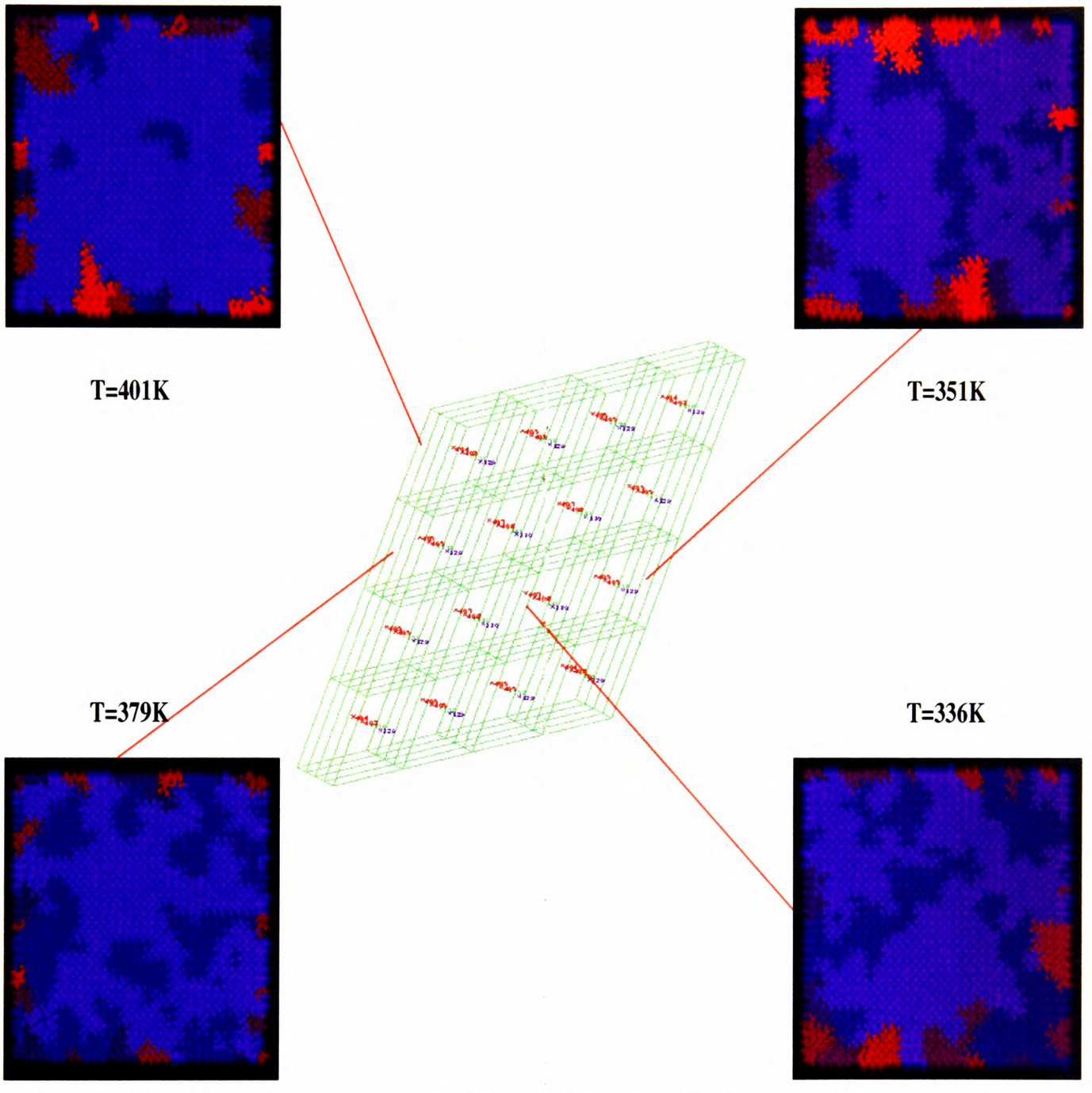

Figure 3.11: Microstructures obtained after 100 seconds for Sn 10%wtPb binary system

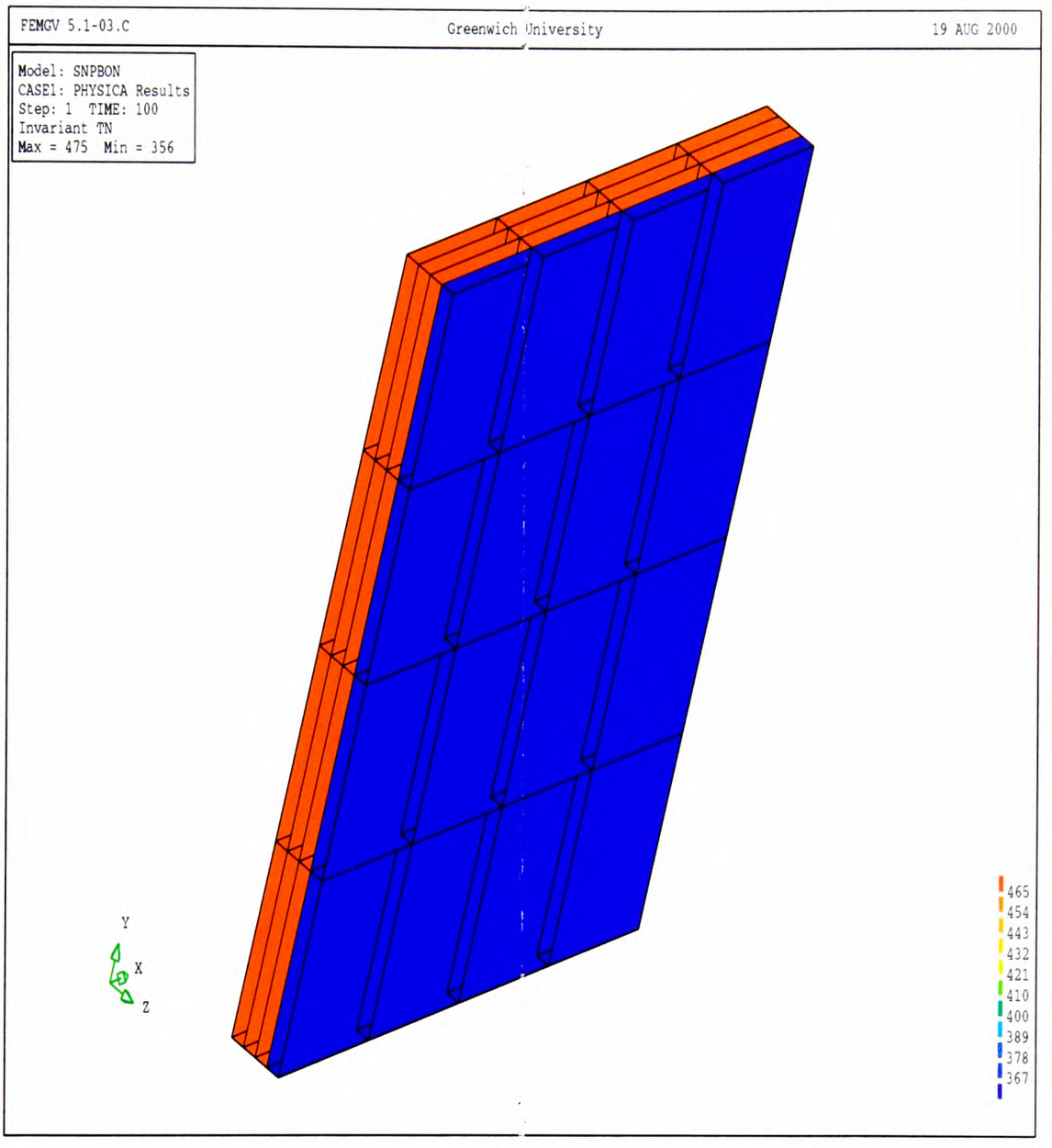

Figure 3.12: Temperature field obtained after 100 seconds for Sn 10%wtPb binary system, produced by Physica

As shown in Figure 3.13, for the element at 475K, the stripes of liquid (dark blue lines) were concentrated near the dendrite arms of the columnar grains as the solute rejection was at maximum in these areas and therefore the constitutional undercooling was quite high which allowed for lower local freezing points and therefore the existence of a liquid region.

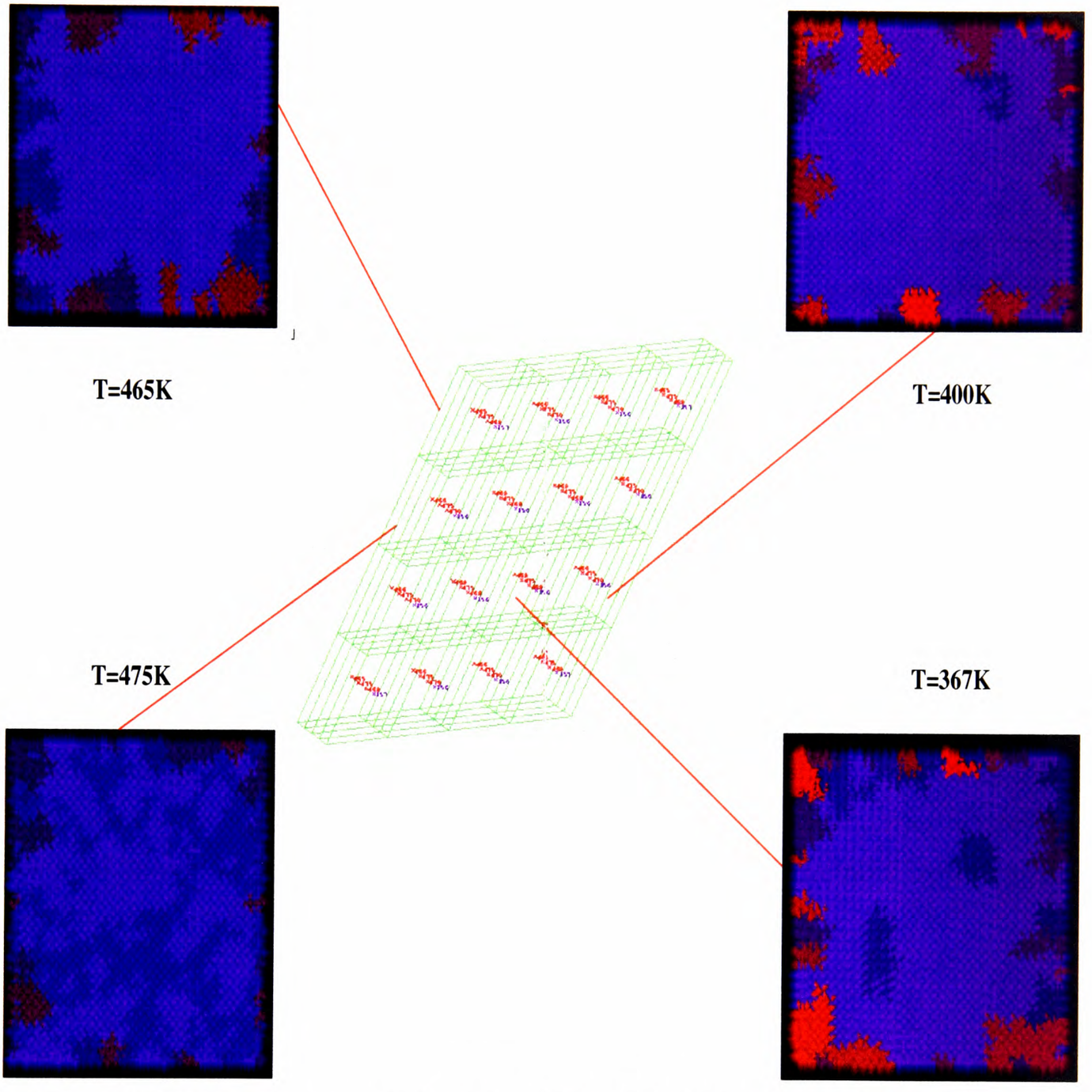

Figure 3.13: Microstructures obtained after 100 seconds for Sn-10%wtPb binary system

The liquid fraction via temperature used to obtain a functional fit was shown in Figure 3.15. Comparing this Figure with the one corresponding to the Al-Sn alloy, a step-like shape was observed in opposition to the nearly linear form for Al-Sn. This confirms that the columnar zone was less developed than in the case of Al-Sn because the time for growth was decreased and grain nucleation was more like a big-bang.

3.4.3 Al based alloy approximated by Al 2%wtNi

To demonstrate the application of the multiscale model as a post-processor to generate solidification microstructure of complex industrial casting, the case of an aluminium based alloy, used for air blades in low temperature compressors was considered. The real alloy was approximated by a binary Al-2%wtNi alloy as aluminium and nickel constitute up to 99% of the alloy. The macro modelling was conducted by Dr. A. Williams [3].

3.4.3.1 Results produced by the modified Rappaz model

The geometry of the cast and also the thermal history of five selected volume elements within the cast are given in Figure 3.16. It was shown that the local cooling rates were nearly the same for all five chosen volume elements. This means that all five volume elements must have had the same kind of microstructure. As the cooling rates for these elements were low (0.24 K/s), the main structure was a columnar-like structure containing large elongated grains, with some variations in a possible but restricted equiaxed zone. Another important factor influencing the local microstructure was the local geometry. Microstructures and their corresponding elements are given in Figure 3.17.

[3] RA at the university of Greenwich, centre for numerical modelling and process analyses

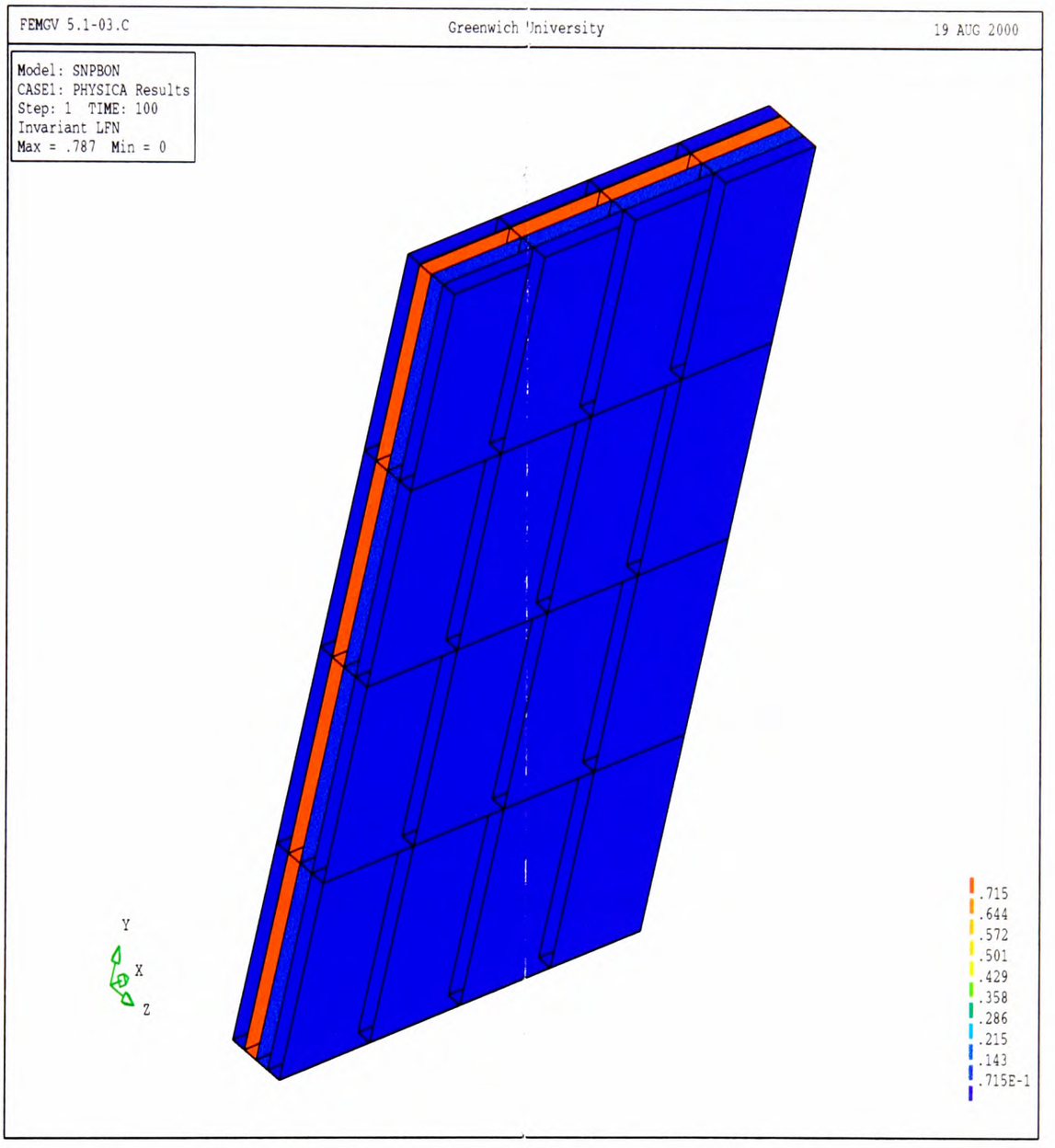

Figure 3.14: Liquid fraction distribution obtained after 100 seconds for Sn 10%wtPb binary system

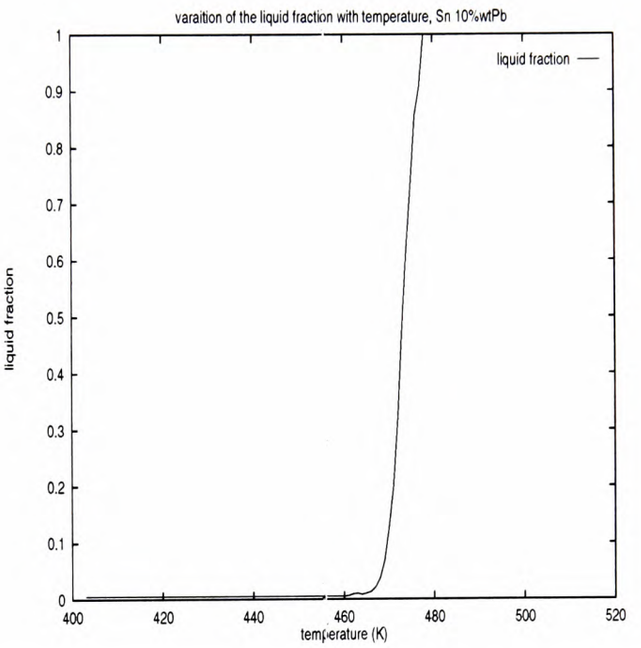

Figure 3.15: Liquid fraction variation with temperature for Sn 10%wtPb binary system

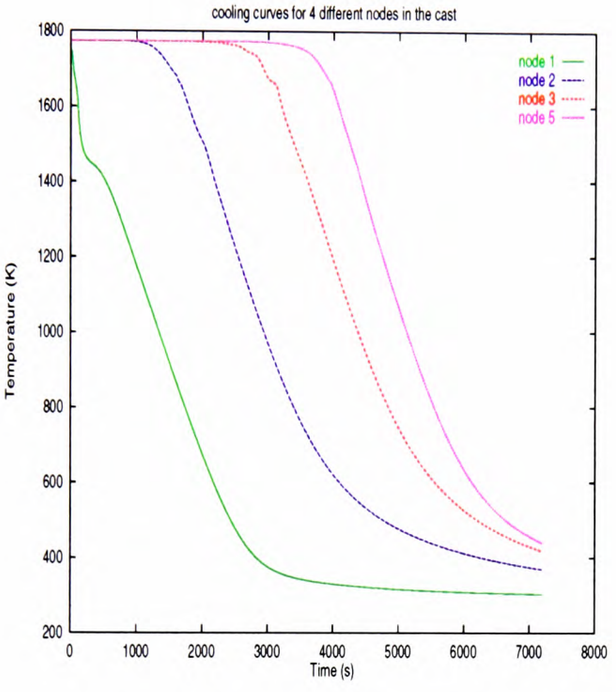

Thermal and geometrical characteristics of the Al based alloy used for air blades.

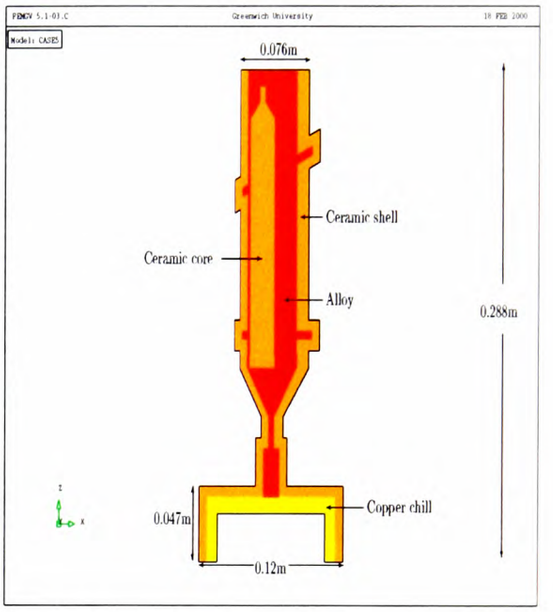

Figure 3.16: Curves on the left hand side represent the cooling curves for various mesh elements chosen throughout the cast. The scheme on the right hand side represents the geometry and dimensions of air blade.

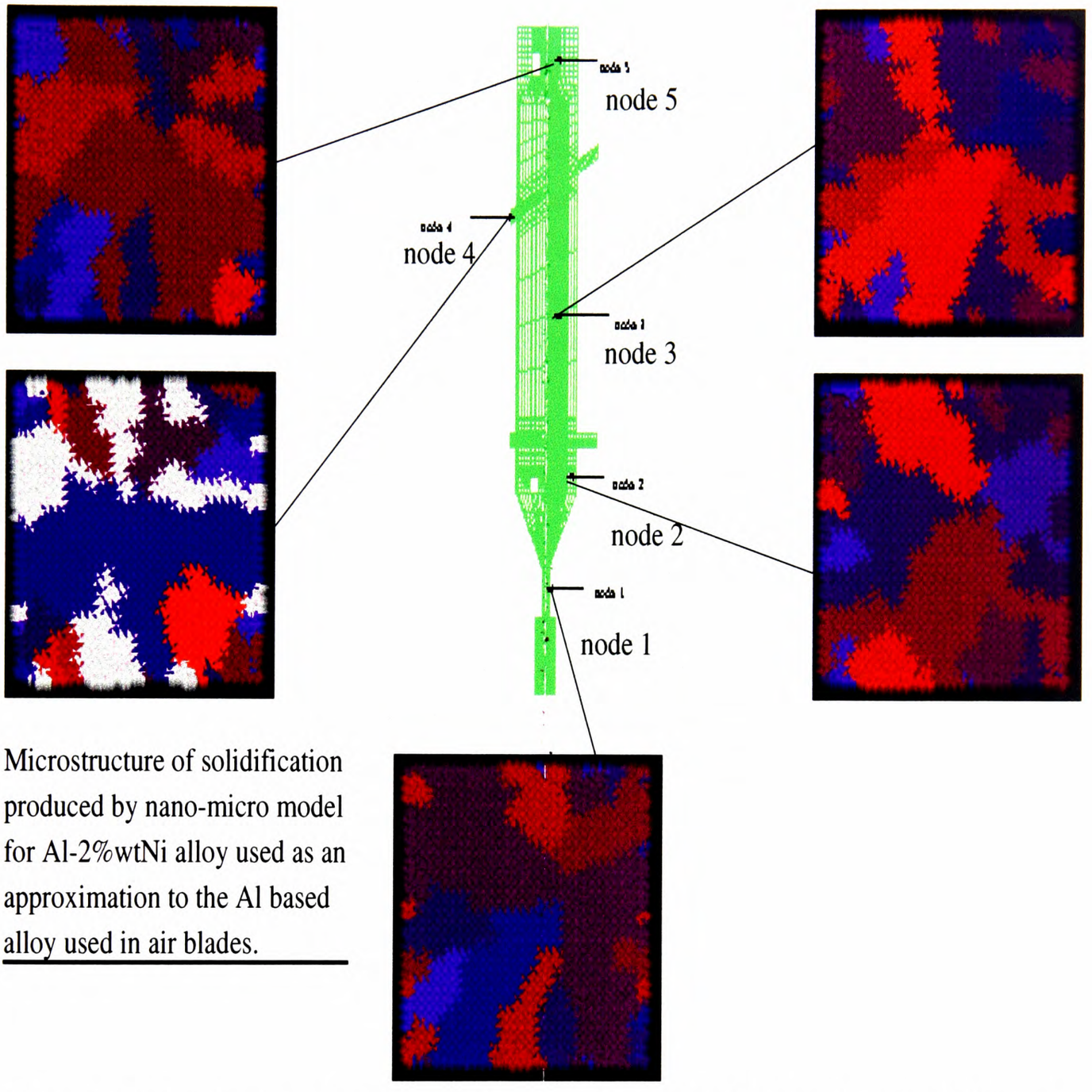

Microstructure of solidification produced by nano-micro model for Al-2%wtNi alloy used as an approximation to the Al based alloy used in air blades.

Figure 3.17: Local microstructures, produced by the nano-micro model used as the post-processor to the Physica software, at five selected control volume centres within the cast at the end of the solidification.

As seen in Figure 3.17, microstructures of solidification were all formed of large elongated grains. The most visible difference was between element number four and other elements. Despite the fact that the microstructure was also formed of large and elongated grains, the grain orientation was different. Element number four was extremely thin in the direction of the heat flow, therefore it was going to solidify faster through its thickness rather than its width. This means that locally, the elongated grains were grown in the remaining liquid which was through the width of the element. This causes grains, perpendicular to the general heat flow, to grow, in addition to those in the direction of the heat flow (white regions in the fourth element's microstructure represent grains with an orientation of 81 to 90 degrees with regard to the heat flow direction). These results are qualitatively in accordance with experimental observations [98].

3.5 Discussions and conclusion

What has been presented in this Chapter was an attempt to implement and to apply a multiscale modelling of solidification to several important industrial alloys. The model and strategy detailed in this Thesis can be applied to any binary system and the choice of Al and Sn based alloys were purely practical. The concept of *virtual casting* and *computational metallography* was of a great importance to automotive, aerospace and electronic packaging industries due to their potentiality to predict microstructural effects based on a given set of process and alloy parameters and therefore the evaluation of important material properties based on the obtained microstructure. The multiscale model presented in this Thesis can be developed further and can mostly be used to predict tendencies than direct quantitative predictions. As any new proposed methodology, it has its own advantage and disadvantages which can be summarized as follows

3.5.1 Advantages of the multiscale modelling

- The most important aspect of the multiscale model proposed in this Thesis was a comprehensive study of the solidification process, beginning from the atomistic clusterisation to the macroscopic segregation. Using atomistic theory, in the case of nucleation and growth, enabled us to replace empirical assumptions based on experimental measurements by theoretical calculations based on atomic positions and velocities. Furthermore, the determination of the temperature-dependent material properties directly from the nanoscale can provide macro modelling with accurate materials data input.

- A great number of process parameters and alloy specification can be controlled using the multiscale modelling within a reasonable amount of computer time and with a minimum cost which can make the multiscale modelling a suitable tool for material property prediction and design for industry. Therefore, virtual casting and computational metallography can be used along side the usual laboratory experiments to provide the manufacturer with a better understanding of the phenomenon and also with a powerful

prediction tool for microstructural based material properties.

3.5.2 Limitations of the model

The multiscale model proposed in this Thesis was at its early stages of development and a lot more can be done to make it more suitable to deal with real industrial applications. The main limitations of the present model are as follows

- Like the experimnetal measurement of thermo-physical properties, a series of runs must be completed using the nanoscale model in order to produce a complete database. This was time consuming. Three cases can be considered, in the first case, the interatomic potential for the alloy and for each one of the alloying elements was not rvailable, therefore, first principle calculations are needed to inodel this potential. This process can take up to several months but once created for a given crystallographic structure and validated, it can be easily extended to other materials with similar crystalline structure. The second case was when the potential for each one of the alloying elements was avialable but not for the alloy. In this case (this was the case for Sn based alloys) a mixing rule based on the existing elemental potentials must be obtained in order to represent the alloy interactions. This process can take several months (three months in the case of Sn based alloys). The last case was when the potential was available for the alloy under investigation. Once the interatomic potential was determined, a great number of MD simulations must be run in order to obtain different material properties at various temperatures. As an average, the evaluation of the specific heat at ten different temperatures for each alloy would take about a week. The same amount of time must be considered for the diffusion coefficient and the nucleation rate. Once the atomistic part was finished, the micro and the macro simulations can be conducted. Their time interval depends largely on the number of CA cells or mesh elements considered and can vary between several minutes to several days of run time. In our case (10000 CA cells for $200\mu m \times 200\mu m$ surface area and 10000 mesh elements) each micro and macro simulation required several hours of run time. As it can be seen from above, once the databases are available, simulations

can be done quite fast. Therefore, for multiscale simulations to be fast and applicable, predetermined interatomic potentials are necessary. Once calculated, atomistic models can produce accurate and reproducable databases.

- The other limitation of this model was the fact that it was run as three seperate programmes each one of which must be set up and run. A better way would be the complete integration of the nano and micro scales within the macroscale, which will not be possible without the advent of extremely fast and powerful computers, much faster than what was available today in the market.

Even with its present limitations, the model has contributed to the field of virtual casting and computational metallography by

- Evaluating the nucleation rate via atomistic modelling and replacing the existing empirical functions.
- To improve the modelling of dendrite growth by introducing the Ito stochastic dynamics, taking into account the interface velocity and the tip diffusional noise.
- To replace constant material properties by temperature-dependent material properties throughout the mushy zone temperature range.
- To replace empirical functions of the liquid fraction via temperature with their correct variations based on process and alloy parameters.
- To enable us to predict microstructural features based on the alloy and process parameters.

Summary and conclusions

The aim of this Thesis was to propose a multiscale model for virtual casting and computational metallography by taking into account the major aspects of phase transformation in metallic systems beginning from the atomistic clusterisation and culminating in macroscopic segregation. The parameterisation of different levels involved in the process and the linkage of these various scales via passage of relevant parameters' values formed the basis of the multiscale approach. The complexity of the process and the extreme differences between the time, length and energy scales involved, made the task of linking different scales a difficult one. As the nucleation of solid nuclei begins at the atomistic level (in metallic systems, arround 150 atoms can rearrange and create a solid nucleus) due to the atomic clusterisation by random collisions within the liquid, our first task was to determine with precision when during the process, these clusters formed within the liquid state became stable and could hold together in order to form the solid nuclei. To achieve this, the variation of the Gibbs free energy of the system was monitored. The stability of any cluster depends on the change in the Gibbs free energy of the system due to the creation of the cluster and if this change is favourable (if the system can reduce its total energy) then the cluster can be stabilised and maybe grow.

As we are dealing with phase transitions, it was necessary to detect with accuracy the moment at which this transition occurs during the process. As in the case of the Gibbs free energy which is influenced by the phase change and its decrease during the liquid-solid transition is the main driving force for the transition, the order of the system is also influenced by the phase change. The atomic clusterisation will increase the internal order of the system and this change in the order can be quantified and observed. It can be quantified by evaluation of the radial distribution function, translational order parameter or the running mean square displacement. The visualisation is possible by simulating the change in the crystallographic structure of the atomic system.

Therefore, in order to model the phase transition at atomistic level, three aspects of the phase change were monitored

- change in the Gibbs free energy,

- change in the order of the system, and
- change in the crystallographic structure of the sytem.

Unfortunately, not all of these pieces of information are useful for the linkage of the atomistic scale to the micro and macro scales. What we neede to link the atomistic level to the micro level was a set of parameters allowing us to link the nucleation and growth of solid nuclei within the system.

As the grain nucleation is based on the energetic aspects of the process, the use of Gibbs free energy and more precisely the residual chemical potential representing the entropic part of the Gibbs free energy and related to change in order of the system was considered to be a valid starting point for the linkage. Regarding the growth of grains already nucleated, the diffusion controlled growth was considered and, therefore, the diffusion coefficient of the atomic system was considered as the possible link.

On the other hand, a link was necessary between the atomistic level and the macro level. Not only the macro level must be linked to the atomic level, but also the alloy and process parameters at macro level must in turn influence the atomic level. The macroscale simulations are mainly used for the numerical solution of the heat and mass flow during the phase change. They rely on accurate and temperature dependent material properties, such as specific heat, latent heat, shear viscosity and density, for their simulation. As these data were not available in many cases the passage from calculated material properties directly at atomic level, to the macro level seemed to be a valid link. The influence of the alloy solute concentration and the solidification path were incorporated at the atomic level for the evaluation of the material properties and, therefore, the macro level conditions can influence the atomic simulation.

At this point the micro and the macro levels had to be linked. The linkage of these two scales is useful due to the capability of micro models to generate the cast's microstructure based on the local temperature field. The best link possible is, therefore, via the relation between the temperature field evaluated at the macroscale for the whole macro volume and the microstructural changes whithin the system quantified by the solid fraction. The link is therefore possible through the source term of the energy conservation equation used at the

macroscale to solve the temperature by passing the variation of the solid fraction evaluated at the microscale at each time step and for each node to the macroscale and feeding back the temperature field to the microscale for a new evaluation of the solid fraction.

Links between all different scales can then be summarized as follows

- The value of the residual chemical potential evaluated at the atomic level is passed to the nucleation routine at the micro level.
- The value of the diffusion coefficient evaluated at the atomic level is passed to the growth routine at the micro level.
- Values of latent heat, specific heat and shear viscosity varying with the temperature and evaluated at atomic level are passed to the macro level.
- The value of the solid fraction for a given temperature is passed at each time step and for each node to the macro level.
- The temperature field is passed to the micro level for the evaluation of the new solid fraction.
- The value of the solute concentration and cooling rate at macro level is passed to the atomic level for the evaluation of the material properties databases.

These links are graphically represented in Figures 1 and 2. What are the advantages of the multiscale approach? The main advantage of such a model is that it considers more of the physics of the process than any of the models at atomic, micro or macro levels alone. This means that fewer empirical assumptions and experimental fittings are necessary which gives the model a solid physical basis and also more accuracy. On the other hand the need for less experiments and the ability to calculate material properties for a series of similarly structured systems render the model more flexible and faster for its application to metallic systems. We can therefore, summarise these advantages as follows

- the empirically fitted nucleation rates for the surface and bulk nucleation were replaced by calculated nucleation rates based on the variation of the residual chemical potential and the use of an angular factor representing the properties of the mould's surface,
- the growth of the dendrite tip is modelled using the Ito stochastic dynamics, taking into account the velocity of the interface and the diffusional noise of the tip, and
- a set of temperature dependent material property databases are produced by the atomic simulations and used directly as input to the macro simulation, replacing the existing constant material properties.

The multiscale model proposed in this Thesis is in its early stage of developement and limitations are applied to this model. One of the main limitations of this model is its uncoupled structure. This means that three different programs in atomic, micro and macro scales must be run seperately, each one producing databases used as input for other scales. On the other hand, the atomic simulations are based on the use of interatomic potentials which are not always available for a given system and need to be modelled which can take a great amount of time. Therefore, for the current model following limitations exist

- the model works as pre- and post-processor and is not fully coupled, and
- the atomistic modelling is limited by the availability of the interatomic potentials.

Future Work

The multiscale modelling of phase transformation is extremely complex and many different improvements are possible. The following aspects of the model can be improved

- the linkage between the atomic and micro level can be improved by incorporating more physics based on the atomic calculations into the micro model. This can be done via
  - the evaluation of the surface tension using the nano-thermodynamics directly at atomic level and its passage to the nucleation part of the micro level,
  - physical calculation of the angular factor characterising the surface properties (shape and chemistry) using the surface science principles in atomic simulations,
- a set of binary and ternary interatomic potentials for different crystallographic structures can be developed in order to increase the aplicability of the multiscale model, and
- the micro and macro models can be fully coupled using a multi-grid approach within the macro model.

Each one of these improvemnets can take a long period of time to implement and as any other model it can and it will undergo continuous modifications.

Bibliography

[1] R. E. Spear, G. R. Gardner, AFS Trans., Vol. 71, 209, 1963

[2] J. M. Boileau, J. W. Zindel, J. E. Allison, SEA Technical Paper Series, International Congress and Exposition, Detroit, Michigan, 1997

[3] C. H. Caceres, B. I. Selling, Mater. Sci. and Engineering, A220, pp 109-116, 1996

[4] J. A. Eady, D. M. Smith, Mater. Forum, Vol. 9, No. 4, 1986

[5] D. Christian, The Theory of Transformations in Metals and Alloys, Pergamon Press, 1965

[6] F. Seitz, D. Turnbull and H. Ehrenreich, Solid State Physics, Vol. 22 Academic Press, 1968

[7] C. Kittle, Introduction to Solid State Physics, Wiley edition, 1968

[8] D.A. Porter and K.E. Easterling, Phase Transformations in Metals and Alloys, Van-Nostrand Reinhold, 1984

[9] N.E. Cusak, The Physics of Structurally Disordered Matter, Adam Hilger Publications, 1987

[10] K. Huang, Statistical Mechanics, Wiley eddition, 1987

[11] E.S.R. Goral, Statistical Mechanics and Properties of Matter, John Wiley and sons, 1974

[12] K. Fisher, Fundamentals of Solidification,Trans Tec Publications, 1986

[13] M.P. Allen and D.J. Tildesley, Computer Simulation of Liquids, Oxford Science Publications, 1996

[14] B. Diu, D. Lederer and B. Roulet, Physique Statistique, Hermann editeurs des sciences et des arts, 1989

[15] D. Raabe, Computational Materials Science, Wiely editions, 1998

[16] J.M. Haile, Molecular Dynamics Simulation Elementary Methods, A Wiley-Interscience Publication, 1992

[17] J. Israelachvili, Intermolecular and Surface Forces, Academic Press, 1995

[18] M.W. Finnis and J.E. Sinclair, Philos. Mag. A, Vol. 50, No. 1, pp 45-55, 1984

[19] A.P. Sutton, J. Chen, Philos. Mag. Lett. 61 (1990)

[20] H. Rafii-Tabar and A.P. Sutton, Philos. Mag. Lett., Vol. 63, No. 4, pp 217-224, 1991

[21] B.R. Eggen, R.L. Johnson, Sidian Li and John N. Murrel, Mol. Phy., Vol. 76, No. 3, pp 619-633, 1992

[22] L.D. Lloyd, R.L. Johnson, Chem. Phy., Vol. 236, 1998

[23] H. Cox, R.L. Johnston and John N. Murrel, J. Sol. State Chem., 1993

[24] F. Ercolessi, M. Parrinello, E. Tosatti, Philos. Mag. A, Vol. 58, 1988

[25] M.S. Daw, M.I. Baskes, Phys. Rev. Lett. 50 1983

[26] M.S. Daw, M.I. Baskes, Phys. Rev. B 29 1984

[27] M.S. Daw, S.M. Foiles, M.I. Baskes, Mater. Sci. Rep. 9 (1993)

[28] B.S. Wherrett, Group Theory for Atoms, Molecules and Solids, Prentice/Hall International, 1986

[29] D.M. Heyes. Chem. Phy., Vol. 82, pp 285-301, 1983

[30] S. Nose, J. Chem. Phy., Vol. 81, 1984

[31] H.J.C. Berendsen, J.P.M. Postma, J. Chem. Phy. Vol. 81, 1984

[32] H.C. Anderson, J. Chem. Phy. Vol. 72, 1980

[33] W. G. Hoover, Phy. Rev. Vol. A 31, 1985

[34] H. Rafii-Tabar, Phy. Rep., Vol. 235, Number 6, March 2000

[35] Biosym/MSI scientific reports (1998)

[36] P.S.Y. Cheung, Mol. Phy., Vol. 33, No. 2, 1977

[37] T. Toffoli, M. Margolus, Cellular Automata Machines, the MIT press, 1987

[38] H.K. Versteeg and W. Malalasekera, An Introduction to Computational Fluid Dynamics (LONGMAN) 1996

[39] J.A. Spittle and S.G.R. Brown, Computer Simulation of the Effects of Alloy Variables on the Grain Structures of Castings, Acta Metallurgica, Vol. 37, No. 7, pp 1803-1810, 1989

[40] D.M.Heyes, Molecular Dynamics at Constant Pressure and Temperature, Chemical Physics, Vol. 82, pp 285-301, 1983

[41] Clive A. Croxton, Introduction to Liquid State Physics, John Wiley and Sons, 1975

[42] R. Hultgren, R.L. Orr, P.D. Anderson and K.K. Kelly, Selected Values of Thermodynamic Properties of Metals and Binary Alloys, John Wiley, 1963.

[43] Solder Alloy Data, Int. Tin Ins., 1986

[44] R.G. Parr, W. Yang, Density Functional Theory of Atoms and Molecules, May 1994

[45] M. C. Flemings, Solidification Processing, McGraw-Hill, 1974

[46] A. Prince, Alloy Phase Equilibria, Elsevier, 1966

[47] W. W. Mullins, R. F. Sekerka, Journal of Appl. Phy. Vol. 34, 1963

[48] W. W. Mullins, R. F. Sekerka, Journal of Appl. Phy. Vol. 35, 1964

[49] R. F. Sekerka, Journal of Crystal Growth, Vol. 3, 1968

[50] J. A. Spittle and S. G. R. Brown, Acta. Metall., Vol. 37, No. 7, pp. 803-1810, 1989

[51] D. J. Srolovitz, M. P. Anderson, P. S. Sahni and G. S. Grest, Acta. Metall., Vol. 32, pp. 793, 1984

[52] D. J. Srolovitz, and G. S. Grest, Acta. Metall., Vol. 33, pp. 2233, 1985

[53] D. J. Srolovitz and G. S. Grest, Acta. Metall., Vol. 34, pp. 1833, 1986

[54] N. Hatta, S. Yabushita and H. Nakata, Scripta Metall., Vol. 21, pp. 147, 1987

[55] D. J. Srolovitz, M. P. Anderson and G. S. Grest, Acta. Metall., Vol. 32, No. 9, pp. 1429-1438, 1984

[56] H. W. Hesselbarth and I. R. Gobel, Acta. Metall. Mater., Vol. 39, No. 9, pp. 2135-2143, 1991

[57] W. Kurz, B. Giovanola and R. Trivedi, Acta. Metall., Vol. 34, No. 5, pp. 823-830, 1986

[58] X. Tong, C.Beckermann, International Journal of Heat and Mass Transfer, Vol. 41, pp. 4025-4029, 1998

[59] J. D. Hunt, Q. Han and Shu-Zu Lu, Solidification Science and Processing, Edited by I. Ohnaka and D. M. Stefanescu, 1993

[60] M. Rappaz and PH. Thevoz, Acta. Metall., Vol. 35, No. 7, pp. 1487-1497, 1987

[61] C. Y. Wang and C. Beckermann, Materials Science and Engineering, A171. pp. 199-211, 1993

[62] Ch. A. Gandin. M Rappaz and D. West, Metallurgical and Materials Transactions A, Vol. 26A, June 1995

[63] C. Beckermann and C. Y. Wang, Solidification Science and Engineering, Edited by I. Ohnaka and D. M. Stefanescu, 1996

[64] X. Tong and C. Beckermann, Journal of Crystal Growth, Vol. 187, pp. 289-302, 1998

[65] V. Pines, A. Chait, M. Zlatkowski and C. Beckermann, Equiaxed Dendritic Solidification in Supercooled Melts, ~~September 18~~ Feb, 1999

[66] I. Steinbach, C. Beckermann, B. Kauerauf and Q. Li, Acta. Mater., Vol. 47, No. 3, pp. 971-982, 1999

[67] B. Cantor and A. Vogel, J. Crystal Growth, vol. ~~14~~ 41, p 109-, 1977

[68] M. Rappaz and Ch. A. Gandin, Acta. Metall. Mater., Vol. 41, No. 2, pp. 345-360, 1993

[69] M. Rappaz, International Materials Review, Vol. 34, No. 3, 1989

[70] I. Maxwell and A. Hellawell, Acta. Matall., Vol. 23, February 1975

[71] Ch. Charbon, A. Jacot and M. Rappaz, Acta. Metall. Mater., Vol. 42, No. 12, pp. 3953-3966, 1994

[72] Ch. A. Gandin, Ch. Charbon and M. Rappaz, ISIJ International, Vol. 35, No. 6, pp. 651-657, 1995

[73] Ch. A. Gandin and M. Rappaz, Acta. Mater., Vol. 45. No. 5, pp. 2187-2195, 1997

[74] K. Y. Lee and C. P. Hong, Solidification Science and Processing, Edited by I. Ohnaka and D. M. Stefanescu, 1996

[75] Ph. Thevoz, J. L. Desbiolles and M. Rappaz, Metall. Trans. A, Vol. 20A, February 1989

[76] D. M. Stefanescu and G. Upadhya, Metall. Trans. A, Vol. 21A, April 1990

[77] Ch. A. Gandin and M. Rappaz, Acta. Metall. Mater., vol. 42, No. 7, pp. 2233-2246, 1994

[78] S. P. Marsh and D. Banerjee, Materials Processing in the Computer Age II, Edited by V. R. Voller and S. P. Marsh, 1995

[79] M. E. Glicksman and R. N. Smith, Metall. Trans. A, Vol. 23A, February 1992

[80] H. Combeau and J. M. Drezet, Metall. and Mater. Trans. A, Vol. 27A, August 1996

[81] M. C. Schneider and J. P. Gu, Metall. and Mater. Trans. A, Vol. 28A, July 1997

[82] Ch. Charbon and R. Lesar, Solidification Science and Engineering, Edited by I. Ohnaka and D. M. Stefanescu, 1996

[83] C. R. Swaminathan and V. R. Voller, Metall. Trans. B, Vol. 23B, October 1992

[84] Modelling of Casting, Welding and Advanced Solidification Processes VII, P. N. Quested, K. C. Mills and R. F. Brooks, Edited by M. Cross and J. Campbell, 1995

[85] C.W. Gardiner, Handbook of Stochastic Methods, Springer, Berlin, 1985

[86] S. R. coriell, B. T. Murray and A. A. Chernov, Journal of Crystal Growth, Vol. 141, pp. 219-233, 1994

[87] W. W. Mullins and R. F. Sekerka, Journal of Applied Physics, Vol. 35, pp. 444, 1964

[88] H. Rafii-Tabar, L.Hua and M.Cross, J.Phys. Condens. Matter, Vol. 10, pp. 2375, 1998

[89] A. Ludwig, K. Greven and P. R. Sahm, Journal of Crystal Growth, Vol. 186, pp. 291-297, 1998

[90] John Campbell, Casting, Buttenworth and Heinemann, 1997

[91] G. E. Dieter, Mechanical metallurgy, 1988

[92] S. V. Patankar, Numerical heat transfer and fluid flow, 1980

[93] T. N. Croft, Unstructured Mesh-Finite Volume Algorithms for Swirling, Turbulent, Reacting Flows. PhD Thesis, University of Greenwich, London, 1998.

[94] V. R. Voller and C. R. Swaminathan, General Source-Based Method for Solidification Phase change. Numerical heat transfer, Part B, 19(2):175-189, 1991

[95] G.A. Taylor, PhD Thesis, University of Greenwich, 1996

[96] F.P. Incropera, D.P. DeWitt, Fundamentals of Heat and Mass Transfer, Wiley, 1996

[97] Physica Guide, University of Greenwich, 1999

[98] Internal comminication by Rolls-Royce industries